

UNCLASSIFIED

AD NUMBER
AD910393
NEW LIMITATION CHANGE
TO Approved for public release, distribution unlimited
FROM Distribution authorized to U.S. Gov't. agencies only; Test and Evaluation; APR 1973. Other requests shall be referred to Air Force Flight Dynamics Laboratory, ATTN: FY, Wright-Patterson AFB, OH 45433.
AUTHORITY
AFFDL ltr dtd 27 Aug 1979

THIS PAGE IS UNCLASSIFIED

THIS REPORT HAS BEEN DELIMITED
AND CLEARED FOR PUBLIC RELEASE
UNDER DOD DIRECTIVE 5200.20 AND
NO RESTRICTIONS ARE IMPOSED UPON
ITS USE AND DISCLOSURE,

DISTRIBUTION STATEMENT A

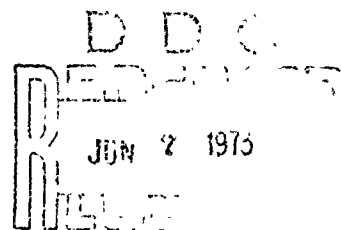
APPROVED FOR PUBLIC RELEASE;
DISTRIBUTION UNLIMITED,

AD910393

AFFDL-TR-72-140
Volume I

VIBRATION RESPONSE OF BALLISTIC RE-ENTRY VEHICLES

L. E. CHAUMP, J. H. LAUZON, H. R. MINNICH
GENERAL ELECTRIC COMPANY



TECHNICAL REPORT AFFDL-TR-72-140, VOLUME I

APRIL 1973

Distribution limited to U.S. Government agencies only; test and evaluation; statement applied 28 November 1972. Other requests for this document must be referred to AF Flight Dynamics Laboratory, (FY), Wright-Patterson AFB, Ohio 45433.

NOTICE

When Government drawings, specifications, or other data are used for any purpose other than in connection with a definitely related Government procurement operation, the United States Government thereby incurs no responsibility nor any obligation whatsoever; and the fact that the government may have formulated, furnished, or in any way supplied the said drawings, specifications, or other data, is not to be regarded by implication or otherwise as in any manner licensing the holder or any other person or corporation, or conveying any rights or permission to manufacture, use, or sell any patented invention that may in any way be related thereto.

Copies of this report should not be returned unless return is required by security considerations, contractual obligations, or notice on a specific document.

VIBRATION RESPONSE OF BALLISTIC RE-ENTRY VEHICLES

L. E. CHAUMP, J. H. LAUZON, H. R. MINNICH

GENERAL ELECTRIC COMPANY

Distribution limited to U. S. Government agencies only; test and evaluation statement applied 28 November 1972. Other requests for this document must be referred to AF Flight Dynamics Laboratory, (FY), Wright-Patterson AFB, Ohio 45433.

FOREWORD

This report was prepared by the General Electric Company, Re-entry and Environmental Systems Division, Philadelphia, Pennsylvania, for the Air Force Flight Dynamics Laboratory, Wright-Patterson Air Force Base, Ohio, under Contract F33615-71-C-1562. The study on which this report is based was conducted under Project 1370, "Dynamic Problems in Military Flight Vehicles", and Task Number 137005, "Prediction and Control of Flight Vehicle Vibration", sponsored by the Vehicle Dynamics Division, Aerospace Dynamics Branch, with Captain M. Prola as Project Engineer.

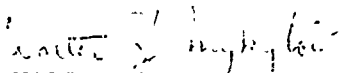
This report concludes the work on Contract F33615-71-C-1562 which covered a period from April 1971 to October 1972.

The final report is presented in two volumes. The first volume describes a prediction technique for the vibration response of high beta re-entry vehicles, discusses correlation of predicted with measured data, describes techniques for ground simulation of re-entry vibration, and documents computer programs, available through the Air Force Flight Dynamics Laboratory (FY), for computing re-entry vibrations. The second volume describes the FATE IIIA prototype vehicle used in the modal survey and acoustic testing, and presents the modal survey results.

The authors gratefully acknowledge the assistance of L. Mitchell, R. Condran, and N. Anderson in performing the vehicle modal survey at GE-RESO; and AFFDL/FYA personnel in their conduction of acoustic testing in the Sonic Fatigue Facility with E. Tolle as Test Director.

The report was submitted by the authors 1 September 1972.

This technical report has been reviewed and is approved.


WALTER J. MYKYTOW
Asst. for Research & Technology
Vehicle Dynamics Division

ABSTRACT

A technique is presented for predicting the vibration responses to reentry aero-acoustic loading of high beta ballistic vehicles (those having a weight-to-drag ratio greater than 1500). Correlation of predicted responses due to ground acoustic loading and measured data is given and, based on these results, guidelines on the use of the prediction technique for acoustic and aero-acoustic loading are outlined. Computer programs for calculating vibration responses due to reverberant and progressive wave acoustic environments and to aero-acoustic excitations are documented and are available through the Air Force Flight Dynamics Laboratory (FFDL). Techniques for ground simulation of re-entry vibration response are discussed, and typical component design requirements and test specifications are delineated. The new feature of the technique is the use of finite element methods in deriving component test specifications. These more accurate test specifications will be essential in reducing the number of overdesigned components, thereby decreasing the cost of mission completion.

TABLE OF CONTENTS

<u>Section</u>	<u>Title</u>	<u>Page</u>
I	INTRODUCTION	1
II	SUMMARY	2
	1. Typical Re-Entry Environment	2
	2. Response Prediction Technique	2
	3. Prototype Vehicle Dynamic Characteristics	2
	4. Re-Entry Vibration Response Predictions	4
	5. Response Verification Test	4
	6. Prediction Technique Verification	4
	7. Simulation Techniques, Design and Test Requirements	5
III	TYPICAL RE-ENTRY ENVIRONMENT	6
	1. Aeroacoustic Environments	6
	2. Forebody Pressure Cross Power Spectral Density	6
	3. Wake Pressure Cross Power Spectral Density	9
	4. Octave Band Sound Pressure Levels	13
IV	RESPONSE PREDICTION TECHNIQUE	14
	1. Literature Survey	14
	2. Optimized Technique	16
	3. Re-Entry Vibration Response	22
	4. Reverberant Chamber Response	27
	5. Progressive Wave Chamber Response	28
	6. Computer Programs	29
V	PROTOTYPE VEHICLE DYNAMIC CHARACTERISTICS	31
	1. Definition of Prototype Vehicle	31
	2. Dynamic Model	31
	3. Modal Survey Summary	34
	4. Frequencies, Mode Shapes and Damping	40
VI	RE-ENTRY VIBRATION RESPONSE PREDICTIONS	47
	1. Combined Forebody and Wake Environments	47
	2. Separate Forebody, Wake Environments	55

PRECEDING PAGE BLANK-NOT FILMED

TABLE OF CONTENTS (Continued)

<u>Section</u>	<u>Title</u>	<u>Page</u>
VII	RESPONSE VERIFICATION TEST	56
	1. Objectives	56
	2. Test Requirements	56
	3. Test Results	61
VIII	PREDICTION TECHNIQUE VERIFICATION	66
	1. Test Acoustic Environment Description	66
	2. Test Vibration Response Prediction	72
	3. Test-Analysis Correlation	72
	4. Discussion	79
IX	VEHICLE RE-ENTRY SIMULATION TECHNIQUES	80
	1. Current Aeroacoustic Environment Description	80
	2. Current Re-Entry Vibration Environment Description	82
	3. Simulation Techniques	82
	4. AFFDL Sonic Fatigue Facility Capabilities	85
X	DESIGN REQUIREMENTS, TEST SPECIFICATIONS	86
	1. Specification Derivation Guidelines	86
	2. Typical Component Test Specifications	87
	3. Internal Acoustic Environments	87
XI	CONCLUSIONS AND RECOMMENDATIONS	89
	1. Vibration Response Predictions	89
	2. Acoustic Testing	89
	3. Simulation Techniques	90
	REFERENCES	91

LIST OF ILLUSTRATIONS

<u>Figure</u>	<u>Title</u>	<u>Page</u>
1	Summary of Vibration Response Prediction	3
2	Flow Parameters Along the Prototype Vehicle	7
3	Spatial Correlation Functions	8
4	Fluctuating Aero-Dynamic Properties on Base of Re-entry Vehicle	11
5	Delta Turning Angle Vs. Mach Number	12
6	Octave Band Sound Pressure Levels on Forebody and Base	13
7	SABOR Finite Element Coordinate Conventions	20
8	Dynamic Model	32
9	Sabor Modeling of Shell Joints	35
10	Sabor Modeling of Bulkhead Attachments	35
11	Modal Survey Test Setup	37
12	Schematic of Sensor Identification and Location	38
13	Axial Mode Shape	43
14	Axial Mode Shape	43
15	Lateral Mode Shape	44
16	Lateral Mode Shape	44
17	Lateral Mode Shape	45
18	Accelerometer 1AL Response	47
19	Accelerometer 1AT Response	48
20	Accelerometer 3AL Response	48
21	Accelerometer 3AT Response	49
22	Accelerometer 4AL Response	49
23	Accelerometer 4AT Response	50
24	Accelerometer 5AL Response	50
25	Accelerometer 5AT Response	51
26	Accelerometer 6AL Response	51
27	Accelerometer 6AT Response	52
28	Accelerometer 8AN Response	52
29	Accelerometer 9AN Response	53
30	Accelerometer 10AL Response	53
31	Vehicle Support System	57
32	Schematic of External Acoustic Sensors	58
33	Acoustic Spectrum -- Minimum Level	59
34	Quick-Look Acoustic Data Processing	59
35	Detailed Acoustic Data Processing	60
36	Vibration Data Processing	61
37	Forebody Sound Pressure Level in Progressive Test	62
38	Forebody Sound Pressure Level in Reverberant Test	62
39	Base Sound Pressure Level in Progressive Test	63
40	Base Sound Pressure Level in Reverberant Test	63
41	Internal Sound Pressure Level (2PL) in Progressive Test	64
42	Internal Sound Pressure Level (7PL) in Progressive Test	65

LIST OF ILLUSTRATIONS (Continued)

<u>Figure</u>	<u>Title</u>	<u>Page</u>
43	Narrow Band PSD'S of Microphone L1	67
44	Meridional Space-Time Correlation Data	67
45	Meridional Spatial Correlation Function	68
46	Circumferential Space-Time Correlation Data	70
47	Circumferential Spatial Correlation Function	70
48	Meridional Space-Time Correlation Comparison	71
49	Circumferential Space-Time Correlation Comparison	71
50	1AL Vibration Response, Test Vs. Analysis	73
51	1AT Vibration Response, Test Vs. Analysis	73
52	3AL Vibration Response, Test Vs. Analysis	73
53	3AT Vibration Response, Test Vs. Analysis	73
54	4AL Vibration Response, Test Vs. Analysis	74
55	4AT Vibration Response, Test Vs. Analysis	74
56	5AL Vibration Response, Test Vs. Analysis	74
57	5AT Vibration Response, Test Vs. Analysis	74
58	6AL Vibration Response, Test Vs. Analysis	75
59	6AT Vibration Response, Test Vs. Analysis	75
60	8AN Vibration Response, Test Vs. Analysis	75
61	9AN Vibration Response, Test Vs. Analysis	75
62	10AL Vibration Response, Test Vs. Analysis	76
63	Axial Mode Shape, Test Vs. Analysis	78
64	Current Aeroacoustic Environment Description	81
65	PSD Envelope for Internal Components-Transition	82
66	PSD Envelope for Internal Components - TBL	83
67	Re-entry Response Simulation Technique	84
68	Test Specification Notching	86
69	Component Re-entry Vibration Test Specification (Internal Self Mounted)	87
70	Component Re-entry Vibration Test Specification (Forebody Sheil and Base)	88
71	Component Re-entry Shock Test Specification	88

LIST OF TABLES

<u>Table</u>	<u>Title</u>	<u>Page</u>
I	Coordinates at Nodes	33
II	Weight Breakdown	34
III	Sensor Description	39
IV	Comparison of Axial Experimental and Analytical Frequencies	41
V	Comparison of Lateral Experimental and Analytical Frequencies	42
VI	Transformations for Accelerometer Response Predictions	54

LIST OF SYMBOLS

A_n	— Area of n^{th} element, ft^2
a^*	— Speed of sound where Mach number equals 1, ft/sec
C	— Co narrowband space correlation coefficient
c	— Speed of sound in sonic chamber, ft/sec
c_1, c_2	— Decay constants in co-space correlation coefficient
f	— Frequency, Hz
f_c	— Center frequency, Hz
f_f	— Frequency bandwidth, Hz
g'	— Structural damping coefficient
H_k	— Modal transfer function, with $*$ denotes complex conjugate
i	— Imaginary designation
J_{θ}	— Joint acceptance in circumferential direction
K	— Stiffness in typical equation of motion
$[L]$	— Displacement transformation matrix
ℓ	— Meridional length of finite element, ft
M	— Mass in typical equation of motion, $\text{lb}\cdot\text{sec}^2/\text{ft}$
M_b	— Mach number associated with base flow
M_c	— Local or edge Mach number
M_k	— Modal mass of k^{th} mode, $\text{lb}\cdot\text{sec}^2/\text{ft}$
n	— Circumferential wave number
$p(s, t)$	— Distributed pressure in typical equation of motion, lb/ft^2
P_b	— Base static pressure, lb/ft^2

P_T	-- Total pressure, lb/ft ²
$\{\tilde{P}\}$	-- Generalized forces on finite element in element coordinate system
$\{\underline{P}\}$	-- Generalized forces on finite element in system coordinates
Q	-- Quadrature narrowband space correlation coefficient
q	-- Dynamic pressure, lbs/ft ²
q_i	-- Finite element coordinates
R	-- Radius of base, ft
\mathcal{R}	-- Space-time cross correlation function
r	-- Radius, ft
r_1	-- Radius on number 1 finite element, ft
s	-- Meridional location, ft
s_1	-- Meridional distance on number 1 finite element, ft
s_T	-- Meridional separation between left station of elements 1 and 2, ft
$\{\ }^T$	-- Transpose of matrix in brackets
u	-- SABOR axial displacement
V_c	-- Convected velocity of turbulent flow, ft/sec
V_e	-- Local or edge flow velocity, ft/sec
v	-- SABOR tangential displacement
w	-- SABOR radial displacement
z	-- Coordinate in typical equation of motion
α	-- Vehicle cone half angle, degrees
β	-- SABOR edge rotation
$[\beta]$	-- Transformation matrix to convert finite elemental coordinates to system coordinates

Γ	-- Modal damping
γ	-- Damping in typical equation of motion
δ^*	-- Boundary layer displacement thickness, ft
η	-- Separation distance across flow direction, ft
θ	-- Circumferential direction location, longitude angle, rad
θ^*	-- Half angle of wake cone, degrees
θ_1	-- Circumferential direction location on element 1, rad
ν_b	-- Prandtl-Mayer expansion angle on base, degrees
ν_e	-- Local Prandtl-Mayer expansion angle, degrees
ξ	-- Separation distance along flow direction, ft
ξ_n	-- Modal coordinate in typical equation of motion
$\{p\}$	-- Generalized force integral expressions
ρ_e	-- Local or edge density lb/ft ³
σ_b	-- Base rms pressure, lb/ft ²
σ_e	-- Local rms pressure, lb/ft ²
τ	-- Delay time, sec
Φ_b	-- Base pressure cross power spectral density, psf ² /Hz
Φ_{TBL}	-- Pressure cross power spectral density for turbulent flow, psf ² /Hz
Φ_P	-- Pressure cross power spectral density, psf ² /Hz
Φ_F	-- Force cross power spectral density lb ² /Hz
Φ_{FC}	-- Co-force cross power spectral density, lb ² /Hz
Φ_{FQ}	-- Quad - force cross power spectral density, lb ² /Hz
$\Phi_{F_1^1 F_1^2}$	-- Term in force cross power spectral density matrix, lb ² /Hz

- ϕ_R — Response cross power spectral density, response units²/Hz
- ϕ_δ — Displacement response power spectral density, in^2/Hz
- ϕ — Homogeneous pressure power spectral density. Subscripts denote location, psf^2/Hz
- φ — Mode shape
- ψ — Incidence angle for progressive waves, degrees
- ω — Radian frequency
- ω_k — Radian frequency of natural modes of vibration

SECTION I

INTRODUCTION

The prediction of vibration responses induced by random pressure fluctuations during re-entry of a high beta vehicle is a difficult task. (Beta is the ratio of vehicle weight to the product of its drag coefficient times its maximum cross-sectional area.) In general, the work of industry has been predominantly theoretical with very limited experimental data available to adequately determine the reliability of these theoretical methods. As a result of low confidence in predictions, it has been necessary to impose very conservative vibration design and test criteria in the development of components for high beta re-entry vehicles. These test specifications are usually obtained by multiplying scant measured flight data by the ratio of the dynamic pressures between the flight vehicle and the design vehicle for which the specifications are intended. This technique omits many factors which influence the vibration response and thus results in excessively high specifications. Thus much contract time and funding is expended in overdesigning components to pass laboratory tests that bear little resemblance to actual re-entry environments.

The objective of this exploratory and development program, then, is to assess the accuracy of analytical methods used throughout industry, and to refine and verify a selected method to enable the establishment of optimum vibration design and test criteria for both structure and equipment. These optimum design and test criteria will be much more representative of actual flight environments thereby reducing component specification over conservatism.

SECTION II

SUMMARY

The prediction of re-entry vibration response involves the use of aeroacoustic forcing functions in conjunction with vehicle dynamic characteristics. The description and interaction of these input parameters with the prediction technique is illustrated by the flow diagram in Figure 1. This flow diagram forms the basis for the organization and logic sequence of tasks performed in this study program; in particular, it emphasizes the need for well-defined acoustic forcing functions and vehicle dynamic characteristics in order to achieve verification of the response prediction technique.

1. TYPICAL RE-ENTRY ENVIRONMENT

Utilizing state-of-art techniques in defining fluctuating pressure environments on re-entry vehicles, a baseline re-entry environment is defined for the prototype vehicle to be used in later tasks. There are two aerodynamic induced environments considered. These are pressure fluctuations in the turbulent boundary layer which act on the vehicle forebody, and pressure fluctuations in the wake which act on the vehicle base. The homogeneous pressure spectrum is defined at each vehicle station as well as cross correlation coefficients so that the cross pressure spectrum can be represented. The aerodynamic parameters utilized in these expressions included local Mach numbers, local convected velocities, local densities, and boundary layer displacement thickness. These aerodynamic parameters are not typically generated by a structural dynamicist. Reference (23) shows how these parameters are obtained from the information which is usually available such as trajectory properties.

2. RESPONSE PREDICTION TECHNIQUE

An all-inclusive formulation of vehicle response due to distributed random pressure environments is first presented. In this formulation no simplifying assumptions have been made. Then, utilizing the results of a detailed literature survey, the complex formulation is simplified to yield a less complex response prediction technique, with no appreciable loss in accuracy but significant gains in economy associated with the computer implementation. A detailed examination of the force cross Power Spectral Density matrix is made to show how the analytical techniques can be applied to acoustic environments encountered in ground testing as well as re-entry aeroacoustic environments. It is shown how further simplifications can be made to the formulation of the force cross PSD matrix in cases where the pressure cross PSD can be considered constant over the size of the finite elements in the dynamic model. In the more general case where this assumption is not valid, individual terms in the force cross PSD matrix are shown as they would be numerically integrated.

3. PROTOTYPE VEHICLE DYNAMIC CHARACTERISTICS

A mathematical representation of the dynamic characteristics of the prototype vehicle is formulated. From available drawings and measurements of component weights and locations, a finite element idealization of the vehicle is obtained. The shell modeling is

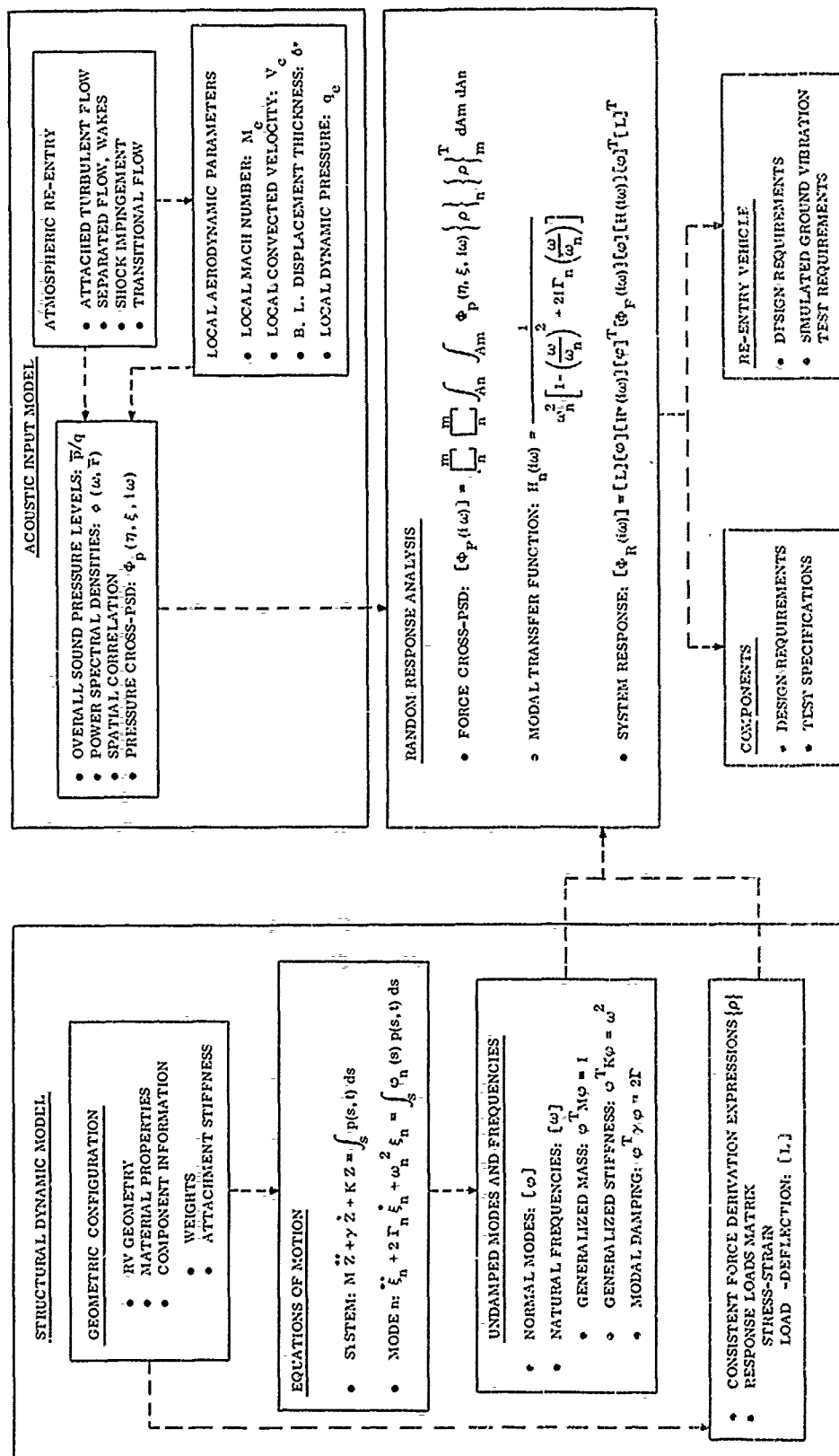


Figure 1. Summary of Vibration Response Prediction

performed utilizing the MIT - developed SABOR program and the vehicle nose and component packages are modeled using beam finite elements. Two separate dynamic models are constructed, one describing the vehicle axial dynamic characteristics and the other describing the lateral dynamic characteristics.

To verify and supplement the dynamic models, a modal survey is conducted on the prototype vehicle. The vehicle natural frequencies and mode shapes are determined in the 20 to 2000 Hz frequency range. This modal data is then used to revise the analytical model in areas of obvious deficiency. The modal survey data is also utilized to obtain the damping characteristics in each mode.

In addition to the external probe accelerometer used to define the shell motion, thirteen internal accelerometers are also utilized. These accelerometers are located in both component packages, the internal shell structure and the aft cover. It is this internal instrumentation that is used in the acoustic test to obtain the component responses and verify the response prediction techniques.

4. RE-ENTRY VIBRATION RESPONSE PREDICTIONS

The response prediction technique, in conjunction with the verified dynamic model, is used to predict the prototype vehicle vibration response to the baseline re-entry environment. Acceleration power spectral densities are predicted at each of the internal accelerometer locations. The vibration response predictions utilized the simultaneous application of the turbulent boundary layer environment and the wake environment. A discussion is also included on the effects of each environment applied separately. These vibration responses form the basis for acoustic test requirements in verifying the prediction technique.

5. RESPONSE VERIFICATION TEST

Acoustic tests are conducted at the AFFDL Sonic Fatigue Facility on the prototype vehicle. The objective of these tests is: (1) to verify the response prediction technique by obtaining vehicle response data in a form suitable for correlation with analysis at levels similar to re-entry, and (2) to define vehicle simulation techniques by making accurate measurements of external and internal acoustic levels to define and express experimental forcing functions.

Response predictions were made on the prototype vehicle under ideal reverberant and progressive wave conditions, which, when correlated with the re-entry vibration predictions, defined a minimum sound pressure level requirement for the acoustic tests to simulate re-entry as best as possible.

6. PREDICTION TECHNIQUE VERIFICATION

The measured acoustic environments achieved in the AFFDL Sonic Fatigue Facility are used in the prediction technique to compute vibration response at the instrumentation locations. Correlation of predicted responses with test data shows good comparison. Guidelines are given in utilization of the prediction technique; in particular, attention is given to dynamic modeling procedures required as a function of the type and location of vibration response desired.

7. SIMULATION TECHNIQUES, DESIGN AND TEST REQUIREMENTS

Aeroacoustic environments occurring at various stages of re-entry are discussed, based on the current state of art.

In addition, best estimates of resulting vibration levels are described.

Methods of simulating re-entry responses, not necessarily re-entry loadings, are given for various stages of re-entry. It is shown that acoustic cross-correlation effects achieved in the AFFDL Sonic Fatigue Facility contribute to significant response, even though overall sound pressure levels in the test facility are less than re-entry values.

Typical design requirements and test specifications for skin-mounted and internal shelf-mounted components are given. These are based on the results of numerous analytical studies and limited flight data measured by GE-RESA in current high beta re-entry vehicle programs.

SECTION III

TYPICAL RE-ENTRY ENVIRONMENT

1. AEROACOUSTIC ENVIRONMENTS

During re-entry a high beta vehicle is subjected to pressure fluctuations in the attached turbulent boundary layer, pressure fluctuations in the wake flow, and pressure fluctuations due to the transition from laminar to turbulent flow. If the vehicle is of the class containing protuberances or flare sections, local oscillating shocks will also occur. The prototype vehicle used in this study did not contain protuberances and is therefore not expected to experience shock loadings of any significance during re-entry. At this time, little is known about the nature of the environment during transition and there are no analytical expressions for pressure cross PSD during transition. The environments presented for this study are therefore for fully - turbulent and wake flow conditions.

2. FOREBODY PRESSURE CROSS POWER SPECTRAL DENSITY

Houbolt's relations ^(1, 2) are used to express the pressure cross PSD. There are four flow parameters required to formulate the pressure spectrum and spatial correlation functions. These parameters are boundary layer displacement thickness, δ^* , local or edge Mach number, M_e , local or edge velocity, V_e , and local or edge density, ρ_e . Figure 2 shows how these four parameters vary with prototype vehicle station.

The pressure cross PSD can be written as

$$\Phi_{TBL}(\xi, \eta, f) = [C(\xi, \eta, f) + i Q(\xi, \eta, f)] \phi(f) \quad (1)$$

where

$C(\xi, \eta, f)$ = In-phase or co-correlation function.

$Q(\xi, \eta, f)$ = Out of phase or quad correlation function.

$\phi(f)$ = Pressure PSD at a station.

ξ = Separation distance in the meridional direction (along the flow).

η = Separation distance in the circumferential direction (across the flow)

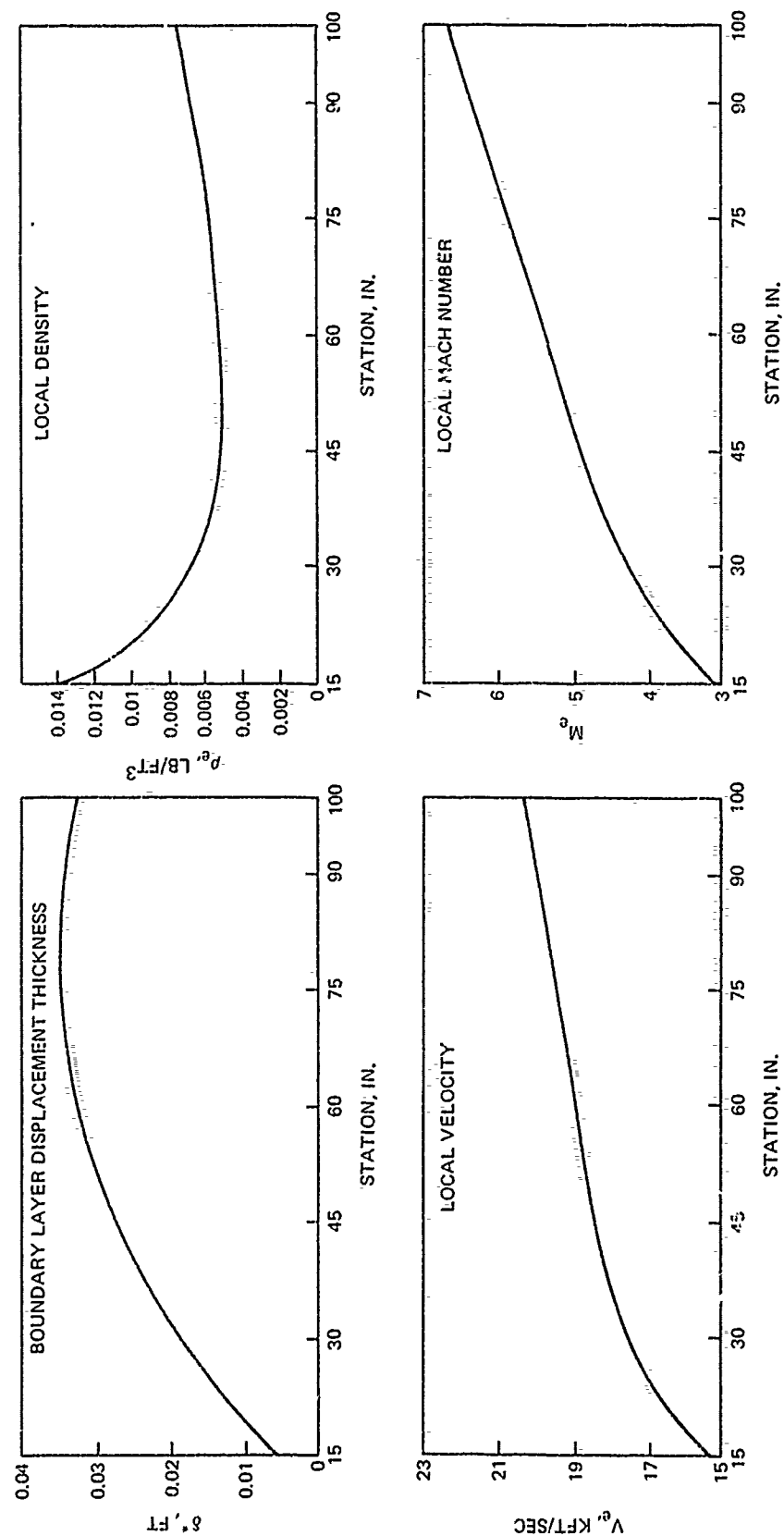


Figure 2. Flow Parameters Along the Prototype Vehicle

The spatial correlation functions can be written as

$$C(\xi, \eta, f) = e^{\frac{-c_1 |\xi|}{\delta^*}} e^{\frac{-c_2 |\eta|}{\delta^*}} \cos \frac{2\pi f \xi}{V_c} \quad (2)$$

$$Q(\xi, \eta, f) = e^{\frac{-c_1 |\xi|}{\delta^*}} e^{\frac{-c_2 |\eta|}{\delta^*}} \sin \frac{2\pi f \xi}{V_c} \quad (3)$$

where

V_c = Convected velocity, equal to $0.7 V_e$.

c_1 = Decay constant, assumed to be 0.05 for this study (based on data in Reference 3).

c_2 = Another decay constant assumed equal to 1⁽¹⁾.

Figure 3 shows a graphical description of the above correlation functions.

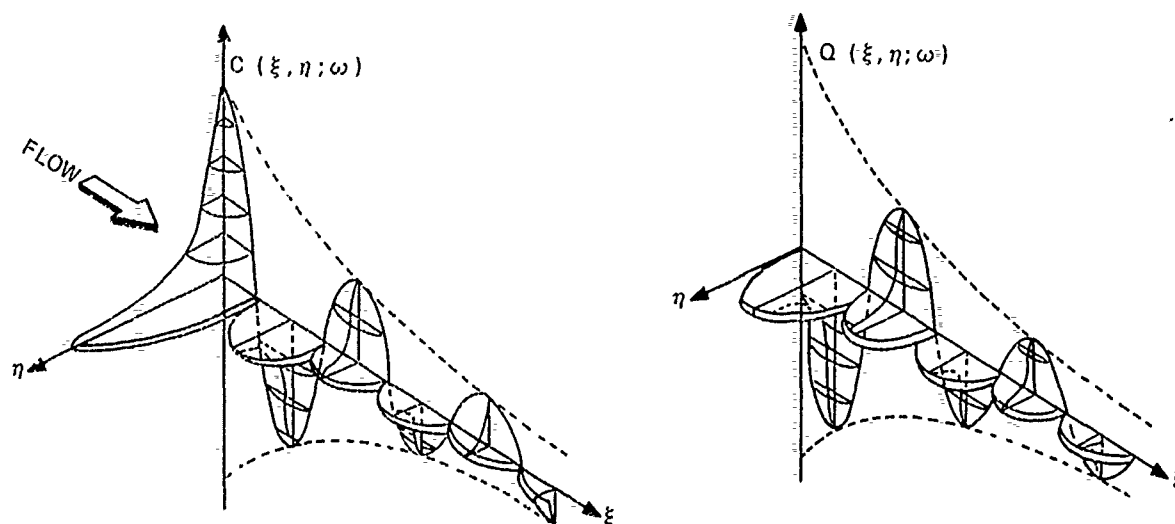


Figure 3. Spatial Correlation Functions

Many investigators also include additional decay terms in the correlation functions, which have the following form

$$e^{\frac{-c_1 |\xi| \omega}{V_c}} e^{\frac{-c_2 |\xi| \omega}{V_c}}$$

These investigators are usually concerned with flow conditions at subsonic or slightly supersonic velocities. For the high beta re-entry vehicle where convected velocities are 10 to 14 kft./sec and the boundary layer displacement thickness are 0.005 to 0.035 ft., the above

terms become insignificant when compared to $e^{-\frac{c_1 |\xi|}{\delta^*}} e^{-\frac{c_2 |\eta|}{\delta^*}}$. For example, the total expression with the added decay terms included would be as follows: $C(\xi, \eta, f) = e^{-\frac{c_1 |\xi|}{\delta^*} \left[\frac{1}{\delta^*} + \frac{2\pi f}{V_c} \right]} e^{-\frac{c_2 |\eta|}{\delta^*} \left[\frac{1}{\delta^*} + \frac{2\pi f}{V_c} \right]} \cos \frac{2\pi f \xi}{V_c}$. Using stated values of δ^* and V_c , the terms in the brackets would be $\left[\frac{1}{0.035} + \frac{2\pi f}{14000} \right]$, or approximately $\left[30 + 4.5 \times 10^{-4} f \right]$.

It is seen that for frequencies less than 5 kHz, the term is negligible. It is for this reason that decay terms which are frequency-dependent need not be considered for structural responses in the 0 to 5 kHz range.

The pressure PSD, $\phi(f)$ has been formulated by Houbolt as:

$$\phi(f) = \frac{4\delta^* \sigma_e^2}{V_c} \left/ \left[1 + \left(\frac{2\pi f \delta^*}{V_c} \right)^2 \right] \right. \quad (4)$$

where σ_e is the rms pressure equal to

$$\sigma_e = 0.00011 \rho_e V_e^2 / (1 + 0.012 M_e^2) \quad (5)$$

3. WAKE PRESSURE CROSS POWER SPECTRAL DENSITY

The analytical expressions proposed for the pressure cross PSD over the aft end of the vehicle are essentially those for fully turbulent flow but with the following modifications:

- (1) the boundary layer displacement thickness is assumed equal to the base radius,
- (2) the convected velocity is the transverse component of the flow velocity along the wake boundary, and
- (3) the rms pressure is expressed with different coefficients to account for strong viscous shear and lack of cooling.

With these modifications the following relations result:

$$\phi_b(\xi, \eta, if) = \left[C(\xi, \eta, f) + i Q(\xi, \eta, f) \right] \phi_b(f) \quad (6)$$

$$C(\xi, \eta, f) = \frac{e^{-c_1 |\xi|}}{R} \frac{e^{-c_2 |\eta|}}{R} \cos \frac{2\pi f \xi}{V_b \sin \theta^*} \quad (7)$$

$$Q(\xi, \eta, f) = \frac{e^{-c_1 |\xi|}}{R} \frac{e^{-c_2 |\eta|}}{R} \sin \frac{2\pi f \xi}{V_b \sin \theta^*} \quad (8)$$

$$\phi_b(f) = \frac{4 R \sigma_b^2}{V_b \sin \theta^*} \left[1 + \left(\frac{2\pi f R}{V_b \sin \theta^*} \right)^2 \right] \quad (9)$$

$$\sigma_b = \frac{0.01 M_b^2 P_b}{1 + 0.18 M_b^2} \quad (10)$$

where

- R = Base radius
- V_b = Local velocity on base
- θ^* = Half angle of wake cone
- M_b = Base Mach number
- P_b = Static base pressure

The effect of replacing the boundary layer displacement thickness with the base radius yields a slowly decaying spatial correlation function, indicative of highly correlated pressures. Also the $R/V_b \sin \theta^*$ term tends to cause the base frequency spectrum to decay much faster than the forebody spectrum.

The methods used to determine the base flow parameters will now be briefly described. Data required to determine the flow parameters on the base are aerodynamic conditions on the aft end of the forebody. For this study these properties are:

- V_e = 20325 ft/sec.
- P_e = 1759.7 lbs/ft.²
- M_e = 6.723

Tables giving properties of compressible flow including Prandtl-Meyer angles, ν , as a function of Mach number are required. An excellent source of this information is found in Reference 4. Figure 4 shows the flow parameters on the re-entry vehicle base.

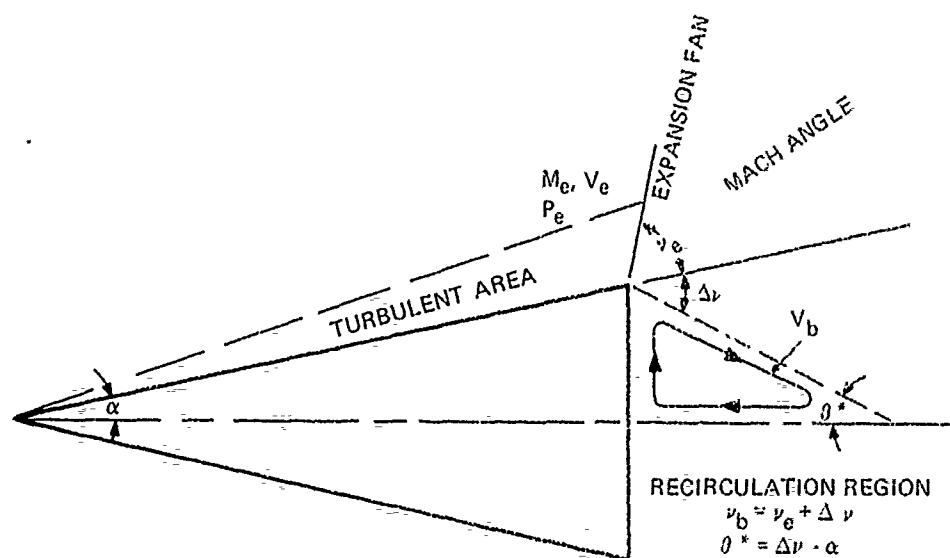


Figure 4. Fluctuating Aero-Dynamic Properties on Base of Re-entry Vehicle

From the tables of Reference 4 at $M_e = 6.723$ we obtain

$$\nu_e = 89.448$$

$$P_e/P_T = 0.0003127$$

$$V_e/a^* = 2.3242$$

Now using Figure 5, which is based upon flight base pressure data⁽⁵⁾ and the difference between the Prandtl-Meyer angles for isentropic expansion from cone pressure and base pressures⁽⁴⁾, we obtain $\Delta \nu$ as 16° at $M_e = 6.723$. The Prandtl-Meyer angle, associated with the base flow is:

$$\nu_b = \nu_e + \Delta \nu$$

$$\nu_b = 89.448 + 16$$

$$\nu_b = 105.448$$

and from Figure 4:

$$\theta^* = \Delta \nu - \alpha = 9.7^\circ$$

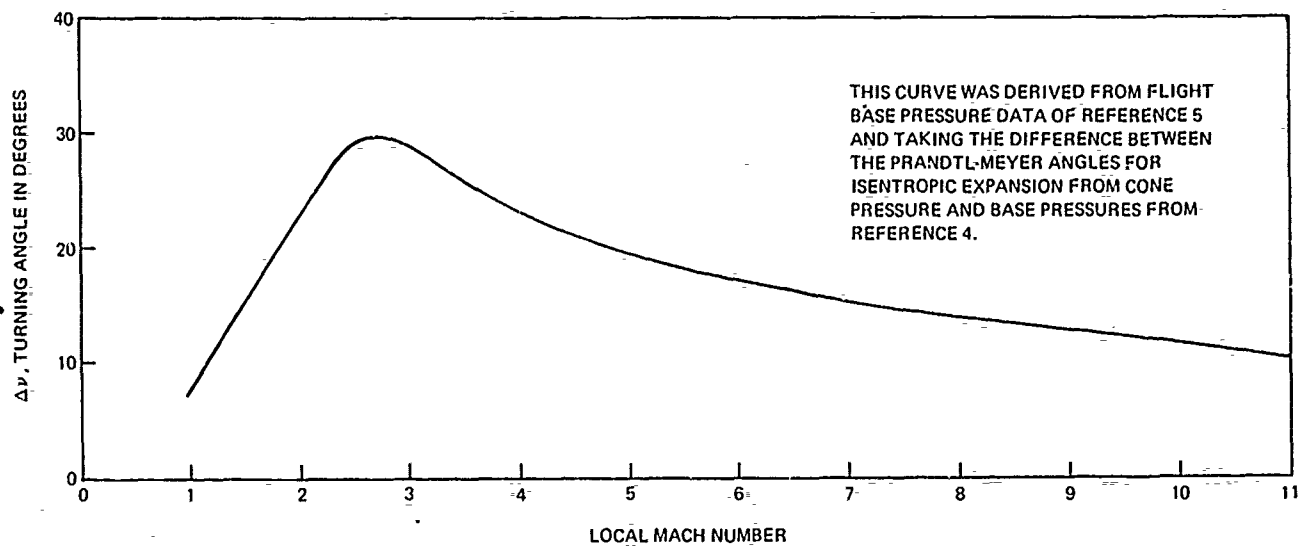


Figure 5. Delta Turning Angle Vs. Mach Number

Using the tables of Reference 4 the Mach number, M_b , which corresponds to a ν_b of 105.448 is obtained. At this M_b the required ratios P_b/P_T and V_b/a^* are also obtained:

$$M_b = 11.3$$

$$P_b/P_T = 0.00001039$$

$$V_b/a^* = 2.403$$

We now have all the data required to obtain the base flow parameters.

$$P_b = \frac{P_b/P_T}{P_e/P_T} P_e = 58.5 \text{ lb/ft}^2$$

$$V_b = \frac{V_b/a^*}{V_e/a^*} V_e = 21014 \text{ ft/sec}$$

$$\sigma = \frac{0.01 M_b^2 P_b}{1 + 0.18 M_b^2} = 3.1 \text{ lb/ft}^2 \text{ rms}$$

4. OCTAVE BAND SOUND PRESSURE LEVELS

Sound pressure levels for both the base pressure spectrum and the maximum forebody spectrum have been evaluated in octave bands. Figure 6 shows the various dB levels associated with each octave band which are used to estimate the levels required in the acoustic test.

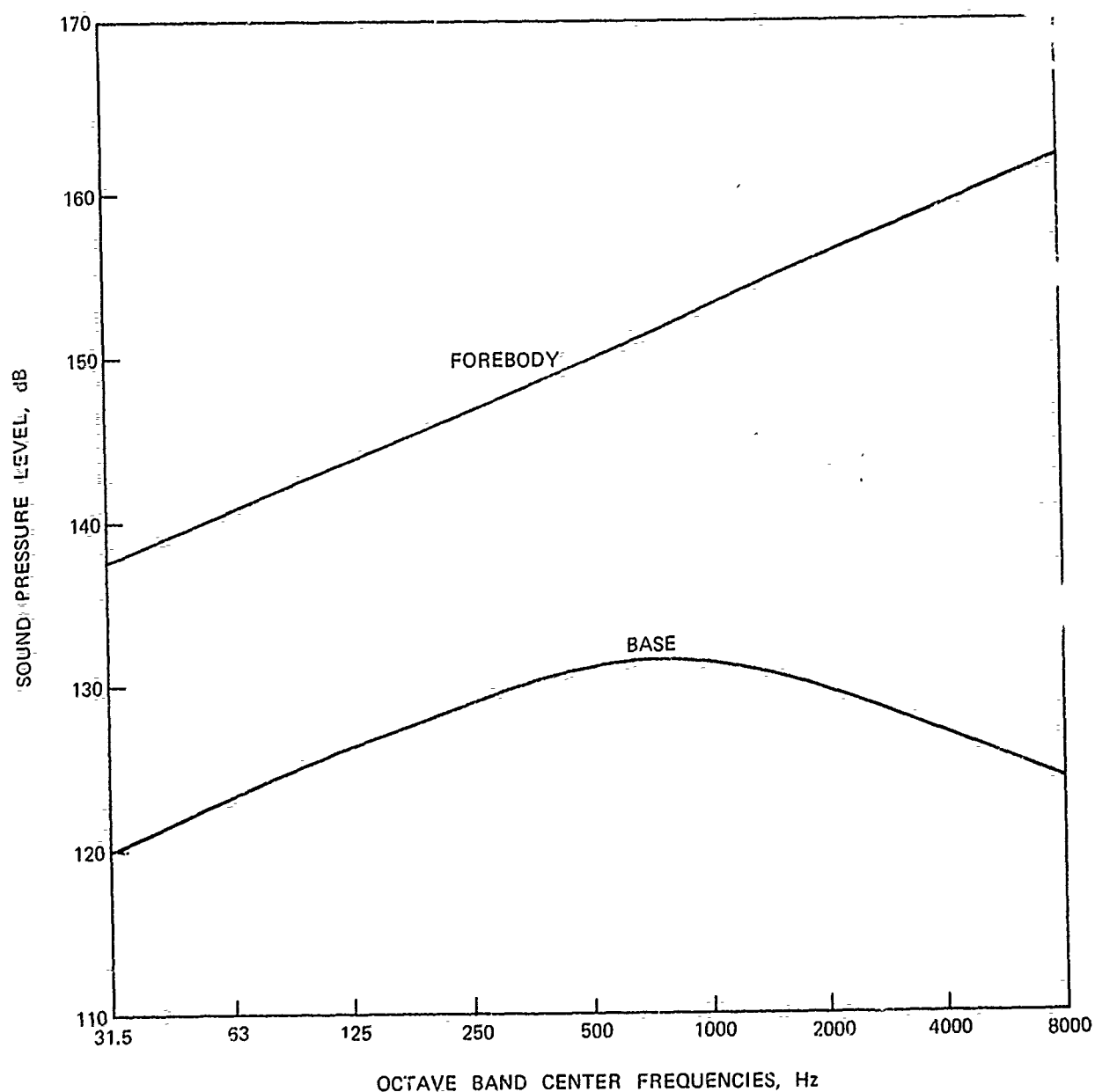


Figure 6. Octave Band Sound Pressure Levels on Forebody and Base

SECTION IV

RESPONSE PREDICTION TECHNIQUE

1. LITERATURE SURVEY

The goal of this task was to obtain, from previously published work, simplifying assumptions which can be made in the vibration response prediction technique with little loss of accuracy but significant economic gains. Many reports and papers were therefore reviewed to satisfy this goal. Of particular interest in these reports were the generalized force formulations and the retention or elimination of cross modal terms in the response formulation. Because this study made use of a dynamic model constructed via the finite element technique, only those reports which also employed finite element dynamic models were of interest with respect to the generalized force. Those reports utilizing closed-form solution dynamic models were of interest with respect to the response formulation.

References 6 through 15 are concerned with the prediction of vibration response of simply-supported panels and cylinders to turbulent boundary layer pressure fluctuations, jet noise, and acoustic fields. All of the reports utilize a closed-form solution for the normal modes of vibration. The response formulations nearly all follow the same format. An all-comprehensive expression is initially developed which includes all the cross modal contributions and the imaginary spectra. The formulation is then simplified to eliminate cross modal terms. There are varying arguments given for this simplification. In the work of Bozich and White (7) and Cockburn and Jolly (9), space averaging the response exactly eliminates the cross modal response because of orthogonality of the mode shapes. Crocker (10) and Bozich (6) merely mention they are neglecting cross modal response terms and formulate the response accordingly. Maestrello (11) (12) neglects cross modal terms based on the assumption that the natural frequencies are well spaced and there is little damping in the panel.

Clarkson (8) cites an investigation by another investigator as the basis for elimination of cross modal terms in his work. This other investigator showed only a 5 to 10 percent contribution to the rms response as a result of these terms in typical cases. Szechenyi (14) gives as the basis for elimination of cross modal terms the work of Wilby (15). Wilby has shown that the cross modal terms do not change the peak power spectral density response points at all. Wilby also shows good correlation with test results in his work. Strawderman and Brand (13) are the exceptions; they formulated the response retaining all terms.

It should be pointed out that the response formulation (elimination of cross modal terms) was the only item applicable to this study in References 6 through 15. However there is much more to be gained from the above reports if such information as sound radiation from panels and design charts for fatigue is desired.

References 16 through 19 represent a series of reports in which the panel response to turbulent boundary layer pressure fluctuations is obtained utilizing a finite element description of the panel to obtain frequencies and modes. References 16, 17, and 18 use the same finite element program and response program for vibration solutions. The response formulation is developed such that all terms are utilized and both real and imaginary response is obtained.

The generalized force is also a complex quantity. The force cross Power Spectral Density (PSD) is obtained by integrating the pressure cross PSD over pairs of finite elements. This gives an exact formulation of force cross PSD which has no limitations on upper response frequency or finite element size. This is important in solving the class of turbulent boundary layer problems where the pressure is not constant over the finite element. Olson and Lindberg⁽¹⁹⁾ follow the same format as Jacobs and Lagerquist⁽¹⁶⁾ except that they obtain the force cross PSD by assuming a constant pressure over the finite element pairs. The force cross PSD is obtained by multiplying the pressure cross PSD, evaluated by using the separation distances between element c.g.'s, by the consistent forces for a unit psi on the elements. This imposes a frequency limit above which no valid calculations can be made. For the problem they analyzed, the upper limit is 1500 Hz.

Jacobs, et. al.,⁽¹⁶⁾⁽¹⁷⁾ present a strong argument for elimination of cross modal terms in the response analysis. In Reference 16 they show a variation of only nine percent on peak PSD points and six percent on mean square response when the cross modal terms are excluded. In Reference 17, in which the problem contained modes very close in frequency, they stated that inclusion of cross modal terms did not increase deflection response.

Schweiker and Davis⁽²⁰⁾ are the only investigators found which treat a class of problems where the pressure PSD (not pressure cross PSD) is not a constant over the entire structure. They solved the problem of a conical shell subjected to pressure fluctuations in the turbulent boundary layer. The dynamic model is based on an assumed closed-form solution; however the structure is broken up into a series of sub-areas, much like finite elements, to formulate the response. The normal coordinate of each sub-area is the integral of the assumed mode shape over the areas. The force cross PSD between pairs of sub areas is obtained from the product of the integration of the spatial correlation function over the sub-areas, the integration of the mode shape over the sub-areas and square root of the product of the homogeneous power spectra on the areas, e.g.

$$C_F^{kl}(\omega) = \sqrt{\phi_P^{kk} \phi_P^{ll}} \left[\int_{A_l} \int_{A_k} C(\xi, \eta, \omega) dA_l dA_k \right] \left[\frac{\int_{A_k} \varphi dA_k \int_{A_l} \varphi dA_l}{A_k A_l} \right] \quad (11)$$

where

ϕ_P^{kk}, ϕ_P^{ll} = Homogeneous power spectra on sub-areas k and l.

$C(\xi, \eta, \omega)$ = Spatial correlation function.

φ = Assumed mode shape.

They have shown the insignificance of cross modal terms in the response formulation. Even when they had modes within 1 Hz of each other a variation of only 15 percent was observed in peak PSD and three percent in rms levels by neglecting cross modal terms.

It becomes obvious from these observations that the omission of the cross modal terms from the response formulation is an acceptable simplification. This assumption greatly reduces the required computation time and the computer core storage thereby resulting in substantial cost savings and, as shown in References 8, 15, 16 and 17, no appreciable loss in accuracy. The elimination of cross modal terms in the response technique also eliminates the imaginary response. Therefore a co-force cross PSD need only be considered.

Another simplification which can be made in the solution of re-entry vehicle response to re-entry aerodynamic environments is the assumption of a constant pressure cross PSD over each finite element⁽¹⁹⁾. This assumption is predicated upon the high (vs. airplanes) convected velocities (10 to 20 K ft/sec). The argument of the term, $\cos \frac{\xi \omega}{V_c}$, in the spatial correlation function does not change significantly over a separation distance equal to the length of the element. (It should also be pointed out that an upper frequency band of 2000 Hz and a finite element length of approximately three inches is assumed.)

$$\frac{\xi \omega}{V_c} = 0.314 \text{ rad or } 18^\circ$$

The cosine of 18° is 0.95, so no significant reduction in pressure cross PSD would occur.

The last information gained from the literature survey was the way in which Reference 20 handles the variable homogeneous pressure PSD over pairs of finite elements. Their approach is to use a pressure PSD between element pairs equal to the square root of the product of the pressure PSD over each element. This technique was implemented in the response formulations which follow.

2. OPTIMIZED TECHNIQUE

In the development of the optimized technique, the simplifying assumptions discussed in the literature survey were implemented. These assumptions are:

- (1) Cross modal terms can be eliminated,
- (2) Pressure cross PSD is a constant over each finite element, and
- (3) The cross PSD of the response is of little significance and need not be computed.

The starting point in the response formulation is the all-inclusive relationship in which there are no simplifying assumptions, which is

$$\left[\Phi_R(i\omega) \right] = \left[\varphi \right] \left[H^*(i\omega) \right] \left[\varphi \right]^T \left[\Phi_F(i\omega) \right] \left[\varphi \right] \left[H(i\omega) \right] \left[\varphi \right]^T \quad (12)$$

where

$$\begin{aligned}
 [\Phi_F(i\omega)] &= \text{Force cross PSD} \\
 i\omega &= \text{Complex function of frequency} \\
 [H(i\omega)] &= \text{Modal transfer function} \\
 * &= \text{Complex conjugate} \\
 [\varphi] &= \text{Matrix of the mode shapes} \\
 [\Phi_R(i\omega)] &= \text{Output cross PSD}
 \end{aligned}$$

The terms in the modal transfer function matrix, $[H(i\omega)]$, are of the following form

$$\frac{1}{\omega_k^2 M_k \left[1 - \left(\frac{\omega}{\omega_k} \right)^2 + 2i\Gamma \left(\frac{\omega}{\omega_k} \right) \right]} \quad (13)$$

where

$$\begin{aligned}
 \omega_k &= \text{Natural frequency (rad/sec)} \\
 \omega &= \text{Calculation frequency} \\
 \Gamma &= \text{Modal damping as a ratio of the critical value} \\
 M_k &= \text{Generalized mass, equal to 1 if } [\varphi] \text{ is normalized with respect to the mass matrix.}
 \end{aligned}$$

The force cross PSD matrix is obtained from

$$\int_{A_n}^N \int_{A_m}^N \Phi_P(\xi, \eta, i\omega) \begin{Bmatrix} \rho \\ \vdots \\ \rho \end{Bmatrix}_n \begin{Bmatrix} \rho \\ \vdots \\ \rho \end{Bmatrix}_m^T dA_n dA_m \quad (14)$$

where

$\Phi_P(\xi, \eta, i\omega)$ = Pressure cross PSD, variable over the shell element and a function of the separation distances ξ and η .

$\{p\}_n$ = Vector of the displacement functions used to obtain the generalized forces on the n^{th} element.

$\begin{bmatrix} & N \\ & \\ & \end{bmatrix}$ = Assemblage summation process used in setting up finite element master matrices over N elements.

The force cross PSD matrix is Hermitian, comprised of the sum of a real or co matrix which is symmetric and an imaginary or quad matrix which is skew symmetric.

$$\begin{bmatrix} \Phi_F(i\omega) \end{bmatrix} = \begin{bmatrix} \Phi_{FC}(\omega) \end{bmatrix} + i \begin{bmatrix} \Phi_{FQ}(\omega) \end{bmatrix} \quad (15)$$

Let us examine the force cross PSD in light of the simplifying assumptions. If the pressure cross PSD is a constant over each finite element the force cross PSD can be expressed as

$$\begin{bmatrix} \Phi_F(i\omega) \end{bmatrix} = \begin{bmatrix} & N \\ & \\ & \end{bmatrix}_n \begin{bmatrix} & N \\ & \\ & \end{bmatrix}_m \Phi_P(\xi, \eta, i\omega) \begin{Bmatrix} P \end{Bmatrix}_n \begin{Bmatrix} P \end{Bmatrix}_m^T \quad (16)$$

where

ξ, η = Separation distances between the centers of the two elements

$\begin{Bmatrix} P \end{Bmatrix}_n$ = Generalized force vectors for the n^{th} or m^{th} element due to a unit pressure loading

The computer time savings to be gained with this assumption is that the integration over the pairs of finite elements can be eliminated. Even though this assumption is usually valid for re-entry vehicles subjected to aerodynamic loading during re-entry, it will not be valid for the acoustic chamber test environments. Here the effective convected velocity is the speed of sound, which, if a three inch finite element length is assumed, would allow for an upper bound in calculation frequency of only 200 Hz. Therefore in order to correlate with test environments, the form of force cross PSD as given in Equation (14), must be retained.

Neglecting cross modal terms has a significant effect on the response formulation complexity. The response formulation is now reduced to the following form:

$$[\Phi_R(\omega)] = \sum_{k=1}^{n \text{ modes}} \left\{ \varphi \right\}_k H_k^2 \left\{ \varphi \right\}_k^T [\Phi_{F_C}(\omega)] \left\{ \varphi \right\}_k \left\{ \varphi \right\}_k^T \quad (17)$$

The quad force cross PSD drops out because of its skew symmetry.

$$\left\{ \varphi \right\}_k^T [\Phi_{F_Q}(\omega)] \left\{ \varphi \right\}_k = 0$$

The above response formulation greatly reduces the computation time and required computer core storage with, as shown in References 8, 15, 16, and 17, no significant loss of accuracy.

The last simplification results when the calculation of response cross PSD is omitted. In other words, only the diagonal elements of $[\Phi_R(\omega)]$ are computed. Only in a few circumstances would cross PSD response be useful. The diagonal terms are those used in test result comparisons to assess structural integrity and to derive component test specifications. The response formulation then becomes

$$\Phi_{\delta i}(\omega) = \sum_{k=1}^{n \text{ modes}} \varphi_{ik}^2 H_k^2 \left\{ \varphi \right\}_k^T [\Phi_{F_C}(\omega)] \left\{ \varphi \right\}_k \quad (18)$$

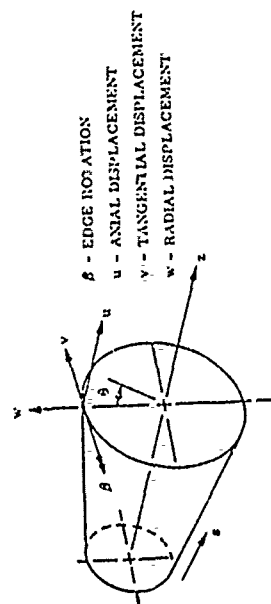
where

φ_{ik} = i^{th} coordinate in the k^{th} mode shape.

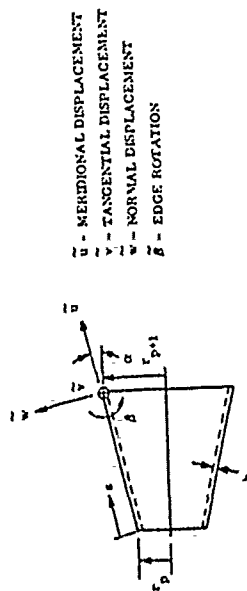
$\Phi_{\delta i}(\omega)$ = PSD of displacement of the i^{th} coordinate.

The different environments are accommodated through proper buildup of the force cross PSD matrix. The following subsections give the details of obtaining the force cross PSD matrix for the different environments. Prior to proceeding into that development, it would be first helpful to examine the SABOR finite element upon which the development is based.

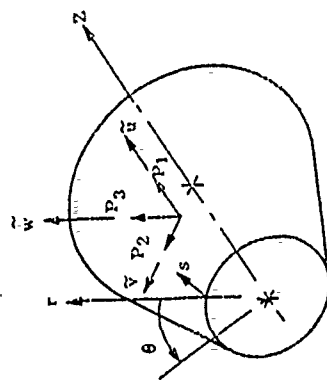
SABOR is a computer program developed at MIT to perform static analyses of shells of revolution via the finite element method. The finite element implemented in the program is a conical frustum. The detailed derivation of the conical frustum element is given in Reference 21. There are four generalized coordinates on each end of the typical element. The coordinates and their sign conventions are shown in Figure 7. In the circumferential direction the



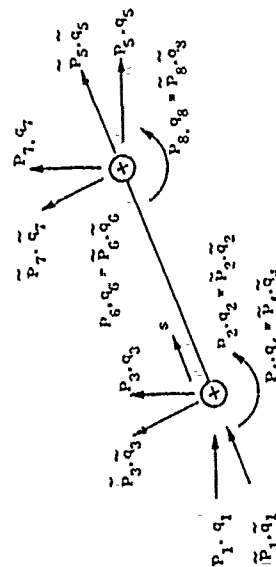
SABOR element shown in u, v, w, β system coordinates



SABOR element shown in u, v, w, β local element coordinates (\tilde{v} is normal to plane of paper)



Applied surface loads and shell displacements on typical conical element



Generalized forces and displacements in the SABOR finite element

Figure 7. SABOR Finite Element Coordinate Conventions

coordinates vary as a Fourier series, e.g. $\cos n\theta$, $\sin n\theta$, where n is the harmonic wave number. The elemental stiffness and mass matrices are constructed such that each harmonic is uncoupled from the other; therefore each harmonic can be analyzed separately and the results superimposed. In this study we are only dealing with the zeroth harmonic, or axial model, and the first harmonic, or lateral model. This is because the beamlike construction of the component areas are not excited by harmonics higher than one. The SABOR shell stiffness is derived through the assumption of a pre-described displacement field. This same displacement field is used in the derivation of the generalized forces under a distributed loading. This is accomplished by equating the virtual work of the generalized forces at the element nodes to the virtual work of the distributed loading over the element. Reference 22 contains the details of this formulation. The integrals for the generalized forces under a unit pressure loading normal to the surface are shown below

$$\begin{aligned}
 \tilde{P}_3 &= \int_0^{2\pi} \int_0^l \left(1 - \frac{3s^2}{l^2} + \frac{2s^3}{l^3} \right) r \cos^2 n\theta \, d\theta \, ds \\
 \tilde{P}_4 &= \int_0^{2\pi} \int_0^l \left(s - \frac{2s^2}{l} + \frac{s^3}{l^2} \right) r \cos^2 n\theta \, d\theta \, ds \\
 \tilde{P}_7 &= \int_0^{2\pi} \int_0^l \left(\frac{3s^2}{l^2} - \frac{2s^3}{l^3} \right) r \cos^2 n\theta \, d\theta \, ds \\
 \tilde{P}_8 &= \int_0^{2\pi} \int_0^l \left(-\frac{s^2}{l} + \frac{s^3}{l^2} \right) r \cos^2 n\theta \, d\theta \, ds
 \end{aligned} \tag{19}$$

The remainder of the forces are zero for normal pressure loading. These elemental forces are related to the generalized system forces by the transformation

$$\{ \underline{P} \} = [\beta] \{ \tilde{P} \} \tag{20}$$

where

$$[\beta] = \begin{bmatrix} \cos \alpha & 0 & -\sin \alpha & 0 & 0 & 0 & 0 & 0 \\ 0 & 1 & 0 & 0 & 0 & 0 & 0 & 0 \\ \sin \alpha & 0 & \cos \alpha & 0 & 0 & 0 & 0 & 0 \\ 0 & 0 & 0 & 1 & 0 & 0 & 0 & 0 \\ 0 & 0 & 0 & 0 & \cos \alpha & 0 & -\sin \alpha & 0 \\ 0 & 0 & 0 & 0 & 0 & 1 & 0 & 0 \\ 0 & 0 & 0 & 0 & \sin \alpha & 0 & \cos \alpha & 0 \\ 0 & 0 & 0 & 0 & 0 & 0 & 0 & 1 \end{bmatrix} \quad (21)$$

and $\alpha =$ Cone half angle.

It should be observed that the circumferential integration is independent of the meridional integration. This is important, as the force cross PSD will be evaluated in two steps, first the circumferential integration and second the meridional. Because the mode shape variation in theta is known ($\cos n\theta$), this integral can be evaluated in closed form and multiplied by the meridional results.

3. RE-ENTRY VIBRATION RESPONSE

In Section III it was shown that the narrowband spatial correlation function for attached turbulent flow can be represented as:

$$C(\xi, \eta, \omega) = e^{-\frac{c_1 |\xi|}{\delta^*}} e^{-\frac{c_2 |\eta|}{\delta^*}} \cos \frac{\omega \xi}{V_c} \quad (22)$$

In cylindrical coordinates the above is

$$C(\Delta s, \Delta \theta, \omega) = e^{-\frac{c_1 |s_2 - s_1|}{\delta^*}} e^{-\frac{c_2 |r_2 \theta_2 - r_1 \theta_1|}{\delta^*}} \cos \frac{\omega(s_2 - s_1)}{V_c} \quad (23)$$

where

δ^* and V_c are now the average boundary layer displacement thickness and convection velocity between locations s_1 and s_2 .

Now in exact form the force cross PSD between the two elements k and m would be

$$\sqrt{\phi_m^{(f)} \phi_k^{(f)}} \int_{\Lambda_k} \int_{\Lambda_m} C(\Delta s, \Delta \theta, \omega) \left\{ \rho \right\}_k \left\{ \rho \right\}_m^T d\Lambda_k d\Lambda_m \quad (24)$$

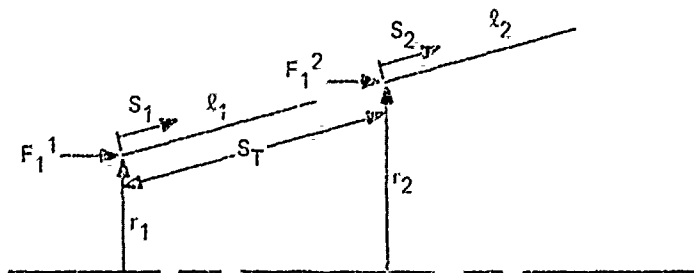
where

$\{p\}_k$ = Expressions in the integrals of Equations (1) given previously
 $\phi_k(f)$ = Homogeneous pressure PSD over element k.

A typical term in the above relation would then be

$$\begin{aligned} \phi_{F_1^1 F_1^2} &= \sin^2 \alpha \sqrt{\phi_1(f) \phi_2(f)} \int_0^{2\pi} \int_0^{2\pi} \int_0^{\ell_1} \int_0^{\ell_2} \left(1 - \frac{3s_1^2}{\ell_1^2} + \frac{2s_1^3}{\ell_1^3} \right) \\ &\quad \left(1 - \frac{3s_2^2}{\ell_2^2} + \frac{2s_2^3}{\ell_2^3} \right) r_1 r_2 e^{-\frac{c_1 |s_T + s_2 - s_1|}{\delta^*}} \\ &\quad e^{-\frac{c_2 |r_2 \theta_2 - r_1 \theta_1|}{\delta^*}} \\ &\quad \cos \frac{\omega(s_T + s_2 - s_1)}{V_c} \cos n \theta_1 \cos n \theta_2 d\theta_1 d\theta_2 ds_1 ds_2 \end{aligned} \quad (25)$$

where s_T is the meridional distance from the beginning of element 1 to the beginning of element 2. The term $\sin^2 \alpha$ comes from the transformation matrix, Equation (21), on both elements.



The integration with respect to θ can be performed separately as

$$\int_0^{2\pi} \int_0^{2\pi} \frac{c_2 |r_2 \theta_2 - r_1 \theta_1|}{\delta^*} \cos n \theta_1 \cos n \theta_2 d\theta_1 d\theta_2 \quad (26)$$

Since the above expression is independent of the driving frequency, it can be evaluated for each pair of elements and multiplied by the results of the meridional integration, which does change with driving frequency. In performing the integration, care must be taken to integrate over the proper areas to account for the absolute sign. For the zeroth harmonic or $n = 0$ the integration yields the circumferential joint acceptance:

$$J_{\theta\theta}^0 = \frac{\delta^* 4\pi}{r_2 c_2} + \frac{\delta^{*2}}{c_2 r_1 r_2} \left[e^{\frac{-2\pi c_2 r_2}{\delta}} + e^{\frac{-2\pi c_2 r_1}{\delta^*}} - e^{\frac{-2\pi c_2 (r_2 - r_1)}{\delta}} - 1 \right] \quad (27)$$

It is observed that for turbulent boundary layer pressure fluctuations in which r/δ^* is greater than one and $c_2 = 1$, that only the first term is significant. $J_{\theta\theta}^0$ therefore is approximated as

$$\frac{\delta^* 4\pi}{r_2 c_2} \quad (28)$$

For higher harmonics in which n is 1 or greater a considerably more complex expression for $J_{\theta\theta}^n$ results.

$$J_{\theta\theta}^n = \frac{\frac{r_1 c_2}{\delta^*} \left[\frac{c_2}{\delta^*} (r_2 - r_1) \right] \left[1 - e^{\frac{-c_2}{\delta^*} (r_2 - r_1) 2\pi} \right]}{\left[\left(\frac{r_1 c_2}{\delta^*} \right)^2 + n^2 \right] \left[\left(\frac{c_2}{\delta^*} (r_2 - r_1) \right)^2 + 4n^2 \right]} - \frac{2n^2 \left(\frac{r_1 c_2}{\delta^*} \right) \left[e^{\frac{-c_2}{\delta^*} (r_2 - r_1) 2\pi} - 1 \right]}{\left[\left(\frac{r_1 c_2}{\delta^*} \right)^2 + n^2 \right] \left[\left(\frac{c_2}{\delta^*} (r_2 - r_1) \right)^2 + 4n^2 \right] \left[\frac{c_2}{\delta^*} (r_2 - r_1) \right]} +$$

$$\begin{aligned}
& + \frac{n^2 \left[1 - e^{-\frac{c_2}{\delta^*} (r_2 - r_1) 2\pi} \right]}{\left[\left(\frac{c_2}{\delta^*} (r_2 - r_1) \right)^2 + 4n^2 \right] \left[\left(\frac{r_1 c_2}{\delta^*} \right)^2 + n^2 \right]} + \frac{\frac{r_2 c_2}{\delta^*} \left[e^{-\frac{2\pi c_2 r_2}{\delta^*}} - 1 \right] \frac{r_1 c_2}{\delta^*}}{\left[\left(\frac{r_2 c_2}{\delta^*} \right)^2 + n^2 \right] \left[\left(\frac{r_1 c_2}{\delta^*} \right)^2 + n^2 \right]} + \\
& \frac{\frac{2 r_2 c_2}{\delta^*} \left[\frac{\sin [2\pi (n + n r_1 / r_2)]}{2 (n + n r_1 / r_2)} + \frac{\sin [2\pi (n - n r_1 / r_2)]}{2 (n - n r_1 / r_2)} \right]}{\left[\left(\frac{c_2 r_2}{\delta^*} \right)^2 + n^2 \right]} +
\end{aligned}$$

$$\begin{aligned}
& \frac{\frac{r_1 c_2}{\delta^*} \left[e^{-\frac{2\pi c_2 r_1}{\delta^*}} - 1 \right] \frac{r_2 c_2}{\delta^*}}{\left[\left(\frac{r_2 c_2}{\delta^*} \right)^2 + n^2 \right] \left[\left(\frac{r_1 c_2}{\delta^*} \right)^2 + n^2 \right]} + \frac{n^2 \left[1 - e^{-\frac{c_2}{\delta^*} 2\pi (r_2 - r_1)} \right]}{\left[\left(\frac{r_2 c_2}{\delta^*} \right)^2 + n^2 \right] \left[\left(\frac{c_2}{\delta^*} (r_2 - r_1) \right)^2 + 4n^2 \right]} +
\end{aligned}$$

(29)

$$\begin{aligned}
& \frac{\left(\frac{r_2 c_2}{\delta^*} \right) \left(\frac{c_2}{\delta^*} (r_2 - r_1) \right) \left[e^{-\frac{c_2}{\delta^*} (r_2 - r_1) 2\pi} - 1 \right]}{\left[\left(\frac{r_2 c_2}{\delta^*} \right)^2 + n^2 \right] \left[\left(\frac{c_2}{\delta^*} (r_2 - r_1) \right)^2 + 4n^2 \right]} +
\end{aligned}$$

$$\begin{aligned}
& \frac{2 n^2 \left(\frac{r_2 c_2}{\delta^*} \right) \left[e^{-\frac{c_2}{\delta^*} (r_2 - r_1) 2\pi} - 1 \right]}{\left[\left(\frac{r_2 c_2}{\delta^*} \right)^2 + n^2 \right] \left[\left(\frac{c_2}{\delta^*} (r_2 - r_1) \right)^2 + 4n^2 \right] \left[\frac{c_2}{\delta^*} (r_2 - r_1) \right]}
\end{aligned}$$

The remainder of the integration of Equation (25) is associated with the meridional direction and varies depending upon the assumption that the pressure PSD is constant or not. If the pressure PSD is considered constant over the individual elements, the spatial correlation function is removed from the integrals and evaluated based on the separation distance between the element centers, e.g.

$$\Phi_{F_1^1 F_1^2} = \sqrt{\phi_1(f) \phi_2(f)} \int_{-2}^n \sin^2 \alpha e^{-\frac{c_1}{\delta^*} \left| s_T + \frac{1}{2} (\ell_2 - \ell_1) \right|} \cos \left[\frac{\omega (s_T + \frac{1}{2} (\ell_2 - \ell_1))}{V_c} \right] \int_0^{\ell_1} r_1 \left(1 - \frac{3s_1^2}{\ell_1^2} + \frac{2s_1^3}{\ell_1^3} \right) ds_1 \int_0^{\ell_2} r_2 \left(1 - \frac{3s_2^2}{\ell_2^2} + \frac{2s_2^3}{\ell_2^3} \right) ds_2 \quad (30)$$

The integral expressions can be evaluated initially for each of the generalized forces on an element and stored at the beginning of the computations for use thereafter.

If the constant PSD assumption is not valid (as in acoustic chambers), the meridional integration must be carried out for each pair of elements at each new driving frequency and the spatial correlation function must of course be included in the integration. The form of the equation thus becomes

$$\Phi_{F_1^1 F_1^2} = \sqrt{\phi_1(f) \phi_2(f)} \int_{-2}^n \sin^2 \alpha \int_0^{\ell_2} \int_0^{\ell_1} r_1 \left(1 - \frac{3s_1^2}{\ell_1^2} + \frac{2s_1^3}{\ell_1^3} \right) r_2 \left(1 - \frac{3s_2^2}{\ell_2^2} + \frac{2s_2^3}{\ell_2^3} \right) e^{-\frac{c_1 |s_T + s_2 - s_1|}{\delta^*}} \cos \left[\frac{\omega}{V_c} (s_T + s_2 - s_1) \right] ds_1 ds_2 \quad (31)$$

The force cross PSD expressed as Equation (31) is numerically evaluated using the trapezoidal rule of integration. For each pair of elements, sixteen separate integrations are involved. The transformation matrix of Equation (21) is used to expand the 4 x 4 matrix to the required 8 x 8 matrix for each element pair.

Thus far only the force cross PSD for SABOR finite elements has been discussed. For the beam-column type finite elements used to model the nose section, a reduced number of coordinates per element is used. In the axial model (zeroth harmonic) only two coordinates per element are required. For the lateral model (first harmonic) four coordinates per

element are required. If a generalized force set were derived for these axial and lateral coordinates, it would be based on a linear displacement function in the axial model and a cubic displacement function in the lateral model. It develops that the generalized force expressions for SABOR radial and rotational coordinates are identical to those for a beam with an assumed cubic displacement function. The SABOR axial generalized force expressions are sufficiently accurate to use for axial nose forces, therefore the same expressions used for SABOR generalized forces can be applied in the nose sections, eliminating the need for separate theory and checks in the computer codes.

4. REVERBERANT CHAMBER RESPONSE

Development for the force cross-PSD matrix as applied to an acoustic chamber operating in the reverberant mode will now be discussed. The spatial correlation function can be described as:

$$C(\xi, \eta, \omega) = \frac{\sin \frac{\omega}{c} \xi}{\frac{\omega}{c} \xi} \frac{\sin \frac{\omega}{c} \eta}{\frac{\omega}{c} \eta} \quad (32)$$

where

c = Sonic velocity

ξ, η = Separation distances

ω = Frequency

In the cylindrical coordinate system the above expression would be:

$$C(\Delta s, \Delta \theta, \omega) = \frac{\sin \left[(s_2 - s_1) \frac{\omega}{c} \right]}{(s_2 - s_1) \frac{\omega}{c}} \frac{\sin \left[(r_2 \theta_2 - r_1 \theta_1) \frac{\omega}{c} \right]}{(r_2 \theta_2 - r_1 \theta_1) \frac{\omega}{c}} \quad (33)$$

The above expression then replaces the narrowband spatial correlation function for turbulent flow in Equation (25) to obtain the terms required in the force cross PSD matrix for reverberant chambers. Numerical integration will be used meridionally, as in Equation (31).

Circumferentially, the reverberant spatial correlation function results in the following expression for the joint acceptance:

$$J_{\theta \theta}^{n_{1-2}} = \int_0^{2\pi} \int_0^{2\pi} \frac{\sin \left[\frac{\omega}{c} (r_2 \theta_2 - r_1 \theta_1) \right]}{\frac{\omega}{c} (r_2 \theta_2 - r_1 \theta_1)} \cos n \theta_2 \cos n \theta_1 d \theta_2 d \theta_1 \quad (34)$$

The closed-form integration of the above yields sine and cosine integrals

$$\left(\int_0^z \frac{\sin x}{x} dx, \int_0^z \frac{1 - \cos x}{x} dx \right)$$

which must be evaluated in series expressions, rational fraction approximations or asymptotic expansions depending upon z . Therefore the computer implementation was again accomplished via numerical integration.

The basic response formulation of Equation (18) then holds with $\left[\Phi_{Fc}(\omega) \right]$ developed as just described.

5. PROGRESSIVE WAVE CHAMBER RESPONSE

The narrowband spatial correlation function representative of an acoustic chamber operating in the progressive mode can be described as:

$$C(\xi, \eta, \omega) = \cos \left[\frac{\omega \xi}{c} \cos \psi \right] \quad (35)$$

where

$$\psi = \text{Incident angle.}$$

It is assumed that the vehicle is placed in the chamber such that the sound waves pass over the vehicle in the direction of its axis. Therefore in the cylindrical coordinate system the above expression is

$$C(\Delta s, \omega) = \cos \left[\frac{\omega (s_2 - s_1)}{c} \cos \psi \right] \quad (36)$$

It is observed that circumferentially there is perfect correlation. This means that the $J_{\theta\theta}$ integration of Equation (34) is simply

$$J_{\theta\theta}^{n_{1-2}} = \int_0^{2\pi} \int_0^{2\pi} \cos n_{\theta_1} \cos n_{\theta_2} d\theta_1 d\theta_2 = \begin{cases} 4\pi^2 & n = 0 \\ 0 & n > 0 \end{cases} \quad (37)$$

Thus under ideal progressive conditions only the axial or zeroth harmonic modes of vibration can be excited.

The force cross PSD development for the meridional direction is the same as Equation (31), except that Equation (36) is substituted in place of the turbulent boundary layer correlation functions.

6. COMPUTER PROGRAMS

The response formulations developed in this Section have been implemented into computer programs. A separate program has been written to compute the re-entry vehicle vibration response to each of the environments discussed. These programs and associated users manuals are available through the Air Force Flight Dynamics Laboratory/F

The program which computes the response of a re-entry vehicle to re-entry environments is named REVIB. This program is developed to accept vehicle dynamic characteristics of a model based on SABCR shell finite elements and beam finite elements. It is assumed that the dynamic model frequencies and mode shapes are computed using existing in-house programs for this purpose and the results stored on tape in formats compatible with the REVIB computer program. In addition to the dynamic model input, parameters required to describe the aero-acoustic environment must be input. These parameters which are described versus vehicle station include boundary layer displacement thickness, convection velocity and overall mean square dynamic pressure. In addition the decay constants in the spatial correlation functions must be input. Finally, vehicle and finite element geometry, which are utilized for the internal generation of discrete force cross PSD's from the distributed pressures, must be input.

The input is required for both the forebody and the aft cover if both forebody transitional or turbulent flow and wake flow is considered. The input can be restricted to merely the forebody parameters if wake flow excitations are omitted from the forcing function. In addition capability exists to input discrete force PSDs representative of shock loadings. This is an option which is exercised only if shock loads are anticipated on the vehicle.

The response formulation of equation (18) is computerized. In order to keep REVIB as general as possible the force cross PSD formulation described by equation (14) is programmed. Output from REVIB consists of response power spectral density values at all degrees of freedom for either or both acceleration and displacement at all of the frequencies selected by the user for calculations. In addition, overall root mean square values for each coordinate power spectral density are printed. Similar response output is also provided for the quantities computed by matrices transforming acceleration or displacement.

PROG and REVERB are the programs which compute re-entry vehicle vibration response to the ground test acoustic environments associated with ideal progressive wave chambers and reverberant chambers. Input to these programs consists, in addition to the finite element geometry, of sound pressure levels at the calculation frequencies for the vehicle forebody and its base. Output is identical to the REVIB program.

In addition a fourth program was written which computes the re-entry vehicle vibration response to acoustic environments representative of the Flight Dynamics Laboratory Sonic Fatigue Facility. This program is named SOFAFA. Input is identical to PROG and REVERB and output the same as REVIB. This acoustic environment is described fully in Section VIII of the report.

SECTION V

PROTOTYPE VEHICLE DYNAMIC CHARACTERISTICS

1. DEFINITION OF PROTOTYPE VEHICLE

The prototype vehicle supplied for this study was a Fuzing and Arming Test and Evaluation Program (FATE) re-entry vehicle. It is a conical vehicle with a 4.5 degree half cone angle, approximately 85 inches long. The substructure is aluminum and the heat shield is carbon phenolic. There are three sections to the vehicle structure and two component packages. The nose section is screwed to the midsection and the mid and aft sections are joined through a bolted flange. One component package is essentially a shelf traversing almost the entire internal midsection. The second component package occupies approximately half of the aft section. More details and a schematic of the vehicle are given in the following subsection (Figure 8).

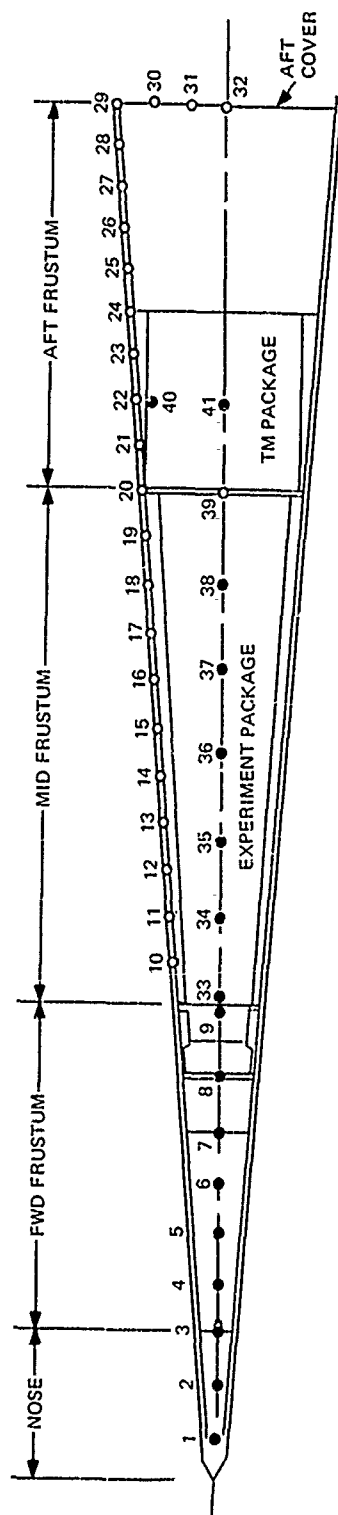
2. DYNAMIC MODEL

The prototype vehicle was modeled using beam and shell (SABOR) finite elements. Node identification and typical coordinate definition for axial and lateral dynamic models are given in Figure 8. Coordinate identification is given in Table I. The axial dynamic model has 86 degrees of freedom whereas the lateral dynamic model required 127 degrees of freedom for its description. An item-by-item weight breakdown is contained in Table II.

A nose fixture was used for testing rather than the prime nose; therefore the nose fixture was modeled using beam finite elements. The forward frustum is either completely solid (heavy ballast) or a very thick shell. This portion of the prototype vehicle was also modeled using beam finite elements.

As seen in the dynamic model of Figure 8, the mid and aft frusta and aft cover are modeled using SABOR shell finite elements. The first node of the mid frustum was transformed from shell coordinates to beam coordinates to connect with the beam-modeled forward frustum. Two complex joints exist at the mid-to-aft frustum interface and aft frustum-to-aft cover interface. Details of modeling in these two areas are shown in Figure 9. Local discontinuities of these types usually provide high flexibility, which considerably affects gross vehicle bending and axial modes. The joints at the nose-to-forward frustum interface and forward-to-mid frustum interface are good threaded joints and should not exhibit high local flexibility.

The experiment package, because of its length and continuous support structure, was modeled using beam finite elements. The weight of the attached components is distributed along the support structure. The bulkhead attaching the support structure to the mid-aft frustum joint (node 20) was modeled using SABOR shell elements, as shown in Figure 10. The shell coordinates at the inner node are transformed to beam coordinates to attach to the beam modeled experiment package (node 39). A light spring was used in the lateral model only, between the forward end of the experiment package and the forward-to-mid frustum joint to replace the 0.010 inch air gap. This connection slips axially.



TYPICAL COORDINATES	
AXIAL MODEL	LATERAL MODEL

Figure 8. Dynamic Model

TABLE I. COORDINATES AT NODES

Node Number	Station Number	Coordinate Number						
		Axial Model			Lateral Model			
		u	w	β	u	v	w	β
1	17.9	1	--	--	--	--	1	2
2	21.	2	--	--	--	--	3	4
3	24.1	3	--	--	--	--	5	6
4	27.2	4	--	--	--	--	7	8
5	30.3	5	--	--	--	--	9	10
6	33.4	6	--	--	--	--	11	12
7	36.5	7	--	--	--	--	13	14
8	39.6	8	--	--	--	--	15	16
9	42.6	9	--	--	--	--	17	18
10	45.6	10	11	12	19	20	21	22
11	48.6	13	14	15	23	24	25	26
12	51.6	16	17	18	27	28	29	30
13	54.6	19	20	21	31	32	33	34
14	57.6	22	23	24	35	36	37	38
15	60.6	25	26	27	39	40	41	42
16	63.6	28	29	30	43	44	45	46
17	66.6	31	32	33	47	48	49	50
18	69.6	34	35	36	51	52	53	54
19	72.6	37	38	39	55	56	57	58
20	75.5	40	41	42	59	60	61	62
21	78.2	43	44	45	63	64	65	66
22	80.9	46	47	48	67	68	69	70
23	83.6	49	50	51	71	72	73	74
24	86.2	52	53	54	75	76	77	78
25	88.9	55	56	57	79	80	81	82
26	91.5	58	59	60	83	84	85	86
27	94.2	61	62	63	87	88	89	90
28	96.8	64	65	66	91	92	93	94
29	99.4	67	68	69	95	96	97	98
30	99.4	70	71	72	99	100	101	102
31	99.4	73	74	75	103	104	105	106
32	99.4	76	77	78	107	108	109	110
33	42.6	79	--	--	--	--	111	112
34	50.0	80	--	--	--	--	113	114
35	54.7	81	--	--	--	--	115	116
36	60.0	82	--	--	--	--	117	118
37	66.3	83	--	--	--	--	119	120
38	72.1	84	--	--	--	--	121	122
39	75.5	85	--	--	--	--	123	124
40	82.0	--	--	--	--	--	125	126
41	82.0	86	--	--	--	--	127	--

NOTE - v coordinate in axial model not used since this defines torsion motion only.

TABLE II. WEIGHT BREAKDOWN

Item	Weight (Lbs.)
Nose, prime	4.07
Nose fixture, axial	4.23
Nose fixture, lateral	3.69
Forward frustum	45.64
Mid frustum	34.50
Aft frustum	37.16
Aft Cover	1.65
Experiment Package	36.98
TM Package	24.48
TOTAL (PRIME)	184.48

The telemetry (TM) package is described with two mass points in the lateral model. Internal components are mounted on two connected webs. These components are treated as one (node 41) and the web bending stiffness is used to connect them to the package outer structure (node 40). Components mounted on the support bulkhead are also modeled at node 40. Axially, all support structure is stiff enough that the total TM package is treated as one mass point (node 41). The bulkhead attaching the support structure to the aft frustum (node 24) is modeled using SABOR shell elements, as shown in Figure 10. The shell coordinates at the inner mode are transformed to beam coordinates to pick up the TM package degrees of freedom. An O-ring exists between the forward end of the TM package and the aft end of the experiment package. This was modeled as a linear spring for the lateral model and as a slip joint axially.

3. MODAL SURVEY SUMMARY

The dynamic model verification test program included axial and lateral modal surveys that established vehicle shell and internal component modal frequencies in the 20 to 2000 Hz frequency range. The mode shapes associated with resonant frequencies were ascertained in the vehicle meridional and circumferential directions. The meridional stations, in particular, were consistent with the nodes chosen in the dynamic model construction to facilitate ease of correlation. Stations at either side of significant structural or load transfer discontinuities were of particular concern because experience has shown that these areas can be large contributors to poor dynamic model correlation.

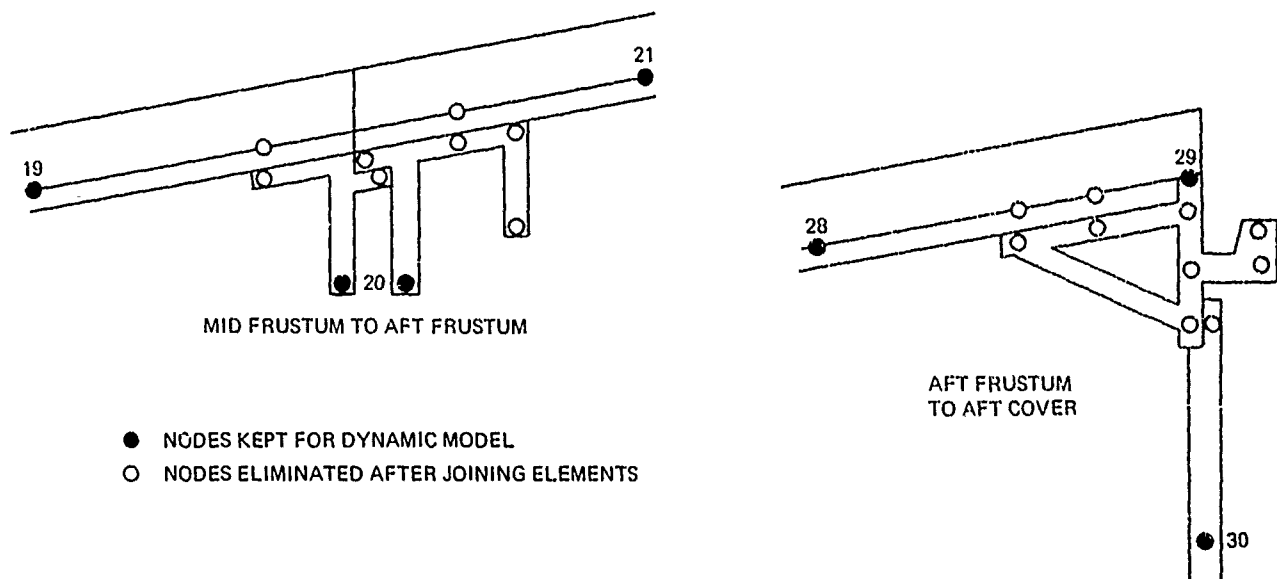


Figure 9. Sabor Modeling of Shell Joints

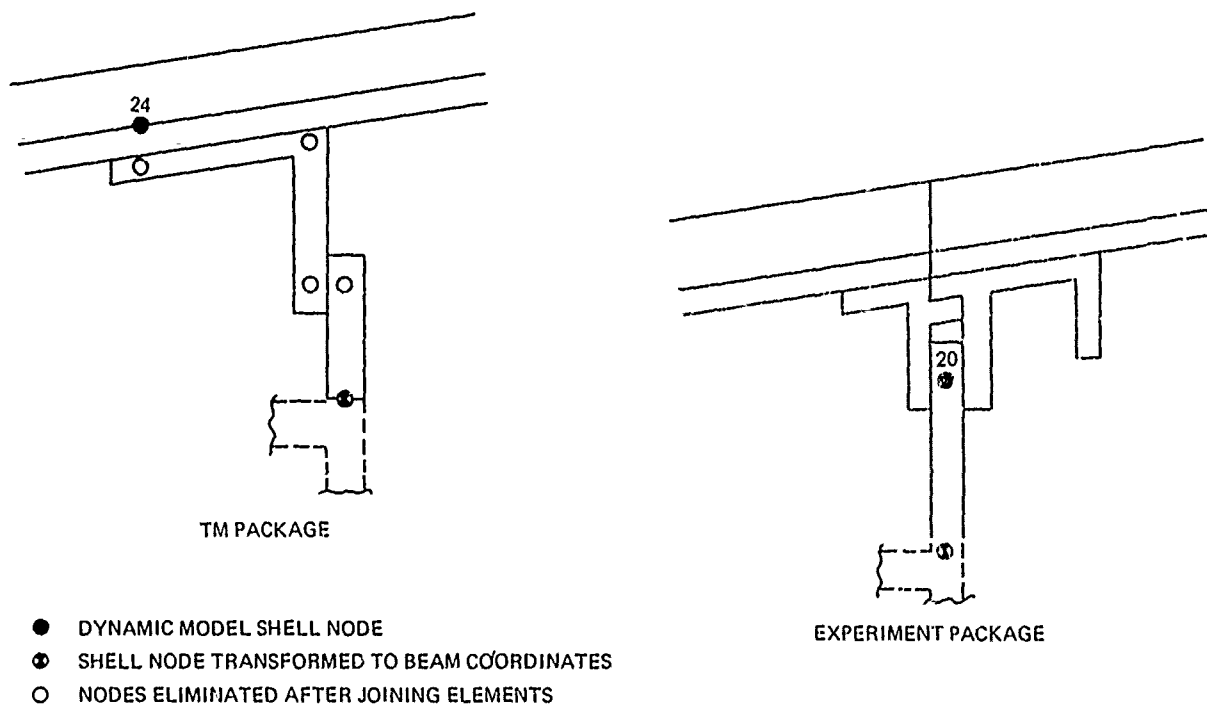


Figure 10. Sabor Modeling of Bulkhead Attachments

The modal surveys provided quadrature and in-phase response versus frequency data from which resonant frequencies and structural damping coefficients, respectively, were determined. The modal surveys also provided quadrature responses versus vehicle station (meridional and circumferential) which are the mode shapes. These resonant frequencies, mode shapes, and damping coefficients were used to:

- (1) Verify the dynamic model, thereby providing a firm basis for evaluating acoustic effects on vehicle response;
- (2) Indicate areas, if any, where the modeling techniques can be improved to more closely simulate vehicle characteristics; and
- (3) Provide structural damping data for use in acoustic response predictions.

The nosetip was not used during the modal surveys. Upon inspection of the nosetip, it was concluded that possible damage or degradation could occur because of the manner in which the nosetip is attached to the vibration fixture. Hence, the nosetip was replaced by a GE-designed nosetip adapter with similar mass and stiffness properties and allowing simple attachment to vibration fixture.

The test was designed so that a lightweight shaker armature could be used. This weight was necessarily small with respect to the test specimen, since the modal frequencies and mode shapes are functions of the entire spring mass system, which includes the shaker armature.

In keeping with low weight fixtures, the suspension system for both axial and lateral vibration consisted of bungee shock cord. Included in the lines were turnbuckles for height adjustment. The natural frequency of the suspended system was less than 5 Hz. This suspension system supported the vehicle in a vertical position, nose down, creating a free-free condition corresponding to free flight. Figure 11 shows the modal survey test setup.

During the axial and lateral modal testing, the location of one shell response accelerometer was changed to accommodate the various phases of testing, i.e., for meridional and circumferential mode shape definition.

Twelve accelerometers were affixed to the test vehicle for shell and internal component monitoring during both the modal survey and acoustic test. Six were located on the component shelf in the midsection and four were placed in the telemetry package in the aft section. Also, one each was attached internally to the midsection and aft section liners. Figure 12 shows a schematic of the instrumented vehicle.

In addition to the twelve accelerometers to monitor component response, four strain gages and two microphones were also included in the internal instrumentation. The strain gages were mounted in the vehicle substructure (Figure 12) and the microphones in the two component packages. Neither the strain gages nor microphones were utilized during the modal survey; however they were used in the acoustic test (SECTION VII). Table III gives the internal sensor descriptions.

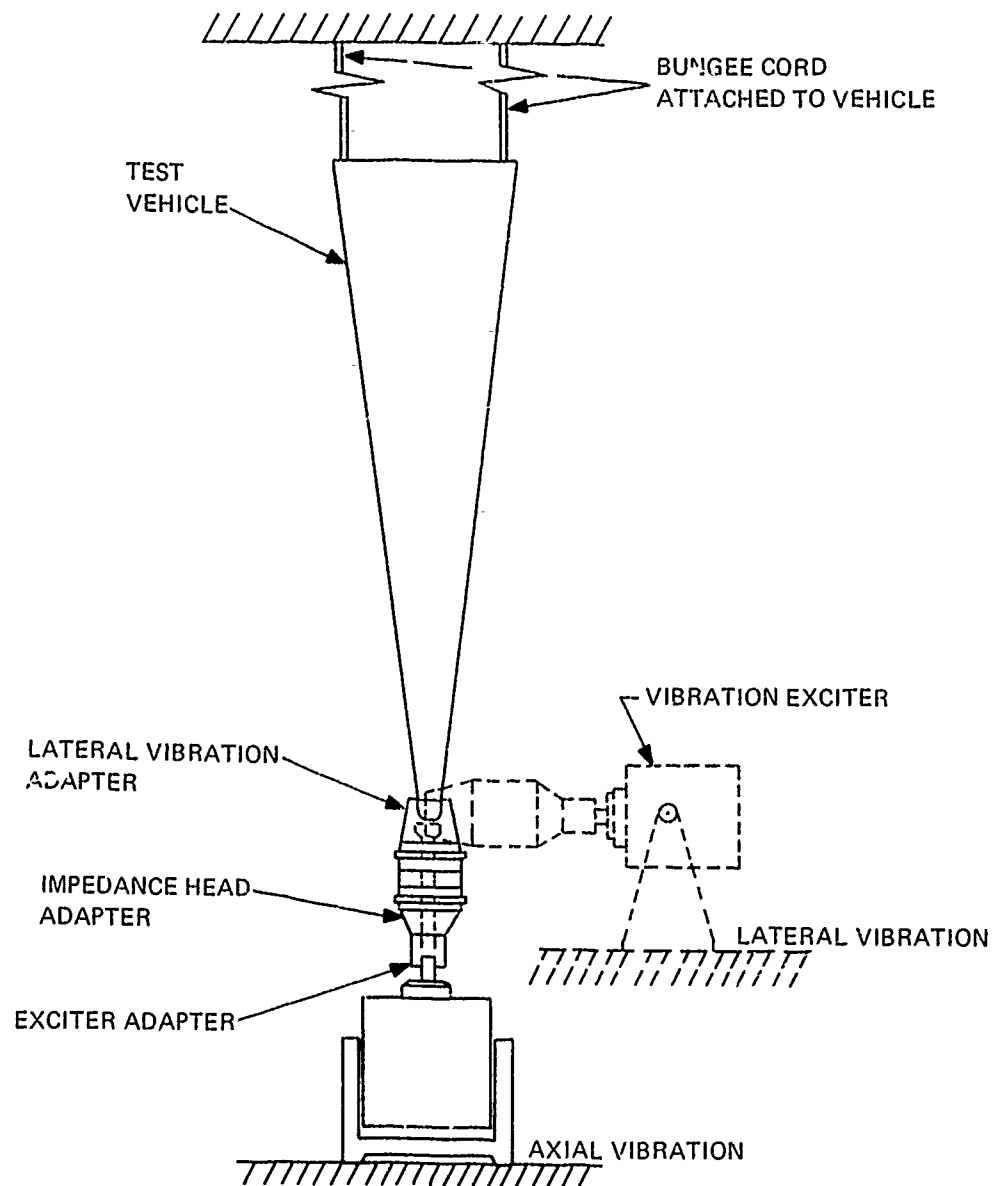
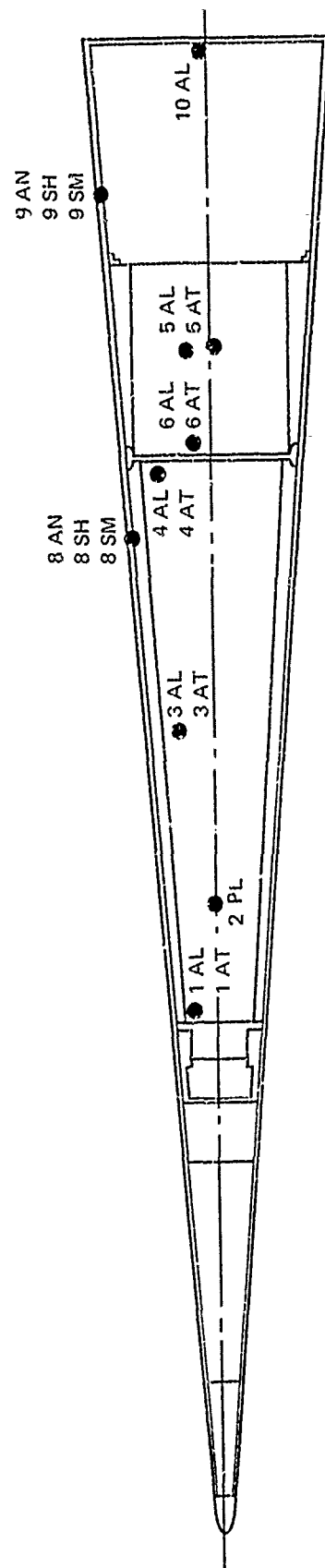


Figure 11. Modal Survey Test Setup



INSTRUMENTATION CODES	
TYPE	DIRECTION
A - ACCELEROMETER	L - LONGITUDINAL
S - STRAIN GAGE	T - TRANSVERSE
P - MICROPHONE	N - NORMAL
	H - HOOP
	M - MERIDIONAL

Figure 12. Schematic of Sensor Identification and Location

TABLE III. SENSOR DESCRIPTION

Ident	Type	Measurement Direction	Vendor	Model
1AL	Accel	Long.	ENDEVCO	2213
1AT	Accel	Trans.	ENDEVCO	2213
2PL	Phone	Long.	B&K	4133
3AL	Accel	Trans.	ENDEVCO	2213
3AT	Accel	Trans.	ENDEVCO	2213
4AL	Accel	Long.	ENDEVCO	2213
4AT	Accel	Trans.	ENDEVCO	2213
5AL	Accel	Long.	ENDEVCO	2213
5AT	Accel	Trans.	ENDEVCO	2213
6AL	Accel	Long.	ENDEVCO	2213
6AT	Accel	Trans.	ENDEVCO	2213
7PL	Phone	Long.	B&K	4133
9AN	Accel	Normal	CRL	606-3-I
8SH	Strain	Hoop	Micro-Measurements	EA-13-250TM-120
8SM	Strain	Merid.	Micro-Measurements	EA-13-250TM-120
9AN	Accel	Normal	CRL	606-3-I
9SH	Strain	Hoop	Micro-Measurements	EA-13-250TM-120
9SM	Strain	Merid.	Micro-Measurements	EA-13-250TM-120
10AL	Accel	Long.	ENDEVCO	2213

4. FREQUENCIES, MODE SHAPES AND DAMPING

The modal survey pointed out the need for modifying the dynamic models. The calculated stiffness coefficients for the telemetry package bulkhead-ring combination, aft field joint and aft cover were modified in order to minimize differences between analytical and experimental dynamic characteristics of the vehicle. In the axial model the most sensitive area, i.e., the area in which change in stiffness had the most affect on the mode shape, was in the telemetry package bulkhead-ring combination. In the lateral dynamic model, the stiffness coefficient representing a linear spring that couples the forward end of the experiment package to the forward section of the vehicle was increased to obtain frequency similitude between analysis and test.

Comparisons of the analytically and experimentally obtained frequencies for the axial and lateral models are presented in Tables IV and V, respectively, along with mode descriptions and the experimentally determined structural damping.

Figures 13 through 17 are comparisons of the mode shapes obtained from the analyses and the modal surveys. The modes chosen for presentation are based on the magnitude of the modal responses computed by the response prediction analyses, i.e., those modes portraying the highest modal forces and most significant modal responses at the internal accelerometer locations were chosen.

The ordinate variable defines relative motion along the vehicle within any particular mode. Thus the mode shapes must be normalized in some manner. The normalization technique used on the mode shapes, in the figure is such that each modal mass is unity, that is

$$\varphi^T M \varphi = I$$

where

φ = The matrix of mode shape values

M = The system mass matrix

I = The unity matrix

The following legend is provided for interpretation of the plotting symbols appearing in the figures.

⊙ = Quadrature response versus vehicle station taken during dwelling at resonant frequency

△ = Quadrature response of experiment package measurements taken during sine sweeps

□, ◇ = Quadrature response of telemetry package measurements taken during sine sweeps

TABLE IV. COMPARISON OF AXIAL EXPERIMENTAL AND ANALYTICAL FREQUENCIES

Experimental (Hz)	Analytical (Hz)	Mode Description	Structural Damping Coefficient
319.4	339.0	First EP Mode	0.04
368.0	346.0	First Shell Elastic; TM and EP	0.047
442.0	--	Very Little Motion	0.03
478.0	--	Very Little Motion	0.03
535.0	525.0	Aft Cover	0.03
639.0	649.0	TM Mode; Shell Elastic and EP (See Figure 13)	0.032
1335.0	1133.0	Shell Elastic and EP	0.03
1380.0	1306.0	Second Shell Elastic (See Figure 14)	0.037

Note: EP - Experiment Package

TM - Telemetry Package

The unlabeled solid line represents relative displacement associated with the main shell structure of the vehicle. The solid lines labeled EP and TM represent the experiment package and telemetry package displacements relative to themselves and to the main structure. The dotted lines are shown to locate the vehicle station from which the component packages are attached. Physically, the length of the dotted line represents the relative displacement between the vehicle and the component shell attachment. This displacement, of course, defines the amount of bulkhead distortion.

Since the mode shapes represent the numbers used in the response analysis to describe coordinate displacements, etc., those modes which exhibit the largest shell deviations from the origin of the ordinate axis would be expected to show the greatest response. This is especially true for the last 30 inches of the vehicle as the greatest surface area is present, thus resulting in larger forces.

TABLE V. COMPARISON OF LATERAL EXPERIMENTAL AND ANALYTICAL FREQUENCIES

Experimental (Hz)	Analytical (Hz)	Mode Description	Structural Damping Coefficient
74	75	EP Rocking	0.068
--	98	TM Motion	--
135	134	Vehicle First Elastic (See Figure 15)	0.059
240	232	Vehicle Second Elastic	0.029
260	268	EP Motion; Vehicle Elastic	0.03
326	353	EP First Elastic (See Figure 16)	0.045
460	--	TM and Vehicle Elastic	0.04
534	580	Vehicle Third Elastic (See Figure 17)	0.026
730	731	EP Second Elastic; TM and Vehicle Elastic	0.074
926	1034	Vehicle Fourth Elastic	0.055
--	1118	Aft Cover (Not Surveyed)	--
1207	1228	Vehicle Fifth Elastic, EP	0.038
1425	1447	Vehicle Elastic, EP	0.053

Note: EP - Experiment Package

TM - Telemetry Package

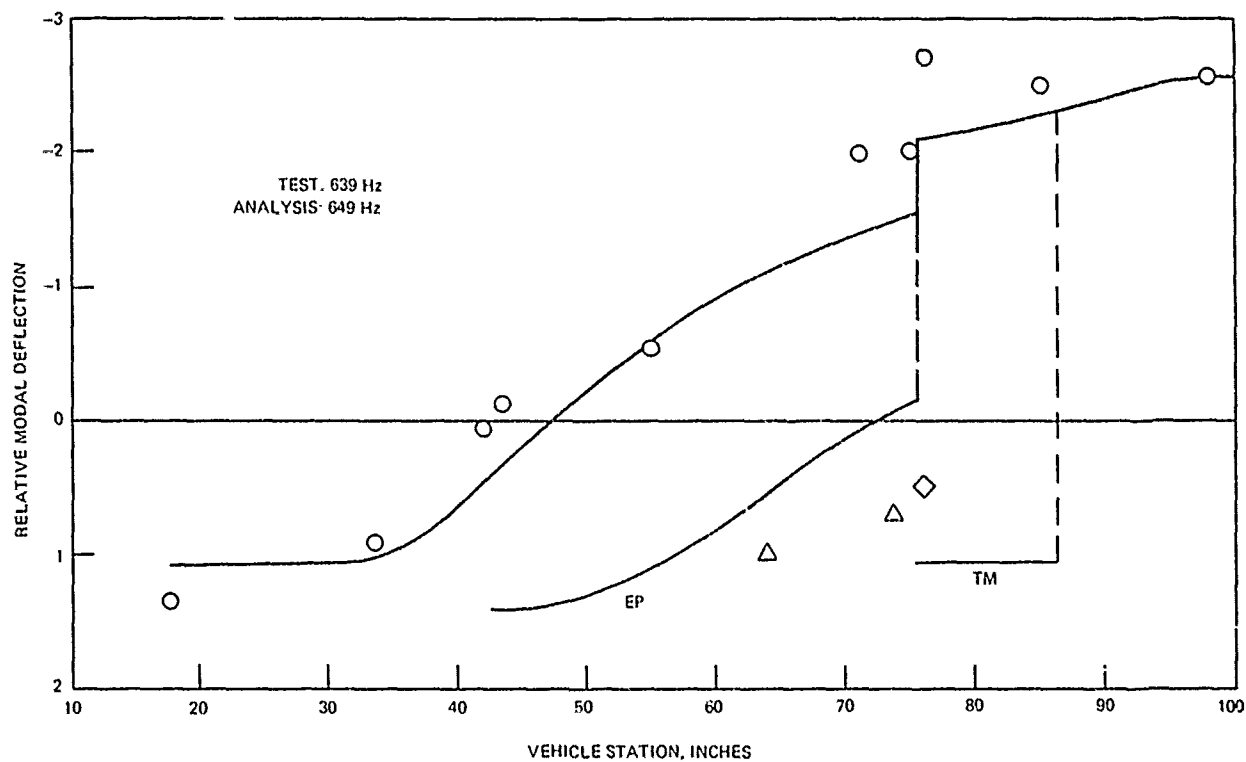


Figure 13. Axial Mode Shape

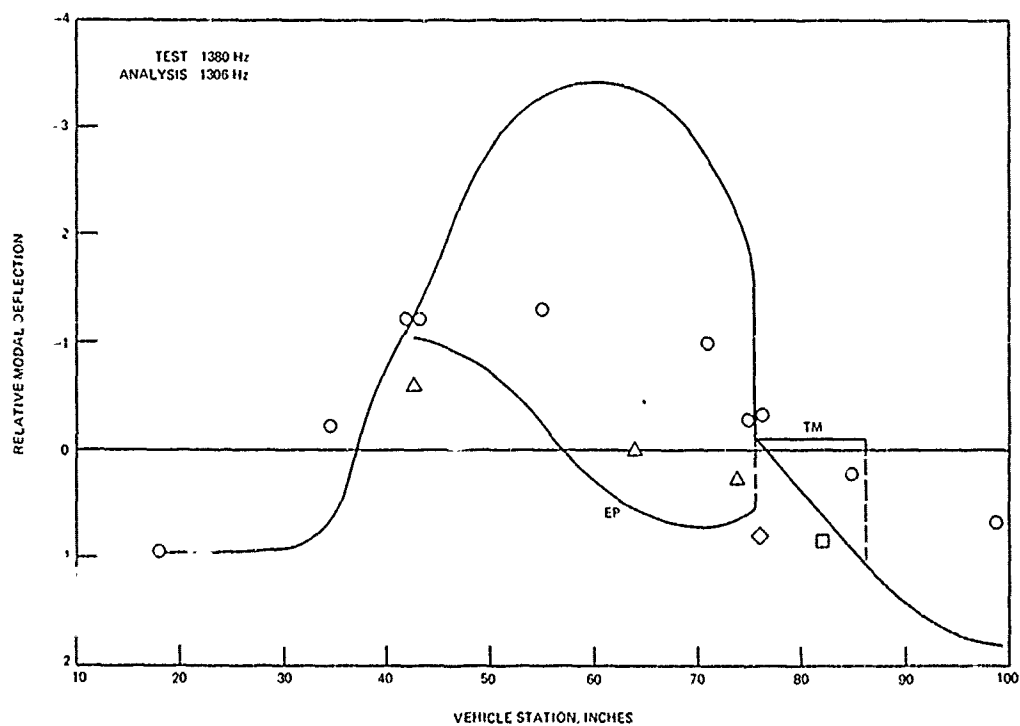


Figure 14. Axial Mode Shape

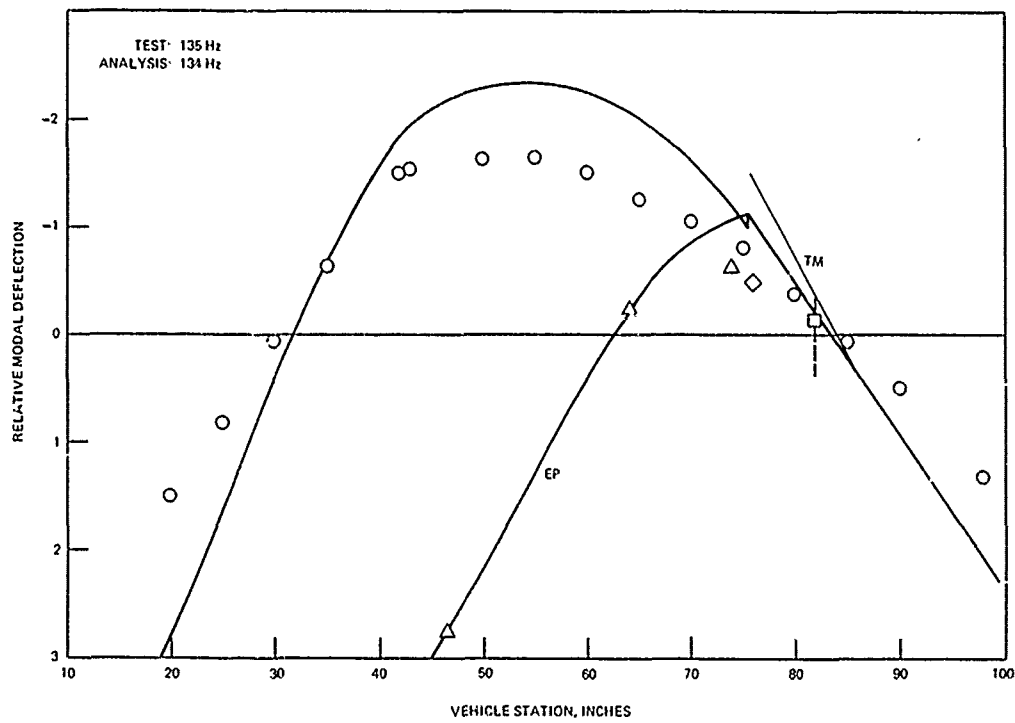


Figure 15. Lateral Mode Shape

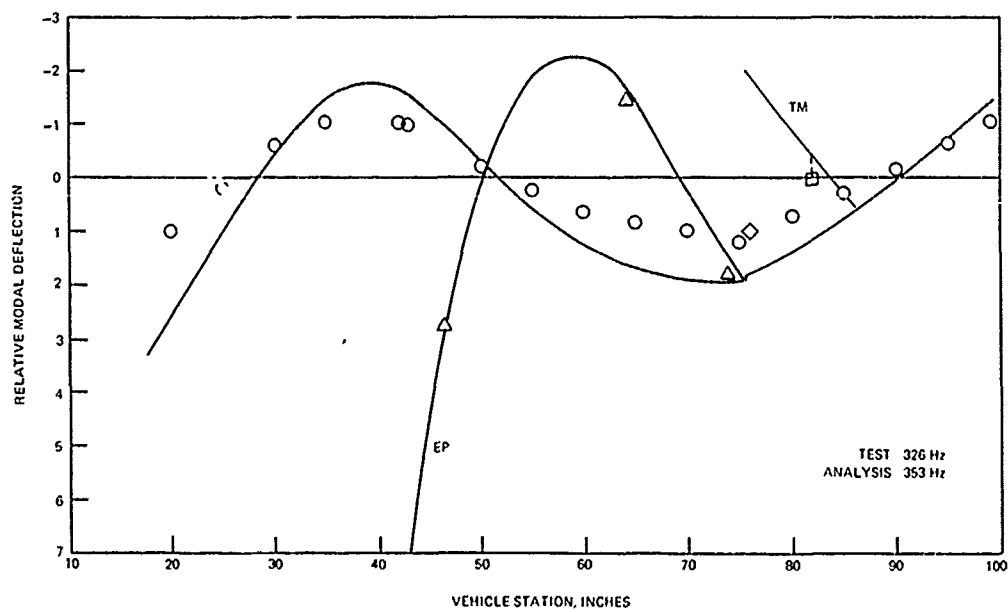


Figure 16. Lateral Mode Shape

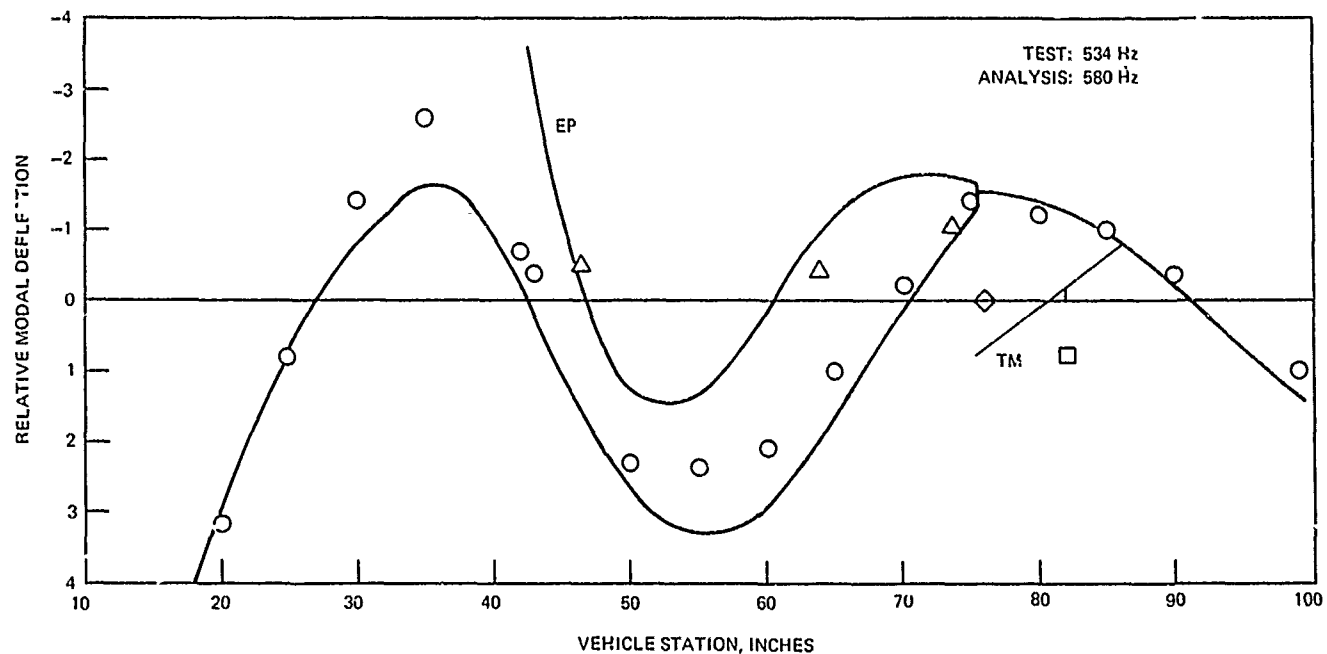


Figure 17. Lateral Mode Shape

In Table IV, it is seen that axial experimental frequencies 442 Hz and 478 Hz have no corresponding analytical frequencies, and that their mode shapes portray very little motion. It was not fully understood why the above frequencies were not predicted, since there was excellent frequency similitude in the other six modes. However, contribution from the 442 and 478 Hz modes will be negligible. This was verified in the acoustic test. That is, since there is very little motion in the modes, modal forces and modal displacements will be diminutive.

In Table V, there is no corresponding lateral experimental frequency for the 98 Hz analytical prediction. The analytical mode shape showed very little motion of the vehicle nose. Hence, the shaker located at the vehicle nose during modal survey testing would not produce large telemetry package (TM) motion. The only way to duplicate this mode experimentally would be to physically attach the shaker to the TM. Also, in Table V, the experimental frequency of 460 Hz does not have a corresponding analytical frequency.

The structural damping values shown in Tables IV and V are obtained from the in-phase or co response peaks just before and just after resonance. The co response is zero at resonance.

Structural damping, g' , is related to peak co response frequencies, ω_a and ω_b by

$$g' = \frac{\left(\frac{\omega_a}{\omega_b}\right)^2 - 1}{\left(\frac{\omega_a}{\omega_b}\right)^2 + 1}$$

Volume II of this report contains the in-phase response plots from which the structural damping coefficients in the tables were obtained.

SECTION VI

RE-ENTRY VIBRATION RESPONSE PREDICTIONS

1. COMBINED FOREBODY AND WAKE ENVIRONMENTS

The prototype vehicle dynamic model was subjected to the combined turbulent boundary layer and wake environments of Section III. The response formulation of Section IV utilizing the constant pressure cross PSD assumption was followed. Figures 18 through 30 show the resulting predicted acceleration power spectral densities for each internal accelerometer location. Shown on the figures in addition to the PSD's are the rms accelerations. The predicted strain PSD's were not plotted, because they were too small, less than 10^{-16} (in/in)²/Hz.

In order to discuss the predicted responses, it would first be helpful to present the transformations utilized in obtaining them. The dynamic model does not, in all instances, have coordinates which directly correspond to accelerometer locations. For this reason, geometric transformations have been used to predict the response at the exact accelerometer locations. Table VI presents the transformations used, where the q_i coordinates represent degrees of freedom in the dynamic models.

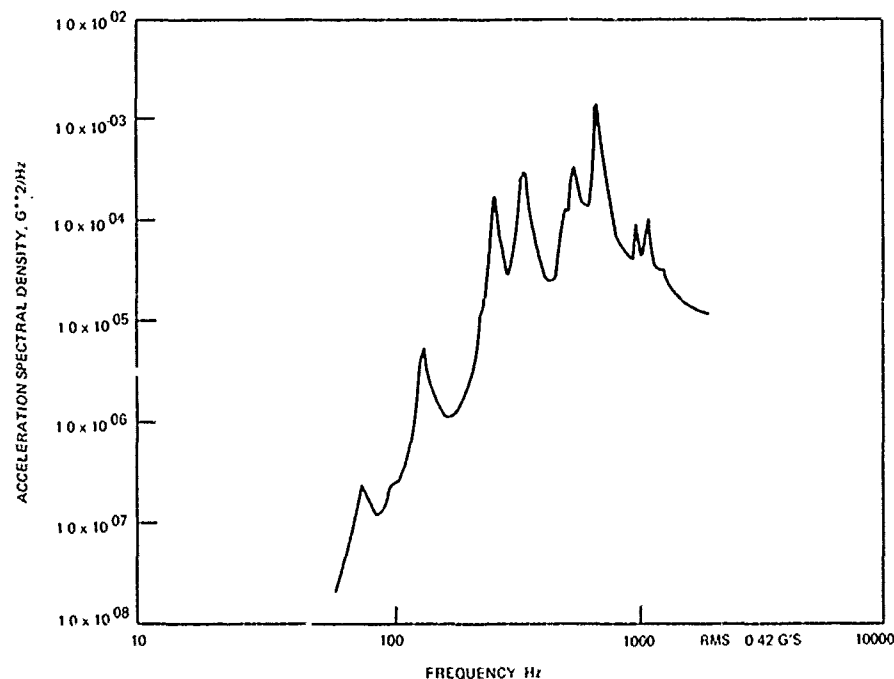


Figure 18. Accelerometer 1AL Response

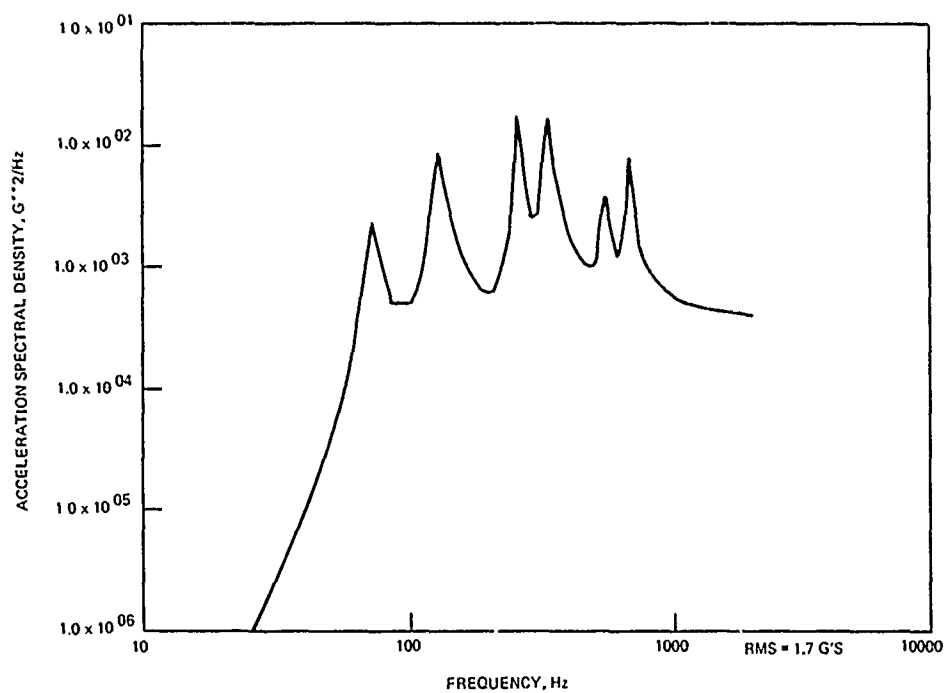


Figure 19. Accelerometer 1AT Response

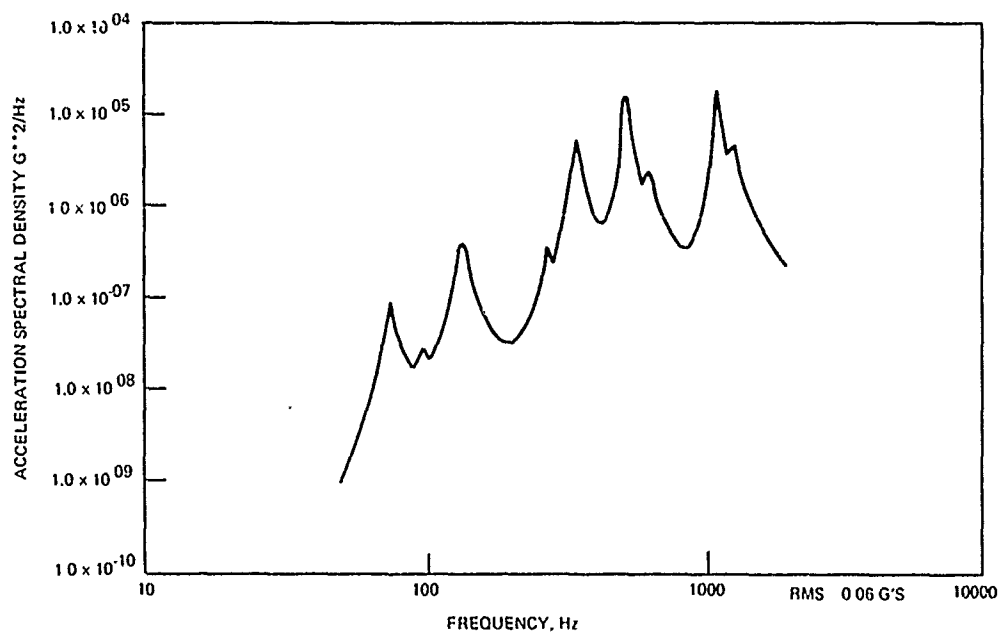


Figure 20. Accelerometer 3AL Response

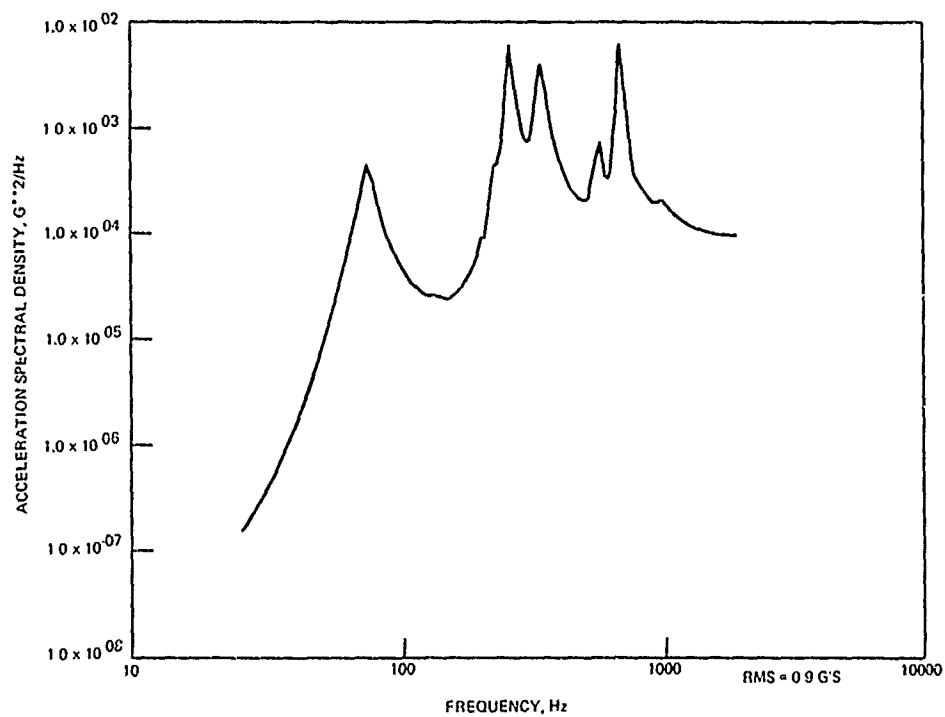


Figure 21. Accelerometer 3AT Response

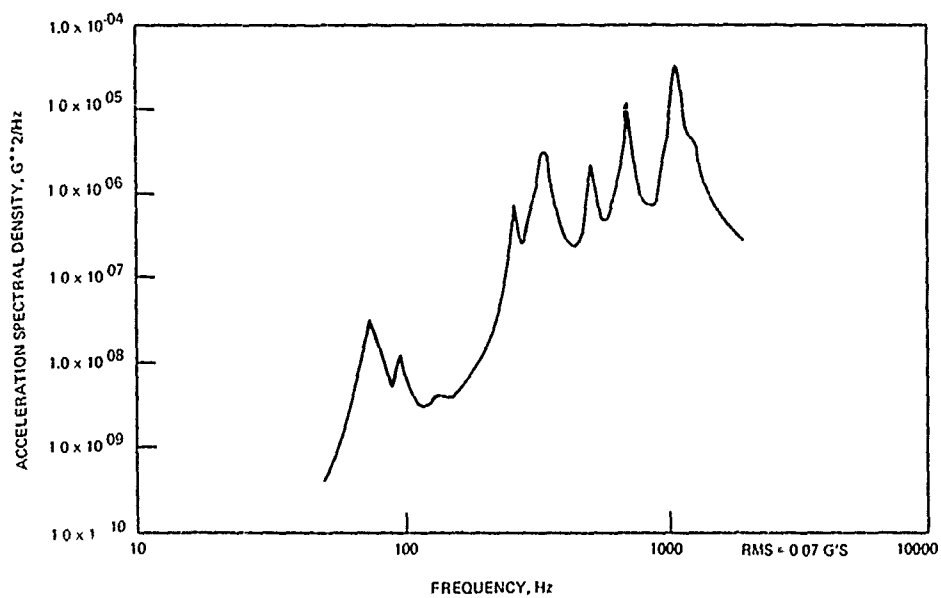


Figure 22. Accelerometer 4AL Response

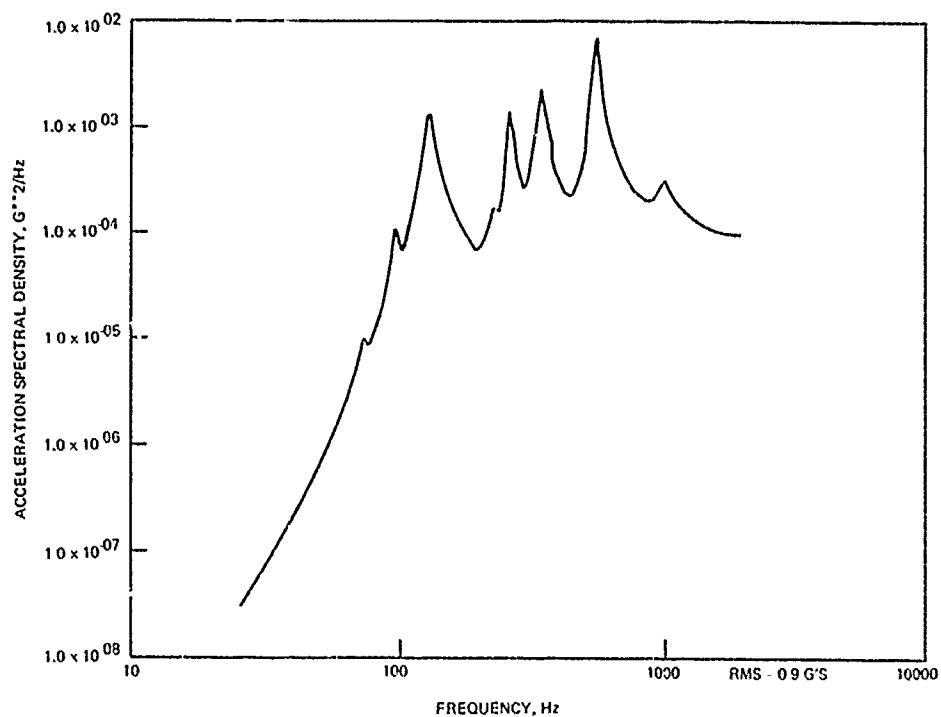


Figure 23. Accelerometer 4AT Response

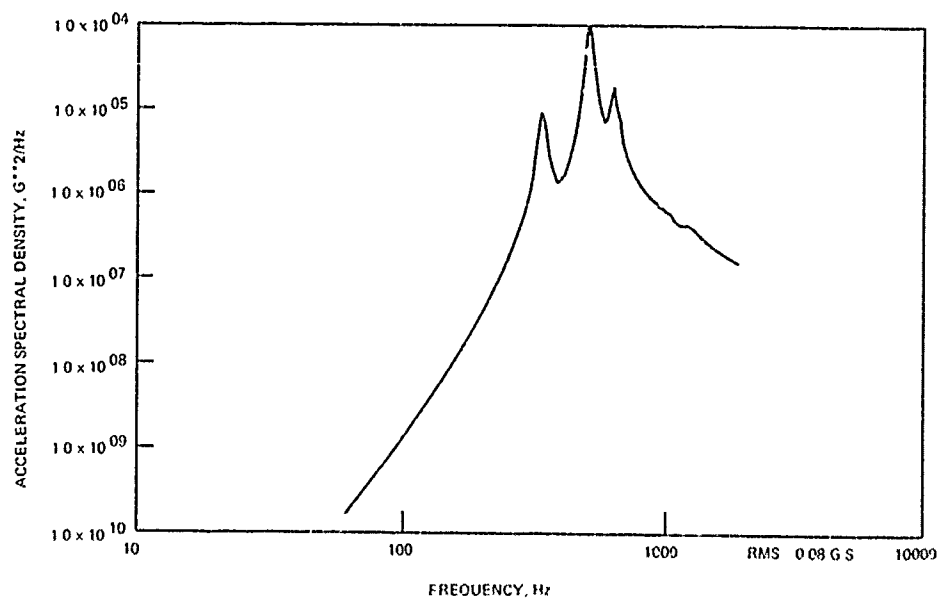


Figure 24. Accelerometer 5AL Response

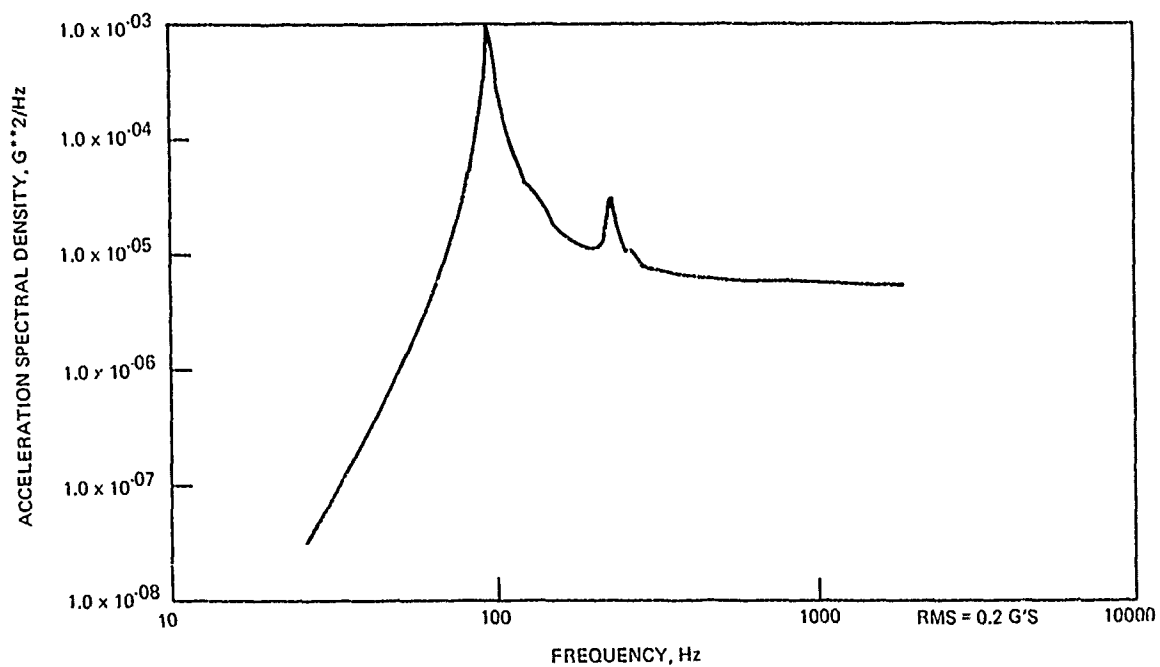


Figure 25. Accelerometer 5AT Response

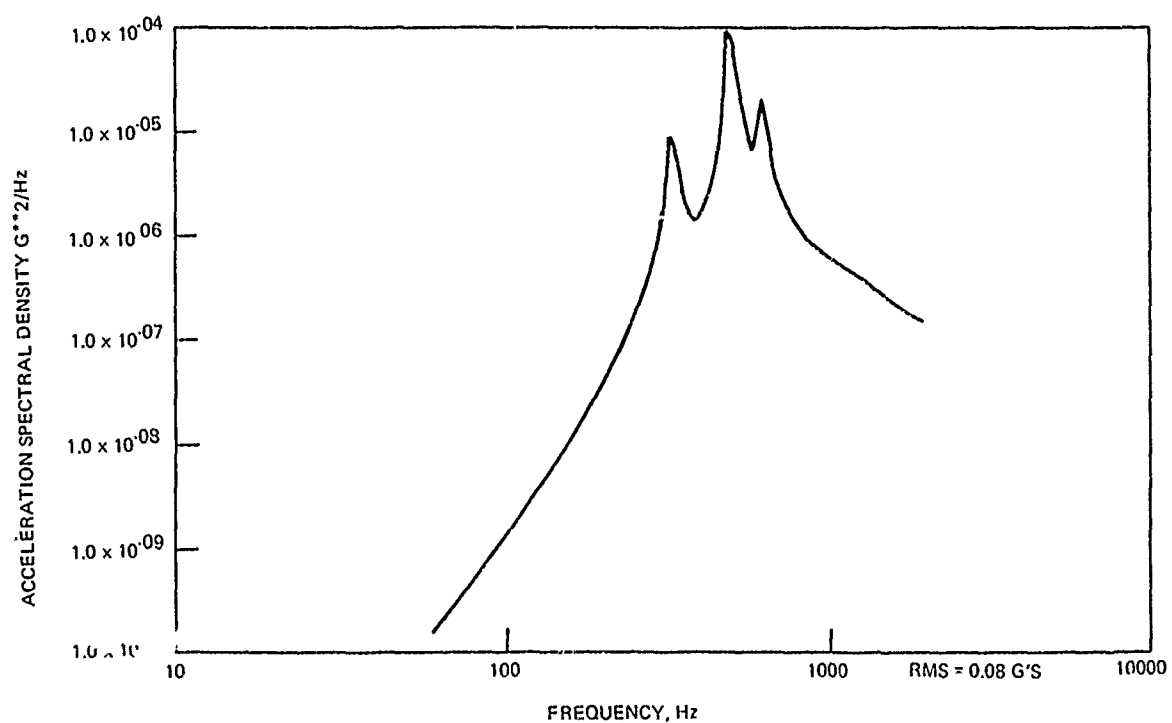


Figure 26. Accelerometer 6AL Response

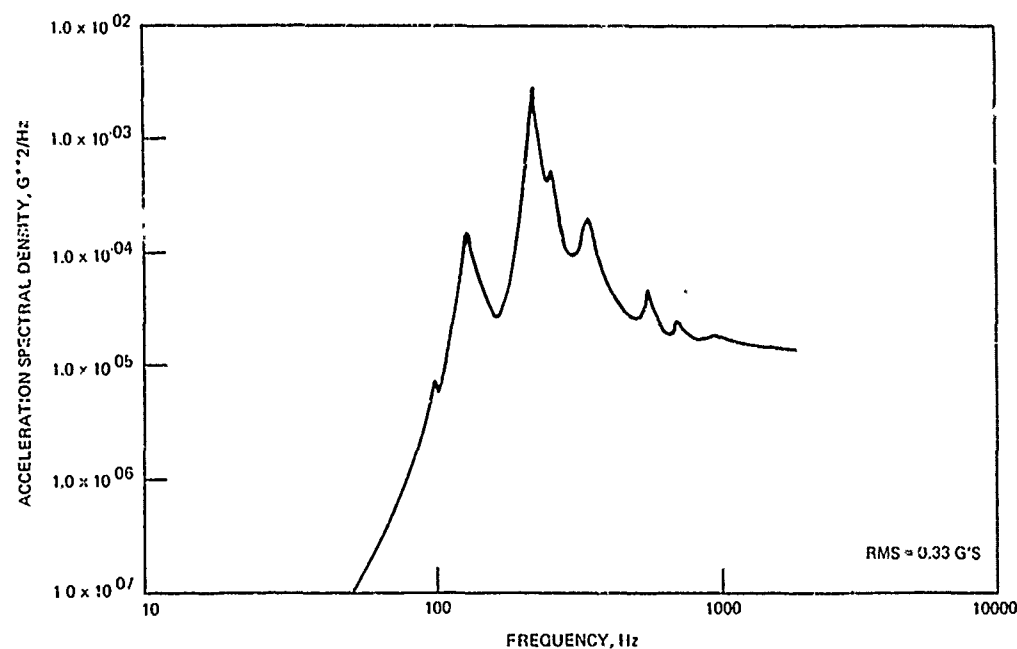


Figure 27. Accelerometer 6AT Response

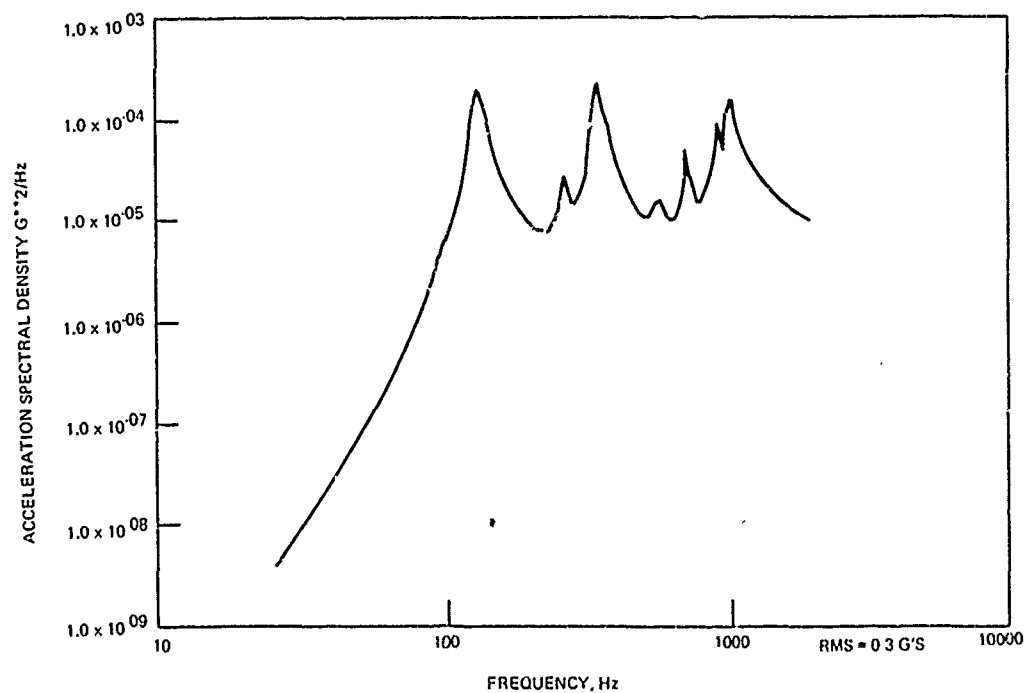


Figure 28. Accelerometer 8AN Response

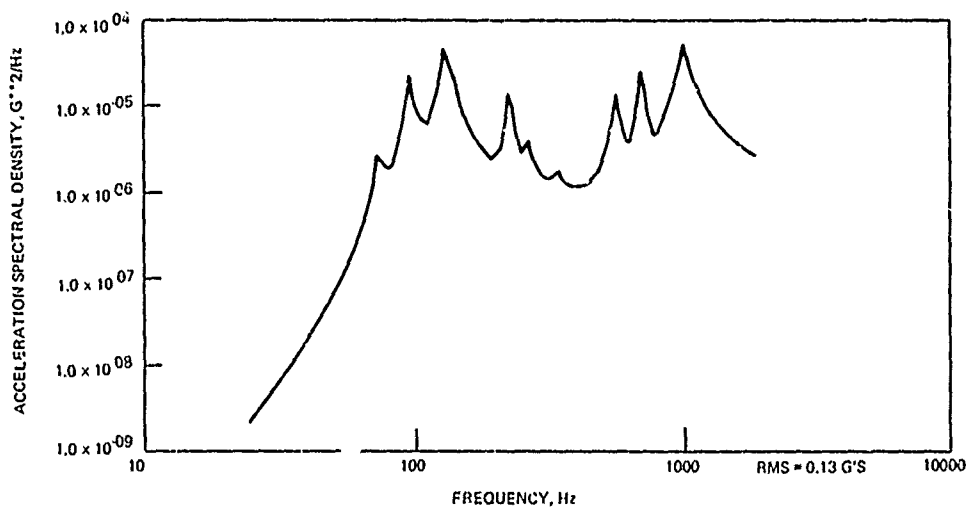


Figure 29. Accelerometer 9AN Response

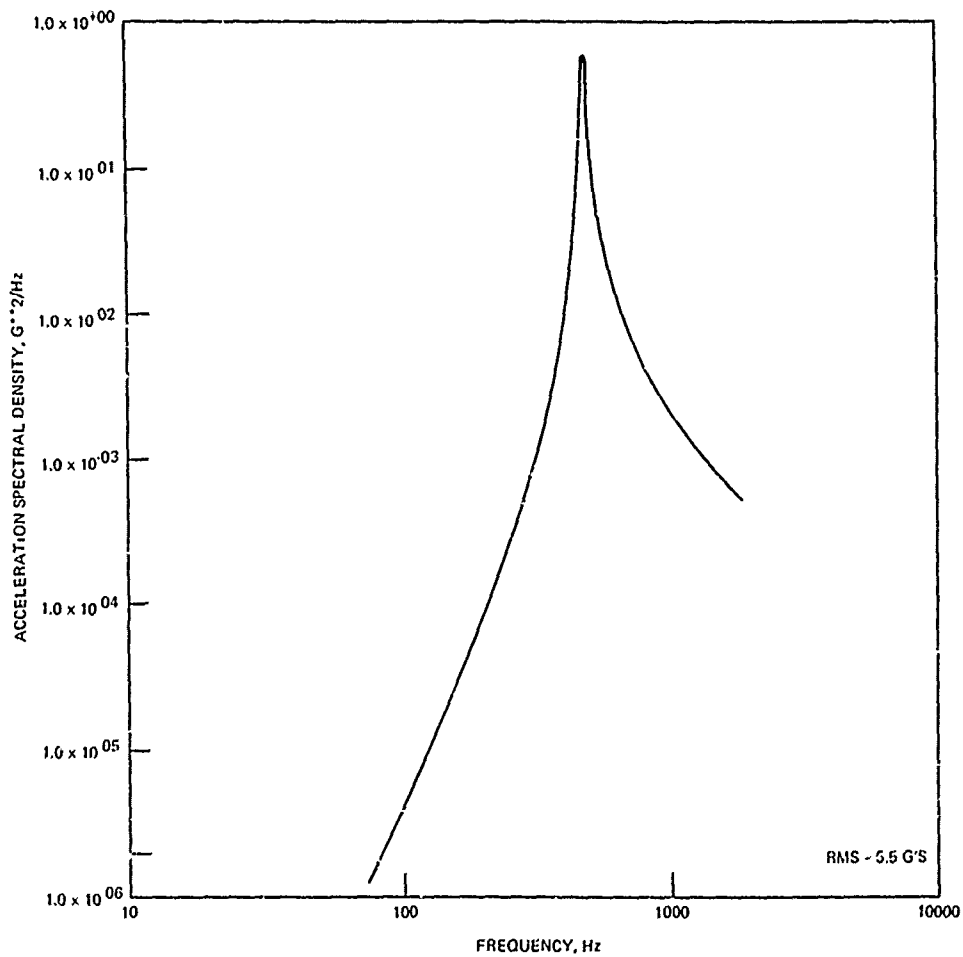


Figure 30. Accelerometer 10AL Response

TABLE VI. TRANSFORMATIONS FOR ACCELEROMETER
RESPONSE PREDICTIONS

Accelerometer	Axial Model Coordinates	Lateral Model Coordinates
1AL	q_{79}	$2.0 q_{112}$
1AT	-	$0.47 q_{111} + 0.53 q_{113}$
3AL	q_{83}	$0.625 q_{120}$
3AT	-	$0.38 q_{117} + 0.62 q_{119}$
4AL	q_{85}	$0.625 q_{124}$
4AT	..	$0.49 q_{121} + 0.51 q_{123}$
5AL	q_{86}	-
5AT	-	q_{127}
6AL	q_{86}	$3.0 q_{126}$
6AT	-	$q_{125} - 6.128 q_{126}$
8AN	q_{35}	q_{53}
9AN	q_{56}	q_{81}
10AL	q_{76}	q_{107}

Table VI shows, for example, that accelerometer 1AL represents the sum of the accelerations at coordinate 79 in the axial model and a 2 inch radius times the rotation of coordinate 112 in the lateral model. Accelerometer 1AT receives no contributions from the axial model but is physically located between coordinates 111 and 113, so that the transformation represents an averaging of the accelerations at these coordinates. The rest of the accelerometer locations are similarly obtained. It is observed that accelerometers 5AL, and 6AL are functions of axial model accelerations only and 1AT, 3AT, 4AT, 5AT and 6AT are functions of the lateral model accelerations only. These results are reflected in the response predictions shown in Figures 19 through 30, where it is seen that PSD peaks of Figures 24 and 26 are due to only axial model natural frequencies, whereas Figures 19, 21, 23, 25, and 27 reflect lateral model frequencies at the peaks of the PSD's. Figures 18, 20, 21, 28, and 29 contain peaks associated with both axial and lateral natural frequencies, since these locations are coupled in the axial and lateral directions. Figure 30, which represents the accelerometer located on the aft cover, only exhibits one dominant frequency, which is the

aft cover frequency. This is expected, since the aft cover mode at 524 Hz in the axial mode! responds so significantly that it masks the contributions of other modes at their natural frequencies. If there were no aft cover loading, Figure 30 would exhibit peaks at other modes in addition to the one at 524 Hz.

2. SEPARATE FOREBODY, WAKE ENVIRONMENTS

The responses shown in the figures are for a simultaneous application of the re-entry environments in Section III; that is, the turbulent boundary layer environment was applied at the same time as the wake environment. The effects of each environment independently applied will now be discussed.

Basically little difference would be expected in the results for Figures 18 through 29 if only the forebody environment were applied. The aft cover environment, as shown in Section III, is significantly lower than the forebody environment. The force cross PSD matrix for the combined environments would have smaller terms for the part of the matrix associated with the aft cover coordinates versus the terms associated with the forebody. Also, except for analytical modes identified as aft cover modes, little aft cover motion exists in the other predicted modes. Thus when the modal force is obtained through the pre- and post-multiplication of the force cross PSD matrix by the individual mode shapes, there would be little contribution from the wake environment. The responses predicted for the combined environments are therefore essentially the same as would be expected for the attached turbulent flow alone for the internal component accelerometers.

This is obviously not the case for the aft cover accelerometer. Under the turbulent boundary layer environment alone, the response predictions for the aft cover would not show the dominance of the aft cover mode. The response levels would be greatly reduced over that shown in Figure 30, and the PSD would be characterized by peaks at each natural frequency whose mode shape has even slight aft cover motion.

Under the reverse situation, where the environment is only applied to the base of the re-entry vehicle, the opposite trends would result. Figure 30 would be unchanged, but Figures 18 through 29 would be reduced by orders of magnitude and reflect modes which contain a slight amount of aft cover motion.

SECTION VII

RESPONSE VERIFICATION TEST

1. OBJECTIVES

The response verification test was an acoustic test utilizing the AFFDL Sonic Fatigue Facility.

The objectives were to:

- (1) Verify the optimized response prediction technique by obtaining vehicle response data plus internal vibration response in a form suitable for correlation with analyses; and to
- (2) Define vehicle simulation techniques by making accurate measurements of external and internal acoustic levels and spectra in order to define and express in sufficient detail the experimental forcing function.

2. TEST REQUIREMENTS

a. Acoustic Test - AFFDL Sonic Fatigue Facility

The vehicle was subjected to two separate test environments of reverberant and progressive wave sound fields in the Large Test Chamber at the AFFDL Sonic Fatigue Facility. The support system consisted of three lengths of bungee cord and three turn-buckles. One bungee cord was attached to the nose tip and the two remaining to the aft end. Figure 31 shows the support system. The vehicle was positioned in the chamber with its nose approximately 10 feet from the siren bank. Its roll axis was coincident with the geometric center of the sirens.

In addition to the internally installed instrumentation to monitor vehicle response, arrays of microphones were utilized at the external vehicle surface to obtain the acoustic environment description. Figure 32 shows the external instrumentation. Based on sound pressure data from the test facility and response predictions for the acoustic environments, a minimum sound pressure level spectrum was defined for the verification test. This is shown in Figure 33. It was also shown in the pretest predictions that if the same sound pressure levels were applied to the base of the re-entry vehicle as the forebody, the aft cover response would be in excess of the re-entry vibration predictions for wake. A baffle was therefore constructed to reduce the incident sound pressure levels on the aft cover in the acoustic test by 15 to 18 dB over that on the forebody.

b. Chamber Environments - Reverberant, Progressive Wave

In order to achieve a diffuse sound field, the AFFDL Large Test Chamber curtains were raised and the floor uncovered. In the progressive test the curtains were down and the floor was covered. The same sound pressure spectra were required for each test; they are given in Figure 33.

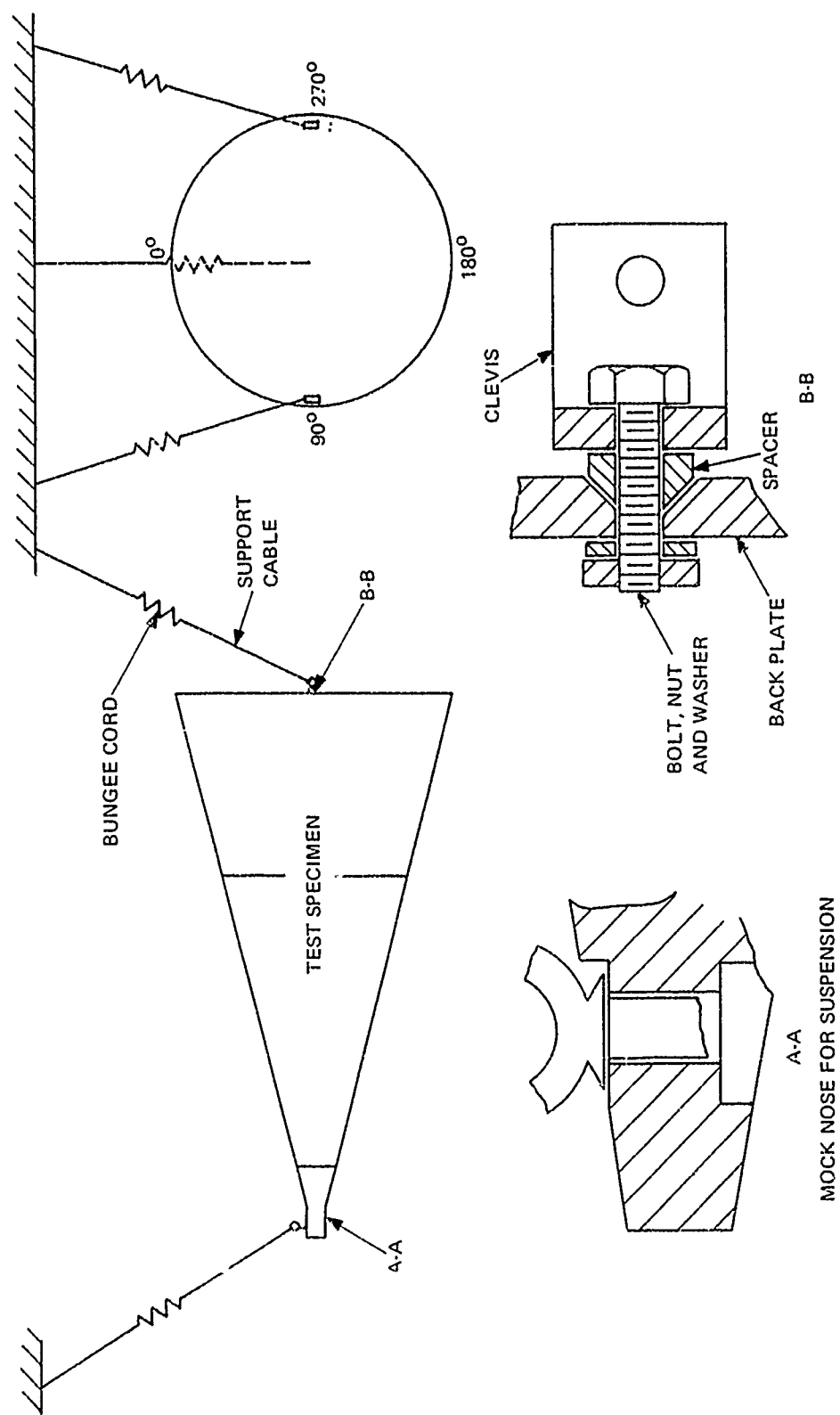
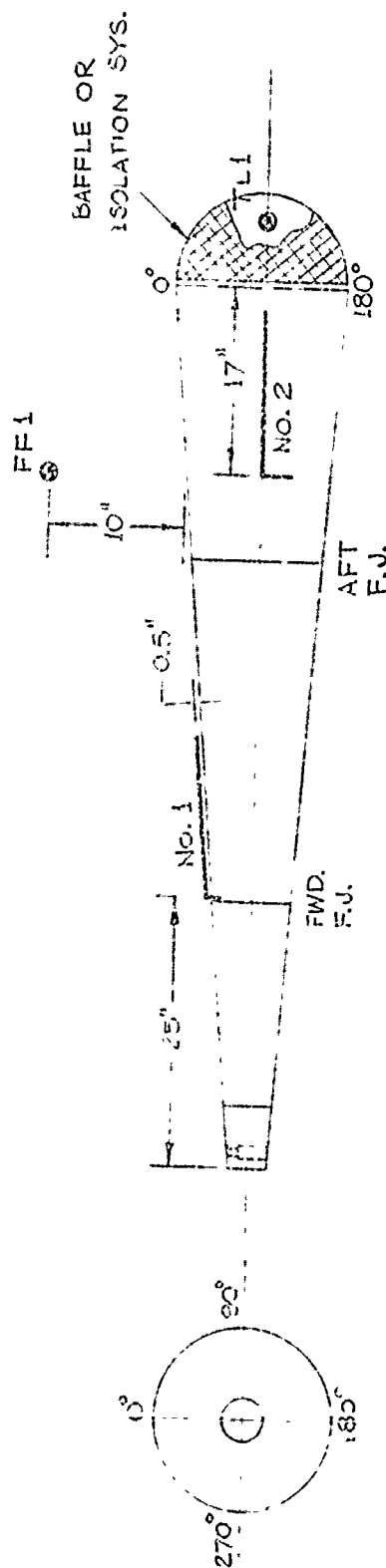
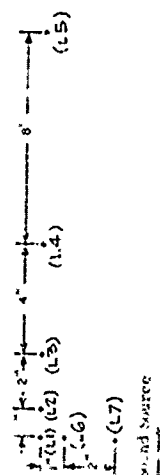


Figure 31. Vehicle Support System

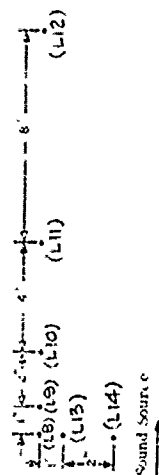


L-SHAPED PATCH ARRAYS

No. 1



No. 2



Note: (1) Shaped arrays are located 0.5 inches from the vehicle, microphones normal to surface.
 (2) L1 and L8 are pivot sensors
 (3) F.J. - Field Joint

Figure 32. Schematic of External Acoustic Sensors

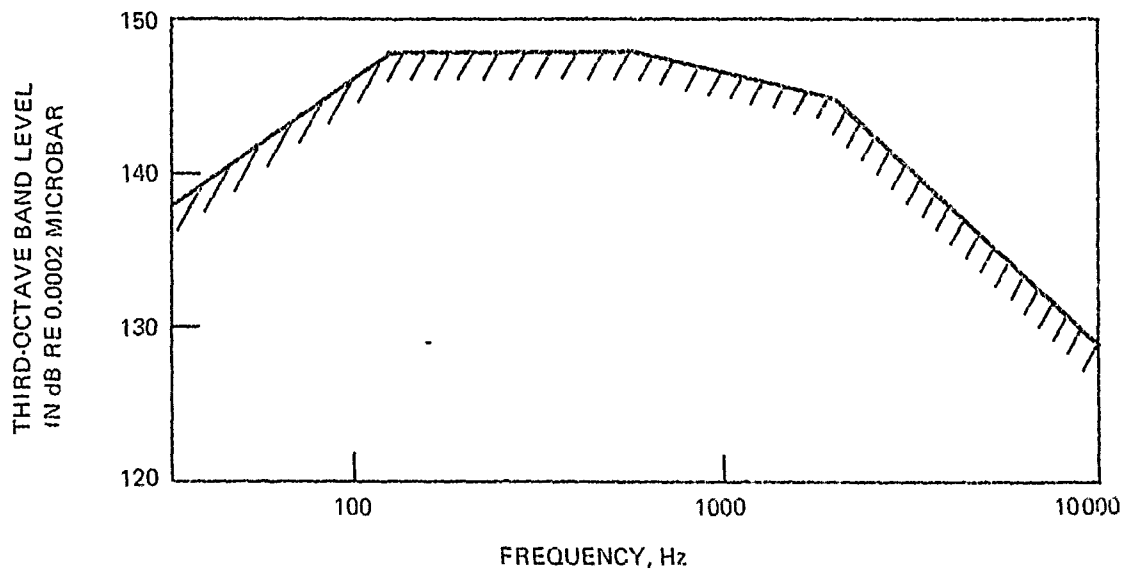


Figure 33. Acoustic Spectrum -- Minimum Level

The data processing requirements for each test environment were as follows: All raw acoustic analog data were analyzed to obtain Sound Pressure Level (SPL) on a 1/3-octave band basis for post test quick-look evaluation. Power spectral density (PSD) analyses were later performed on all acoustic sensor data. Figure 34 shows quick-look acoustic data processing requirements. In addition, detailed data processing of the acoustic sensors comprising the L-shaped patch arrays were performed. The intent was to determine spatial correlation functions and cross-PSDs in order to express the experimental forcing function in a form suitable for use with the FATE III A dynamic model. This was the primary reason for recording the L-shaped array microphones on specific tape recorder channels. Figure 35 shows detailed acoustic data processing requirements.

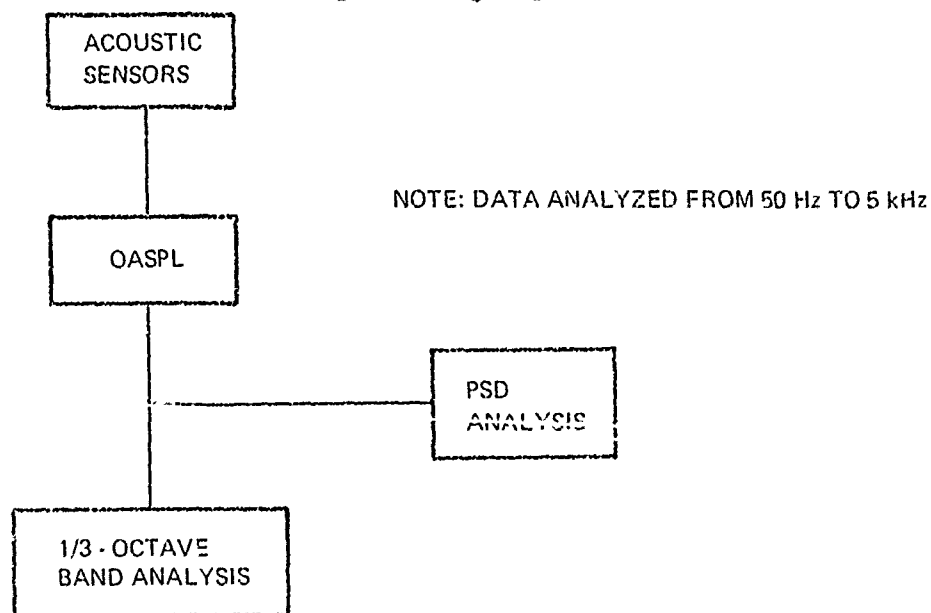
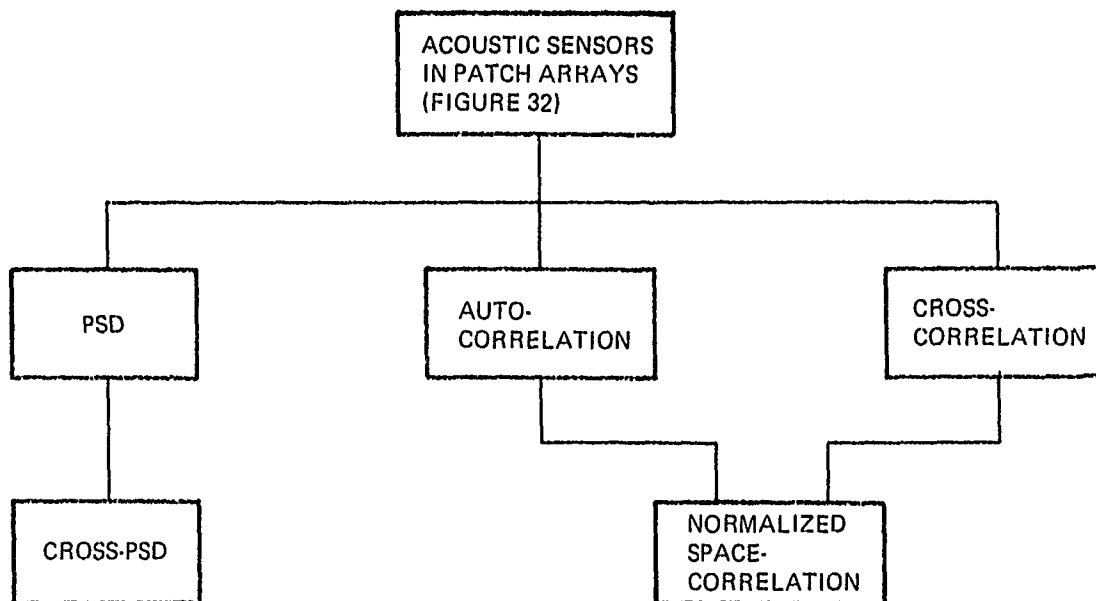


Figure 34. Quick-Look Acoustic Data Processing



NOTE: NARROW BAND SPATIAL CORRELATION COEFFICIENTS ARE TO BE OBTAINED AT THE FOLLOWING FREQUENCIES:

125, 500, 1000 AND 2000 Hz

Figure 35. Detailed Acoustic Data Processing

Since acoustic sensors L1 and L8 were the pivot sensors in the L-shaped patch arrays, the following combinations were analyzed:

NO. 1 PATCH ARRAY

Meridional

L1 - L2
L1 - L3
L1 - L4
L1 - L5

Circumferential

L1 - L6
L1 - L7

NO. 2 PATCH ARRAY

Meridional

L8 - L9
L8 - L10
L8 - L11
L8 - L12

Circumferential

L8 - L13
L8 - L14

c. Vibration Response

The prototype vehicle response to the acoustic environments was monitored via the internally mounted accelerometers and strain gages. The acceleration and strain data, after initial RMS determination, were analyzed for frequency content by obtaining power spectral densities. Figure 36 shows the data processing requirements for the acceleration and strain data.

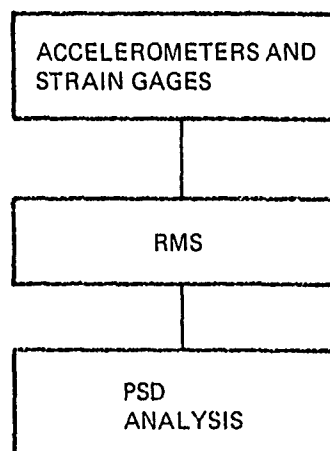
3. TEST RESULTS

a. Acoustic Environment

Upon completion of the data evaluation from the two acoustic tests, it became clear that there was little difference in the environment between the two tests. The specimen was mounted too close to the siren bank to achieve a truly diffuse sound field. The two test environments can be best described as modified progressive. The detailed acoustic data evaluation is given in Section VIII. Volume II of this report contains the entire data obtained during the acoustic testing.

Figures 37 and 38 represent typical one-third octave band sound pressure level spectra obtained during each test from a forebody microphone. Figures 39 and 40 represent sound pressure spectra obtained on the aft cover during each test. It is seen that the baffle performed as designed.

Attention will now be turned to the internal acoustic environments. The purpose of microphones 2PL and 7PL, mounted in the component packages, was to ascertain the amount of the acoustic environment that passes through the shell structure. This environment could



NOTES: (1) DATA ANALYZED FROM 20 Hz to 2 kHz
(2) FILTER REQUIREMENTS
20 TO 200 Hz WITH 5 Hz FILTER
200 Hz TO 2 kHz WITH 20 Hz FILTER

Figure 36. Vibration Data Processing

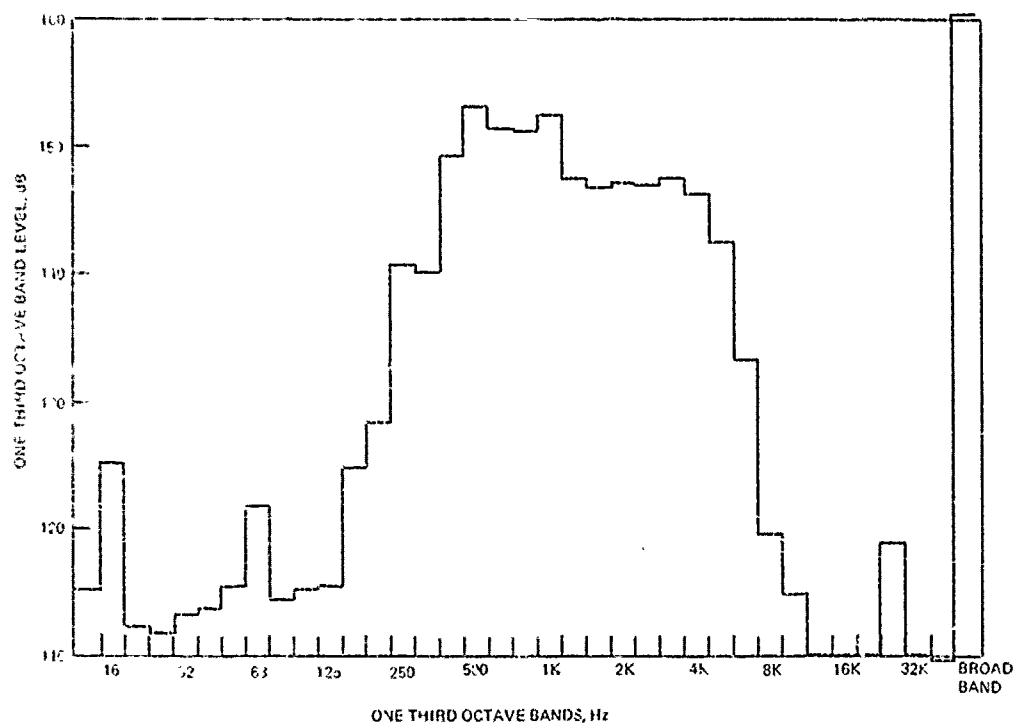


Figure 37. Forebody Sound Pressure Level In Progressive Test

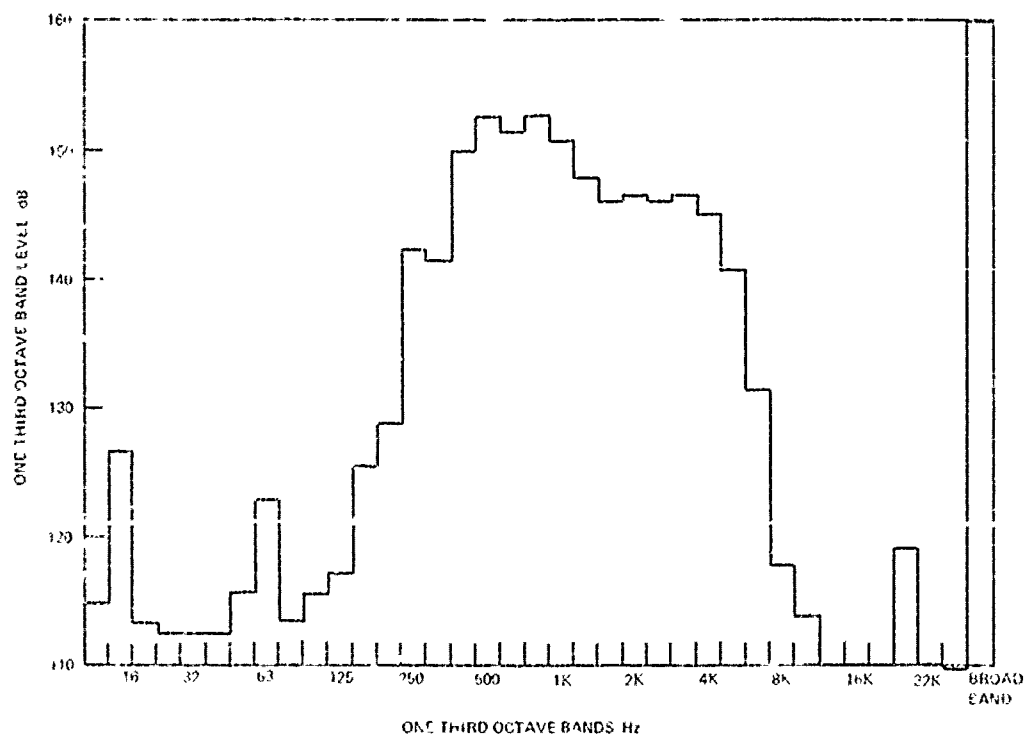


Figure 38. Forebody Sound Pressure Level In Reverberant Test

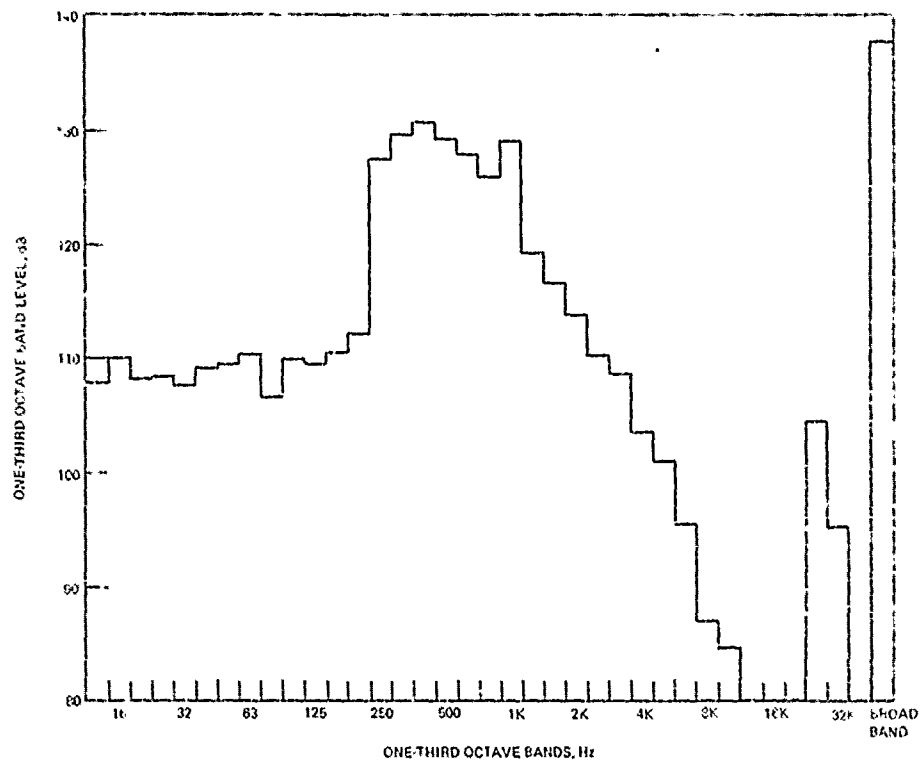


Figure 39. Base Sound Pressure Level In Progressive Test

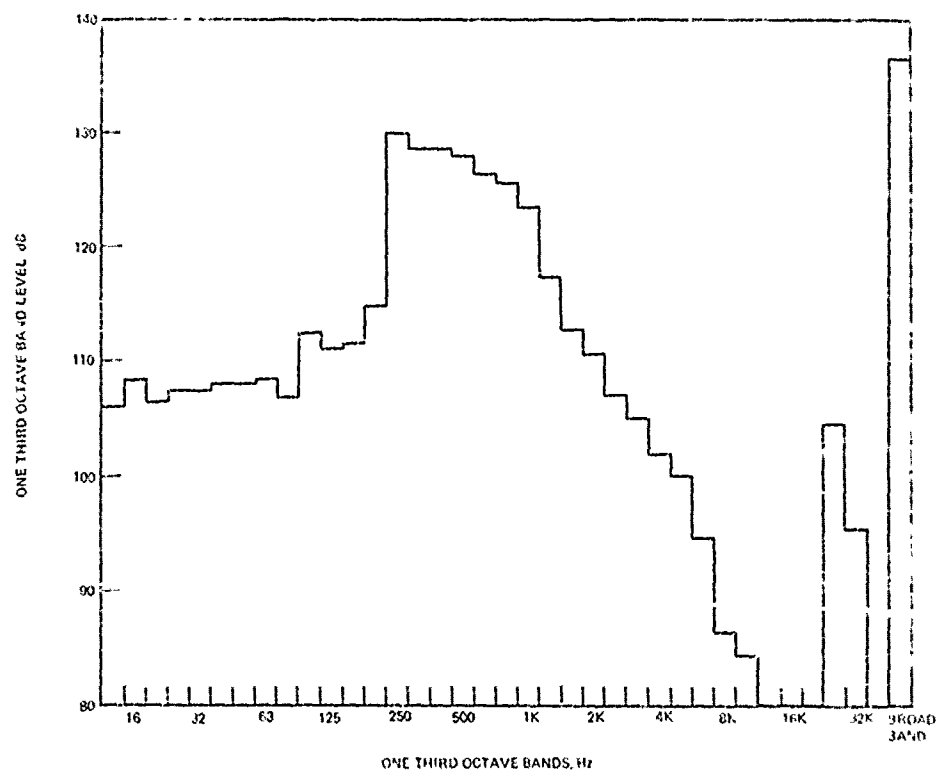


Figure 40. Base Sound Pressure Level In Reverberant Test

be of high enough magnitude to directly excite the component packages. Figures 41 and 42 show the one-third octave band sound pressure levels for the two internal microphones during the progressive acoustic test. It is seen that there is significant reduction in the levels over the external environment of Figures 37 and 38. The Overall Sound Pressure Level is reduced by 36 dB, with a corresponding 29 to 32 dB reduction in the one-third octave bands.

b. Vibration Response

As would be expected when the environments are essentially the same, the vehicle response was nearly identical for both tests. Acceleration power spectral densities were obtained for each accelerometer location. The figures in Section VIII contain these PSDs. As anticipated, the strain gage response was negligible, so no attempt was made to utilize this data.

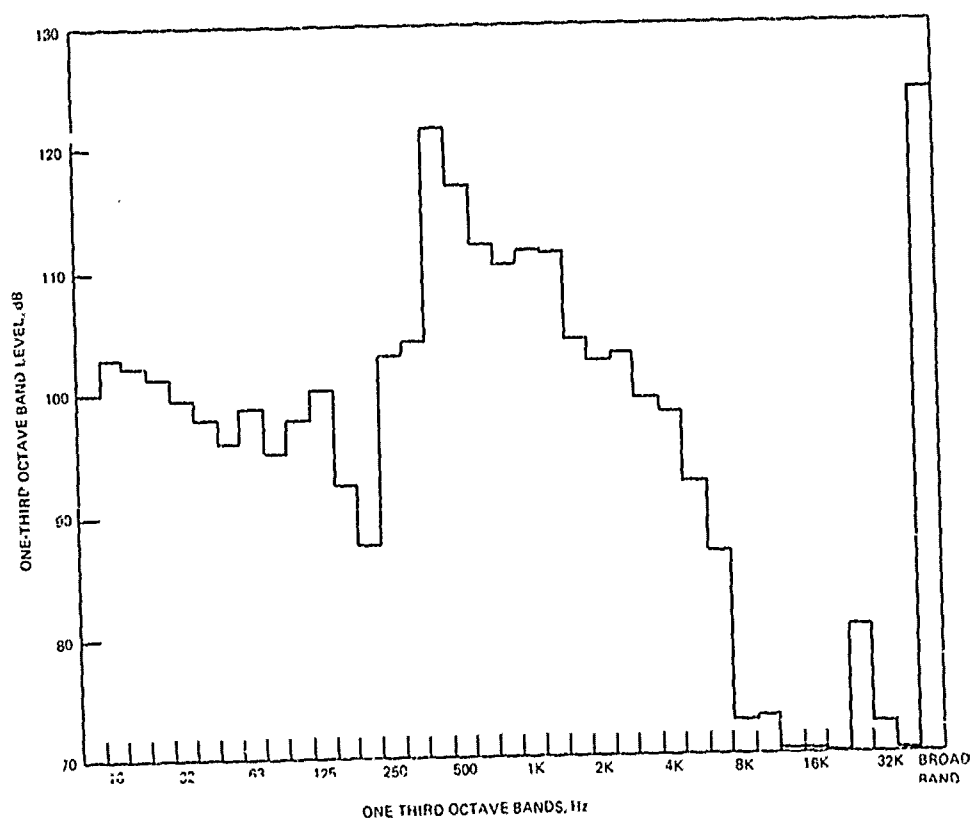


Figure 41. Internal Sound Pressure Level (2PL) In Progressive Test

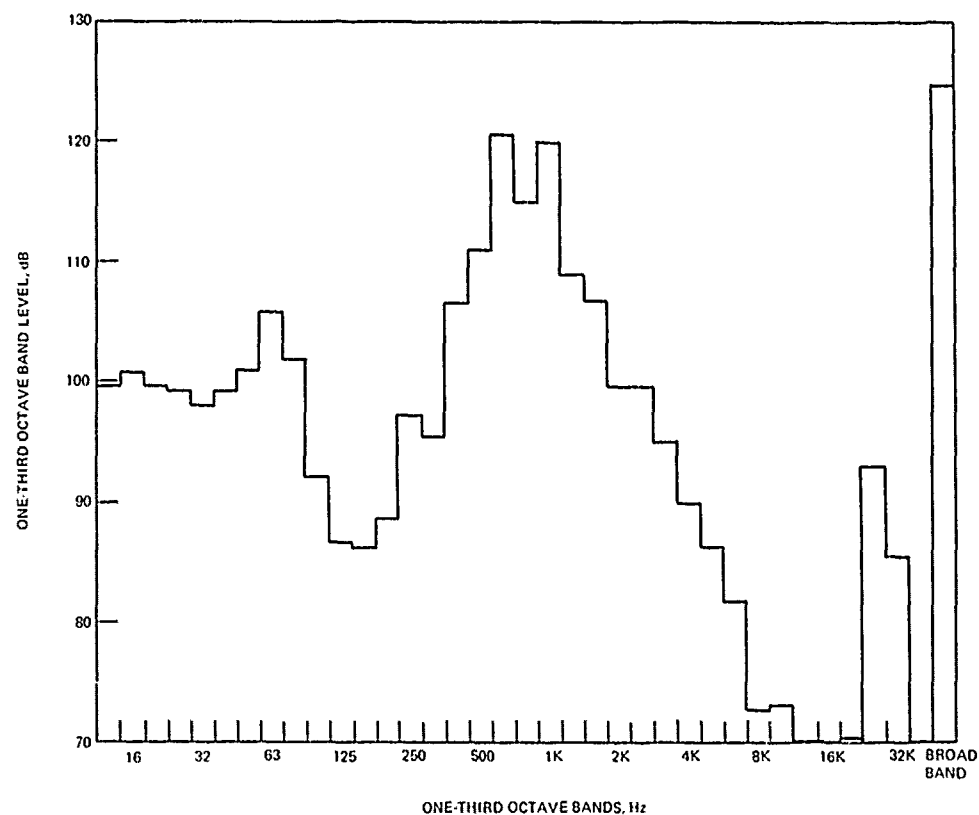


Figure 42. Internal Sound Pressure Level (7PL) In Progressive Test

SECTION VIII

PREDICTION TECHNIQUE VERIFICATION

1. TEST ACOUSTIC ENVIRONMENT DESCRIPTION

The acoustic test environment has been defined in a form suitable for response predictions. The two bits of data required to make response predictions are the pressure power spectral densities and the narrow band spatial correlation functions. The pressure PSDs are of course available directly from the processed data. Figure 43 shows a typical pressure PSD obtained using a narrow band filter for both the progressive and reverberant acoustic tests. It is observed that neither PSD represents a smooth curve. Each of the peaks and valleys must be accounted for in order to obtain accurate correlations. It is also seen that little difference exists between the progressive and reverberant tests.

Attention will now be turned to the derivation of the narrow band space correlation functions. The narrow band space-time correlation data was used for this purpose. Under ideal progressive wave conditions the narrow band space-time correlation functions should be of the following form in the meridional direction:

$$\mathcal{R}(\xi, \omega, \tau) = \frac{\sin[2\pi f_f (\tau - \xi/\vec{c})]}{2\pi f_f (\tau - \xi/\vec{c})} \cos 2\pi f_c (\tau - \xi/\vec{c}) \quad (39)$$

where

f_f = Filter bandwidth used in the data processing

f_c = Center frequency

ξ = Separation distance between the two microphones

\vec{c} = Sonic velocity.

The above expression peaks at 1.0 when $\tau = \xi/\vec{c}$. Figure 44 shows the test space-time correlation functions at 1000 Hz for microphones L1 and L3, and for L1 and L5. Also shown are points representing the above expression. The filter bandwidth used in the evaluation was 1/3 octave. It is seen on Figure 44 that the test points very closely coincide with the theoretically perfect progressive points. The only difference is that the test data does not peak at 1.0 at values of $\tau = \xi/\vec{c}$, but is somewhat decayed. This suggests a narrow band space correlation function of the ideal progressive form, but with a damping term included. This damping term can be obtained from the values of the space-time correlation data at $\tau = \xi/\vec{c}$. A plot of the values of the space-time correlation data at $\tau = \xi/\vec{c}$ versus $\xi\omega/\vec{c}$

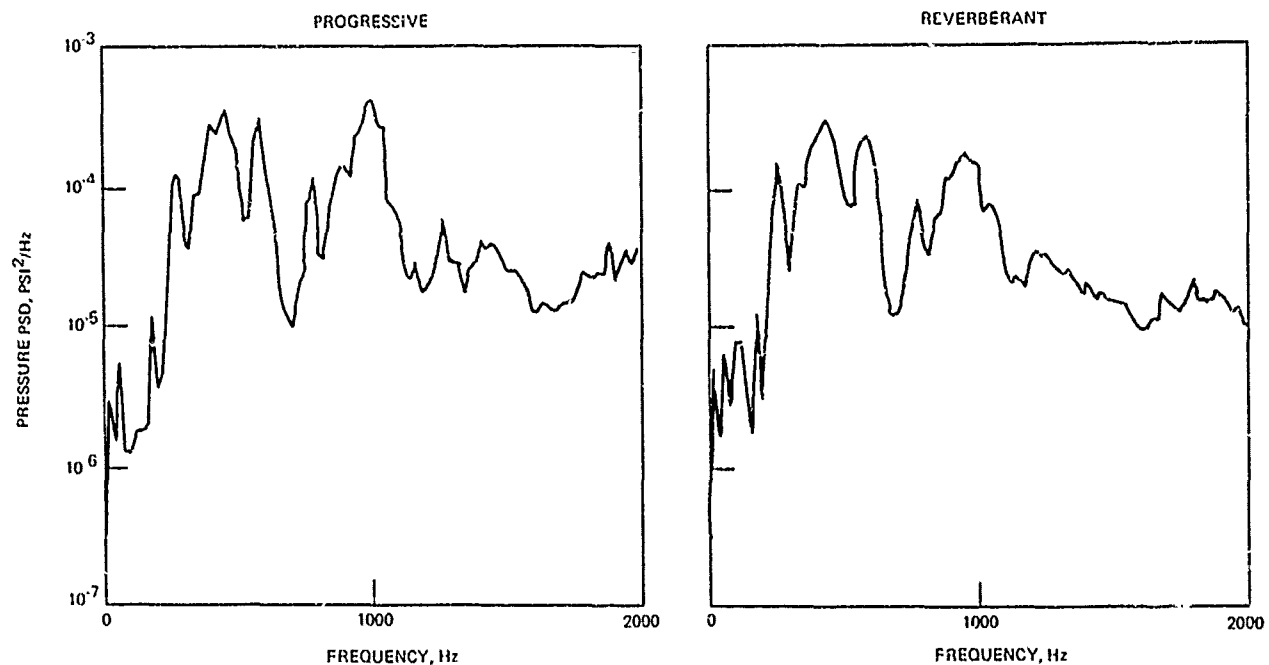


Figure 43. Narrow Band PSD'S of Microphone L1

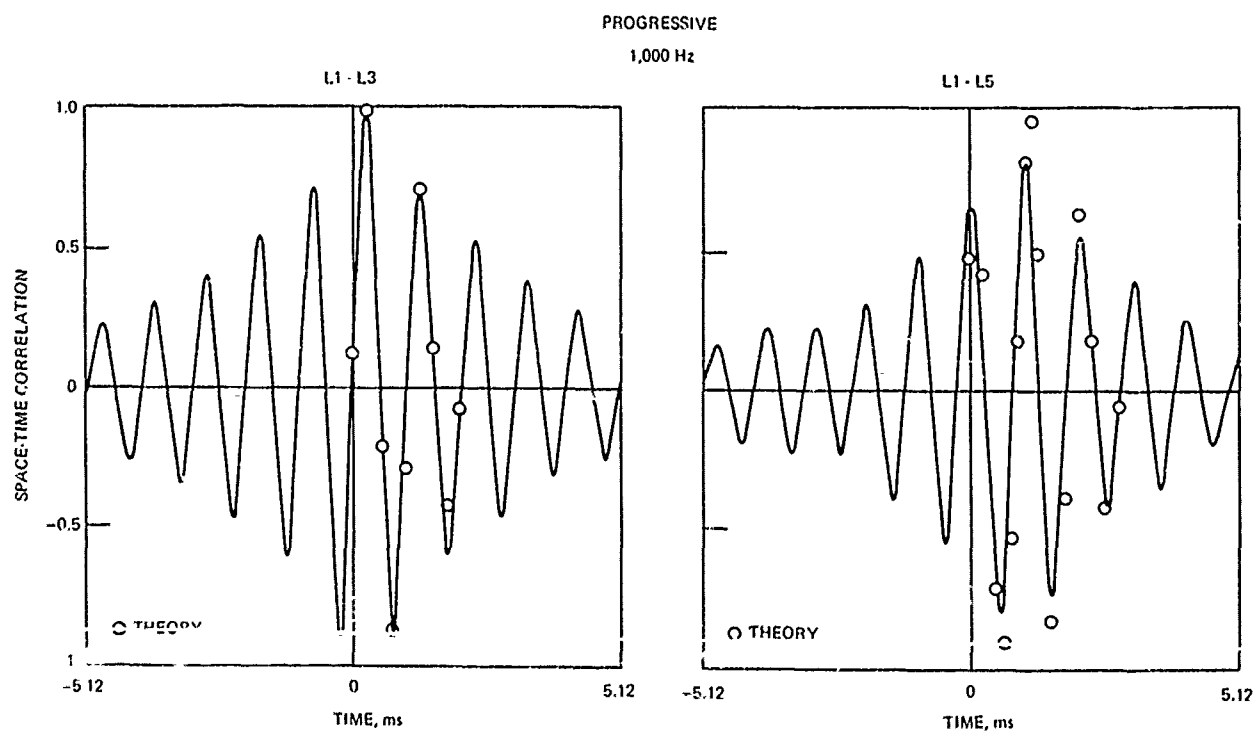


Figure 44. Meridional Space-Time Correlation Data

is constructed. A curve is then fit through these points. This yields a narrow band space correlation function of the following form in the meridional direction:

$$C(\xi, \omega) = e^{\frac{-0.0364|\xi|\omega}{c}} \cos \frac{\xi \omega}{c} \quad (40)$$

A check on the above expression is obtained from the space-time correlation data at $\tau = 0$. The narrow band space correlation function is the space time correlation at $\tau = 0$. Figure 45 shows the final meridional space correlation function with the test data at $\tau = 0$ superimposed. Also shown are the points used to arrive at the damping term. It is seen that nearly all of the test points fall on the analytical curve.

Under perfect progressive conditions the circumferential space-time correlation data should be of the following form:

$$R(\omega, \tau) = \frac{\sin [2\pi f_f \tau]}{2\pi f_f \tau} \cos 2\pi f_c \tau \quad (41)$$

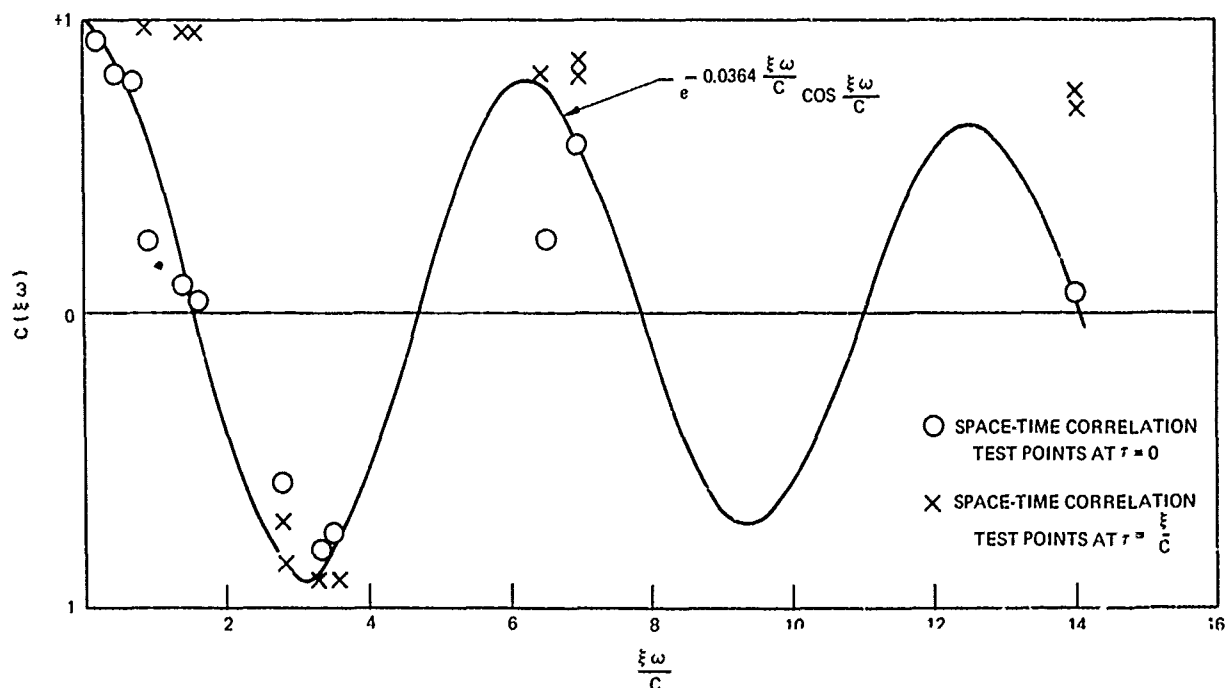


Figure 45. Meridional Spatial Correlation Function

Notice the absence of any dependence on the microphone separation distance. The above expression is simply the auto correlation function. It is seen that this expression also peaks at 1.0, but at $\tau = 0$. Figure 46 shows circumferential space-time correlation data at 1000 Hz. It is seen that the peak does indeed occur at $\tau = 0$ but it is not 1.0. This again suggests damped circumferential space correlation function. Figure 47 shows the decay envelope for the circumferential direction and the test points used to obtain it. The analytical expression is

$$C(\eta, \omega) = e^{-0.0705 \frac{\omega |\eta|}{c}} \quad (42)$$

The total narrow band spatial correlation function for the progressive acoustic test therefore is

$$C(\xi, \eta, \omega) = e^{-0.0364 \frac{\omega |\xi|}{c}} e^{-0.0705 \frac{\omega |\eta|}{c}} \cos \frac{\xi \omega}{c} \quad (43)$$

It is this expression which will be used in the correlation analysis.

The reverberant test data is very similar to the progressive data. As shown in Figure 43 the pressure PSD's are nearly the same. Figures 48 and 49 show a comparison between meridional and circumferential space-time correlation functions for the progressive and reverberant tests. The only significant difference between the two sets of test data is the larger amount of decay in the peaks that the reverberant test exhibits. This suggests that the reverberant test was in reality a more decayed progressive test. This result is expected, due to the close proximity of the re-entry vehicle to the siren bank. Another fact which verifies that the reverberant test is actually a progressive test is the peak of the circumferential space-time correlation data at $\tau = 0$. If the environment were reverberant, peaks at values of τ greater than zero would be expected. This is because in a reverberant environment the microphone separation distance influences the space-time correlation peaks in all directions, not just the meridional as in the progressive test.

The reverberant space-time correlation data was similarly analyzed as the progressive to yield a narrow band spatial correlation function of the following form:

$$C(\xi, \eta, \omega) = e^{-0.0495 \frac{|\xi| \omega}{c}} e^{-0.126 \frac{|\eta| \omega}{c}} \cos \frac{\omega \xi}{c}$$

The only difference between the above expression and the progressive expression is the decay constants.

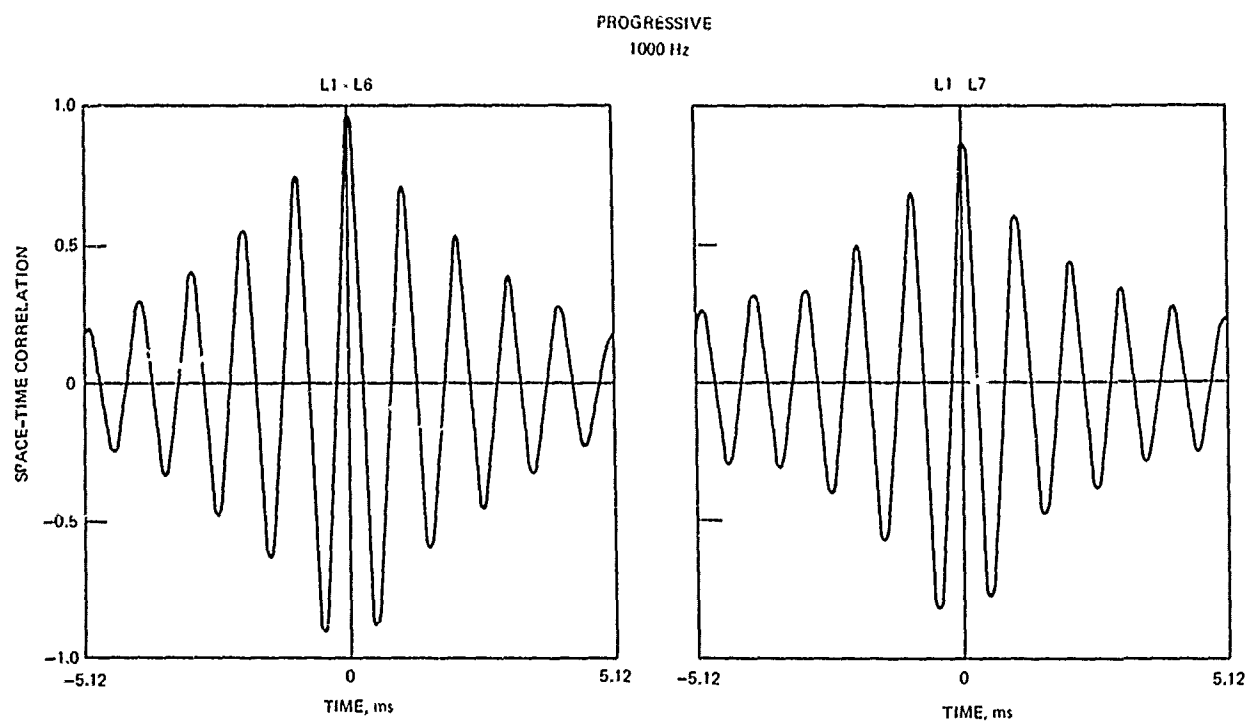


Figure 46. Circumferential Space-Time Correlation Data

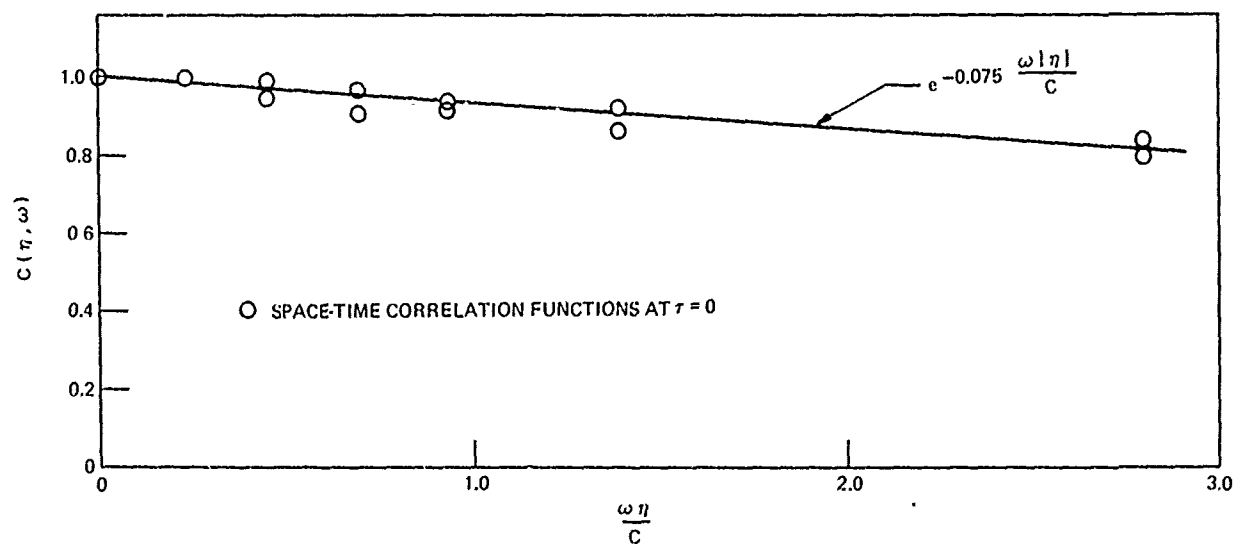


Figure 47. Circumferential Spatial Correlation Function

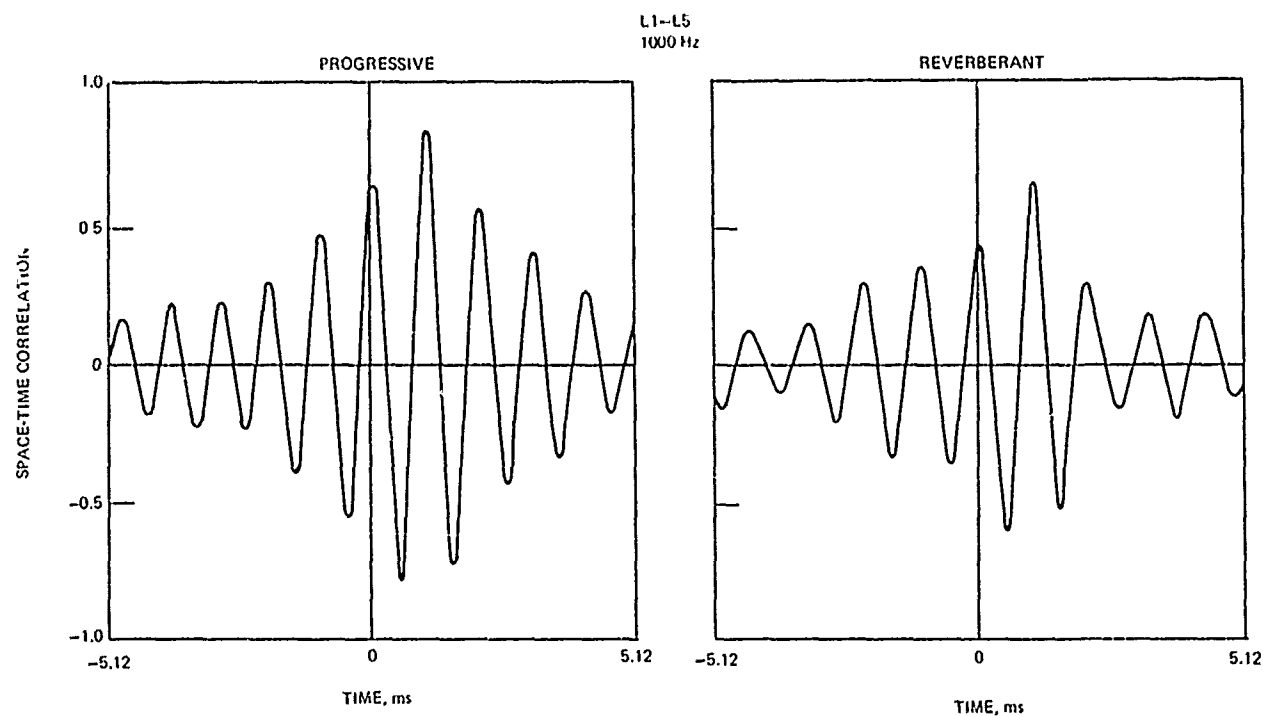


Figure 48. Meridional Space-Time Correlation Comparison

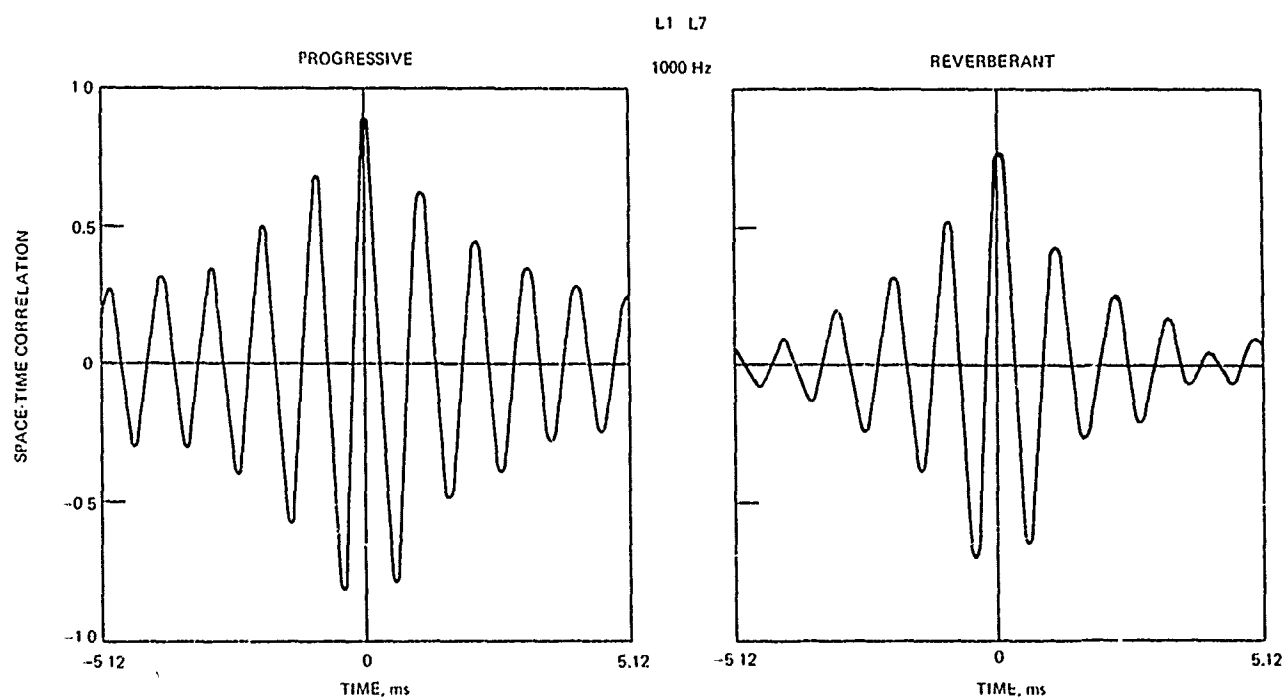


Figure 49. Circumferential Space-Time Correlation Comparison

2. TEST VIBRATION RESPONSE PREDICTION

Several modifications had to be made to the existing response prediction techniques in order to have the capability to predict the test response. These modifications were made to the existing progressive wave response formulation and were associated with the incorporation of the acoustic test spatial correlation functions.

The difference between the acoustic test environment and the perfect progressive wave environment is the exponential decay term in both the meridional direction and circumferential direction. The prediction technique revision in the meridional direction was easily implemented, as it just entailed the addition of this term to the correlation function. In the circumferential direction, the change was more significant. Fortunately the turbulent boundary layer (TBL) environment also contains an exponential decay term so the closed form solutions of the circumferential contributions to the force cross PSD for turbulent boundary layer are applicable for the acoustic test with small alterations. The turbulent boundary layer expression for the circumferential spatial correlation function is

$$C(\eta, \omega) = e^{\frac{-c_2 |\eta|}{\delta^*}}$$

whereas for the acoustic test

$$C(\eta, \omega) = e^{\frac{-c_2^1 |\eta| \omega}{c}}$$

It is seen that if c_2/δ^* is replaced by $c_2^1 \omega/c$, the closed form expressions for turbulent boundary layer presented in Section IV are applicable. These expressions have been incorporated into the computer-implemented progressive response formulation to result in a program with the capability of predicting the acoustic test response.

This program, coupled with an average of the pressure PSD of all the microphones from the progressive test, was used to predict the test response.

3. TEST-ANALYSIS CORRELATION

The acoustic test predictions were done only for the progressive test. Generally, good correlation was obtained between test data and the analytical predictions. There are a few instances where the correlation was poor, but these are readily explainable. Figures 50 throughout 62 show the test results and analytical predictions. The analytical results were obtained using the techniques of the previous subsection. In some cases the analytical mode shapes were altered to coincide with the test modes from the modal survey. Each of the figures will now be discussed.

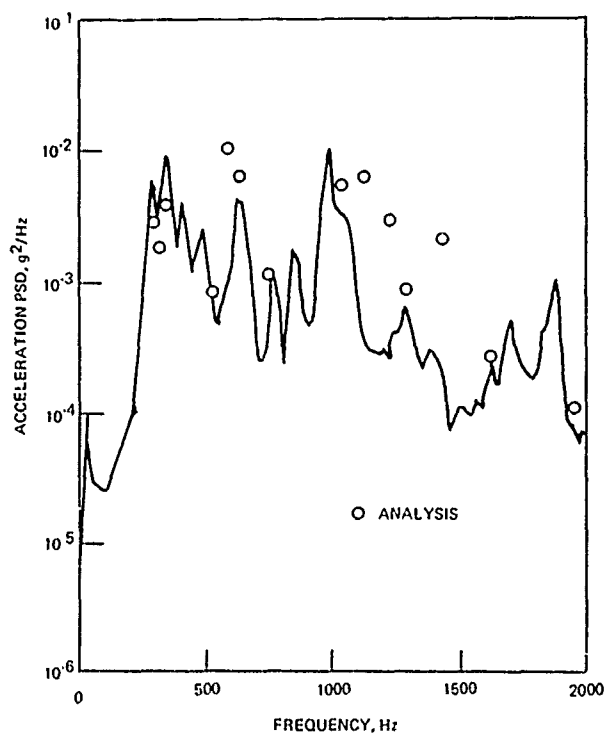


Figure 50. 1AL Vibration Response,
Test Vs. Analysis

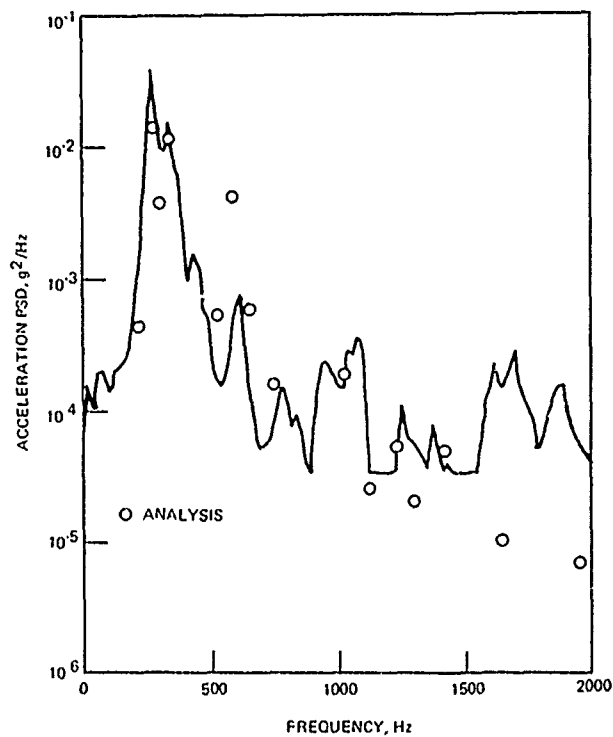


Figure 51. 1AT Vibration Response,
Test Vs. Analysis

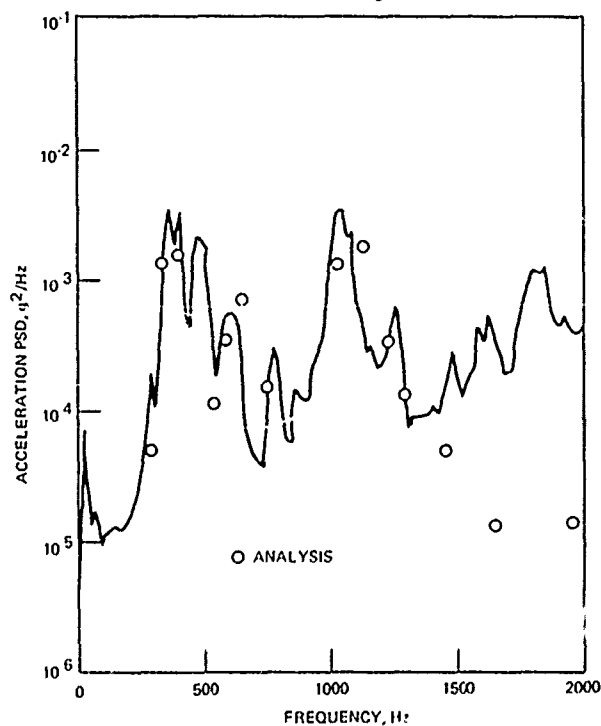


Figure 52. 3AL Vibration Response,
Test Vs. Analysis

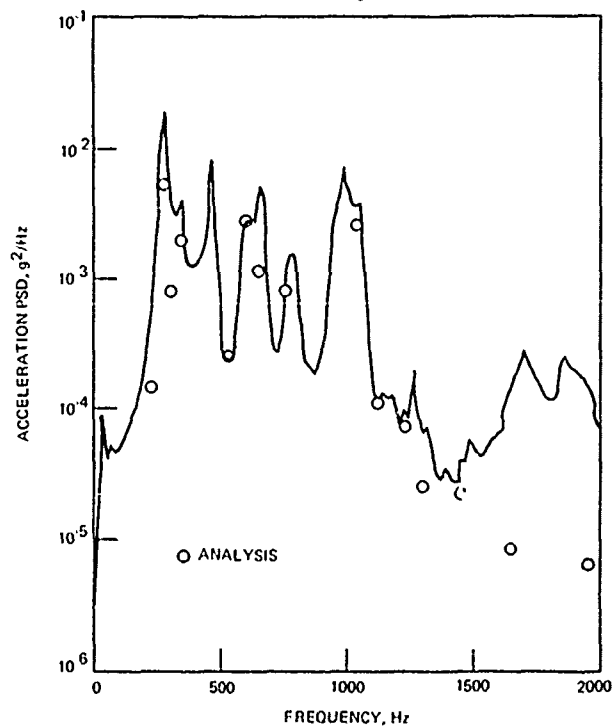


Figure 53. 3AT Vibration Response,
Test Vs. Analysis

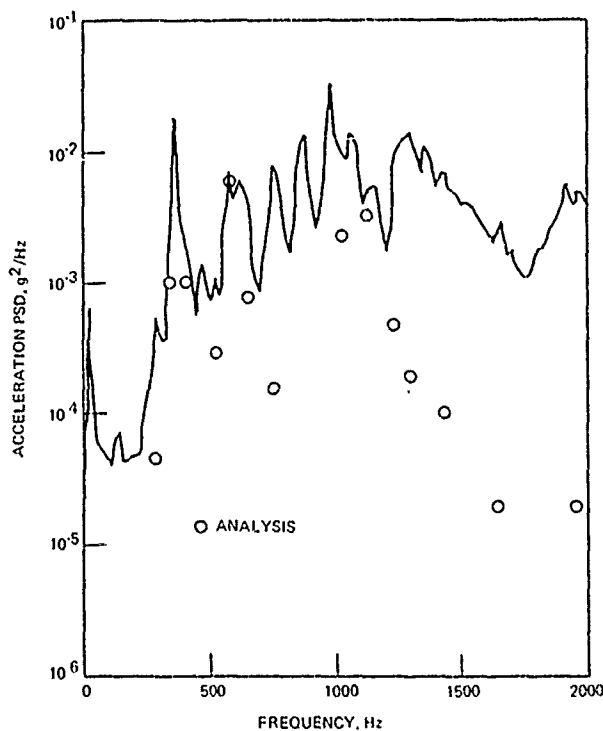


Figure 54. 4AL Vibration Response,
Test Vs. Analysis

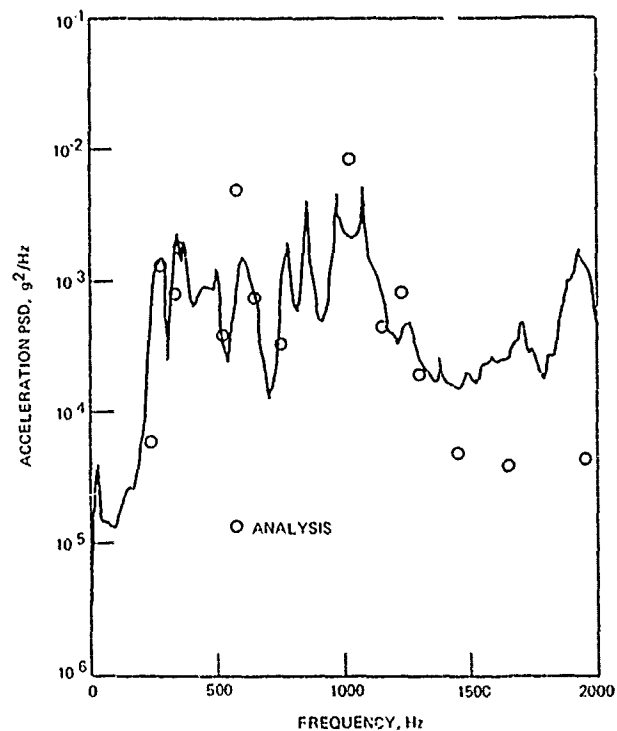


Figure 55. 4AT Vibration Response,
Test Vs. Analysis

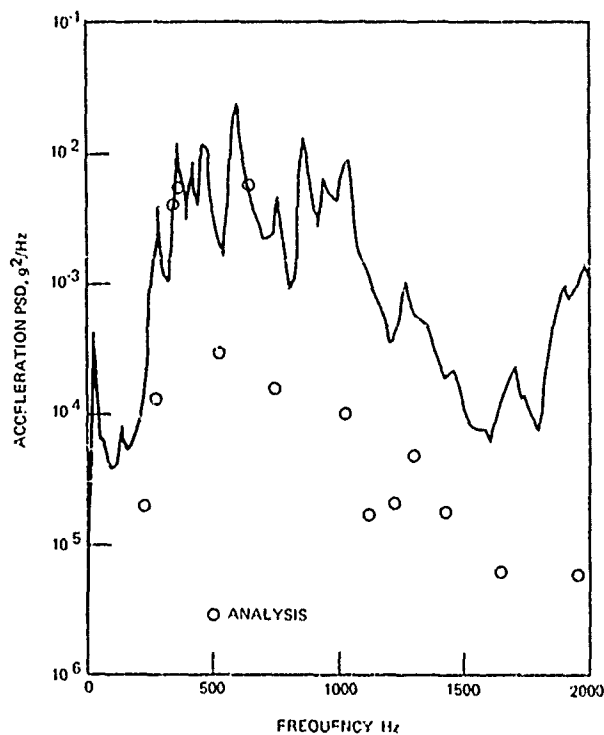


Figure 56. 5AL Vibration Response,
Test Vs. Analysis

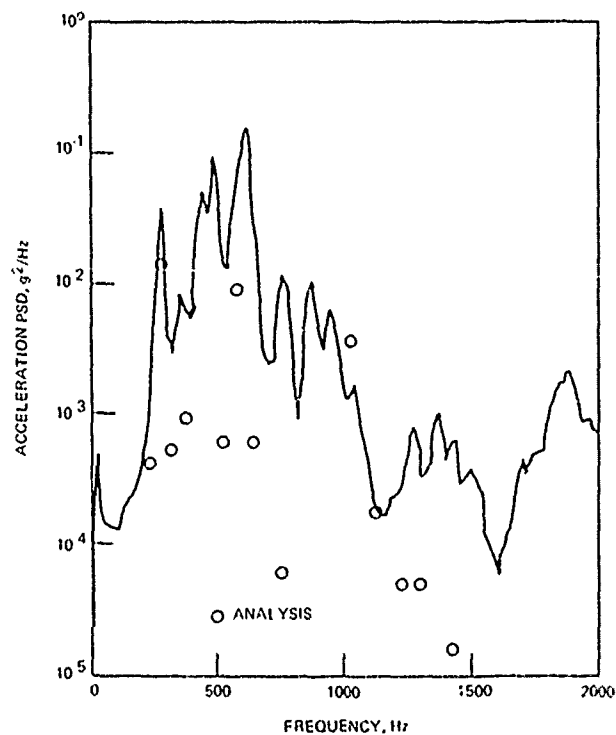


Figure 57. 5AT Vibration Response,
Test Vs. Analysis

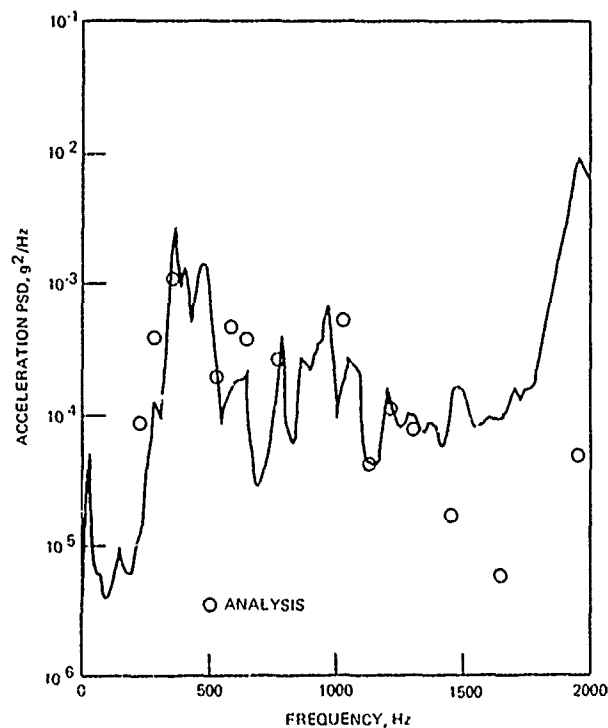


Figure 58. 6AL Vibration Response, Test Vs. Analysis

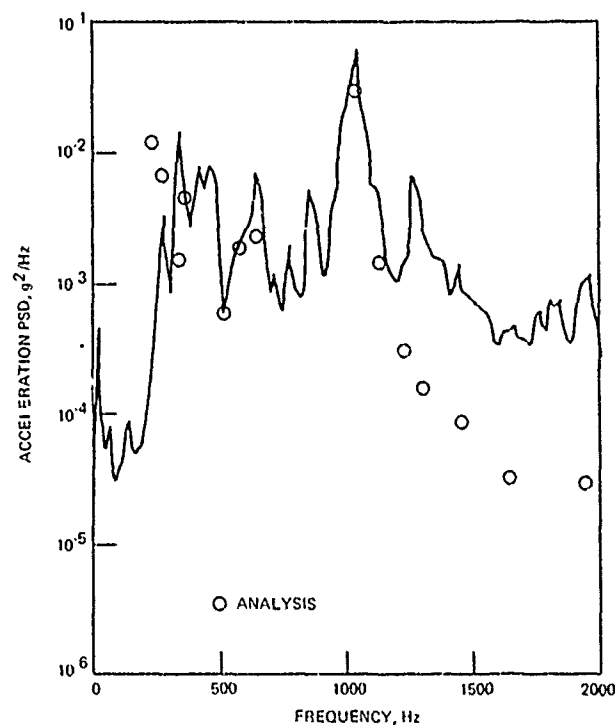


Figure 59. 6AT Vibration Response, Test Vs. Analysis

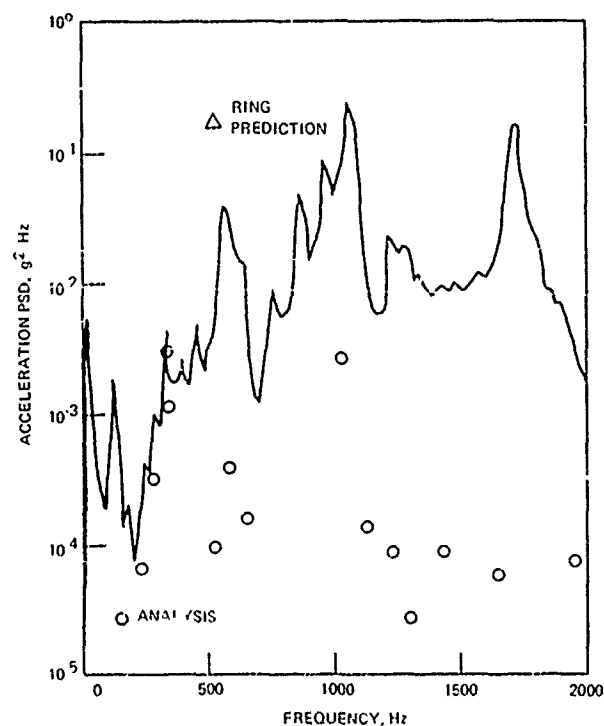


Figure 60. 8AN Vibration Response, Test Vs. Analysis

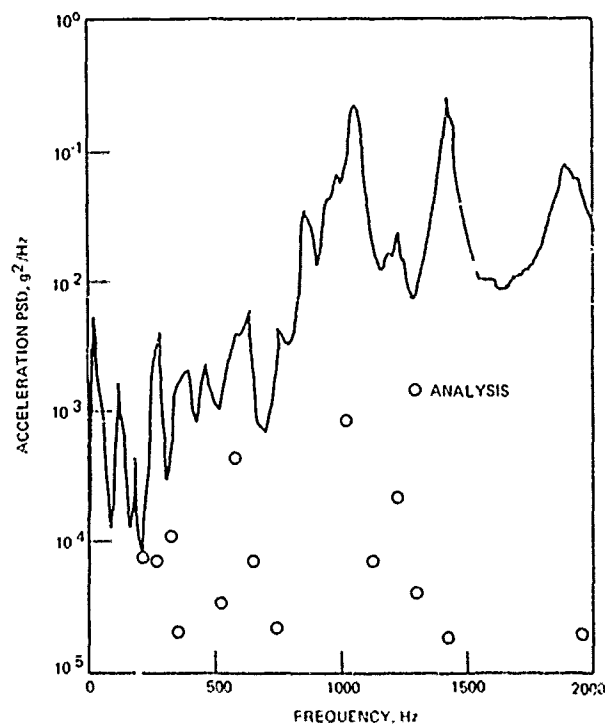


Figure 61. 9AN Vibration Response, Test Vs. Analysis

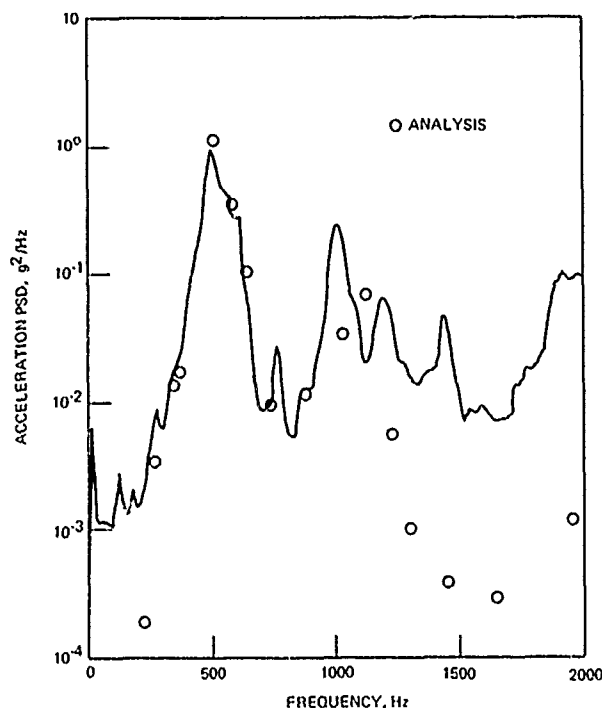


Figure 62. 10AL Vibration Response, Test Vs. Analysis

Figures 50 and 51 show analytical predictions for accelerometers 1AL and 1AT along with the test data. It is seen that good correlation between test peaks and analytical peaks exists below 1000 Hz. There are some test peaks which do not have a corresponding analytical prediction. One such frequency is 460 Hz. This test mode was obtained in the modal survey but no corresponding mode was obtained in the dynamic model. At the time of dynamic model correlation, it was believed that the 460 Hz mode would not exhibit large responses in the acoustic test. The test has proved this to be incorrect. On 1AL a test peak at 850 Hz is noted. This frequency did not show up in the modal survey, and is likely a frequency associated with the other orthogonal lateral direction. Between 1000 and 2000 Hz more discrepancy is noted between predictions and test data. This is to be expected, because the analytical modes were not as well correlated with modal survey test modes. In fact, above 1500 Hz no test modes were found in the modal survey, but there are modes evident in the acoustic test. These modes could possibly be higher order component modes which were not excited by the re-entry vehicle nose input used in the modal survey. The trend of analytical predictions being less than test data above 1500 Hz is present on almost all figures, and is attributed to these modes.

Figures 52 and 53 show analytical and test data for accelerometers 3AL and 3AT. Again good correlation is noted at frequencies below 1500 Hz. On these two figures the 460 Hz mode is more evident. The dropoff above 1500 Hz is also noted.

Figures 54 and 55 show comparisons for accelerometers 4AL and 4AT. Poor correlation is noted for 4AL. It is also observed that the test peaks for 4AL occur primarily at lateral frequencies: 268, 579, 750, 950, and 1050 Hz. The lateral contribution in this axial accelerometer is realized analytically by multiplying the rotational coordinate in the lateral model at this accelerometer location by a moment arm (0.625 inches) to account for the offset from the EP axis (see Section VI). In order to significantly raise the response at these lateral frequencies, the analytical rotational coordinate would have to be increased in each mode or the value of 4AL due to lateral motion known. There is no way to know exactly how much to alter this rotational coordinate based on the modal survey, since it is difficult to measure this quantity, and only lateral motion at the three EP stations were defined in the lateral modal survey. This was one of the shortcomings of the modal survey, and will be discussed more fully in Section XI.

Figures 56, 57, 58, and 59 show the correlation for accelerometers 5AL, 5AT, 6AL, and 6AT, respectively. These accelerometers are located in the TM package. It is on these plots that, in some cases, the test mode shape values were substituted into the analytical mode shape description to give better correlation with the modal survey data. It is seen that good correlation exists on Figures 58 and 59 and poor correlation on Figure 56 and 57. On all of the figures the peak at 460 Hz is noted, which again is not analytically predicted. It is also noted that the axial accelerometers exhibit peaks at lateral frequencies. There is a rotational coordinate in the dynamic model which corresponds to the 6AL and 6AT accelerometer locations. This coordinate was therefore used in conjunction with the proper moment arm to include in the 6AL response the lateral frequencies. Unfortunately, no such coordinate in the dynamic modal was included for the 5AL and 5AT accelerometers; therefore 5AL does not analytically exhibit lateral frequency response and so does not correlate well with the test data.

Figure 63 shows a comparison between the analytical mode shape and experimental one at 650 Hz. It is observed that the analytical mode shape predicts the same response for 5AL and 6AL which is between the two test values. These two test values were substituted within the analytical mode to improve the correlation. This was one example of substituting test values. It was in the TM area where the substitution of the test values was required. This was due to the inherent complexity associated with modeling the TM package. An interesting observation can be made by comparing 5AT test response at 730 Hz with the test mode shape at that frequency in Volume II of this report. It is seen that 5AT exhibits no response in the modal survey at 730 Hz, yet responds significantly in the acoustic test. No doubt the difference in the two environments accounts for this phenomena. It is also seen that neither 6AL or 6AT exhibit any response at all at 2000 Hz in the modal survey, yet have large peaks in the acoustic test. This problem in achieving good correlation in the TM package points out the need for modal surveys of the package itself, to make sure the dynamic model is of sufficient detail to accurately describe the dynamic characteristics, or to point out the need for use of test modal data exclusively.

Figures 60 and 61 show axial and lateral model predictions for accelerometers 8AN and 9AN. It is obvious that the correlation is terrible, so it was decided to investigate higher harmonic dynamic models. (Remember that the axial and lateral model are the 0th and 1st harmonics,

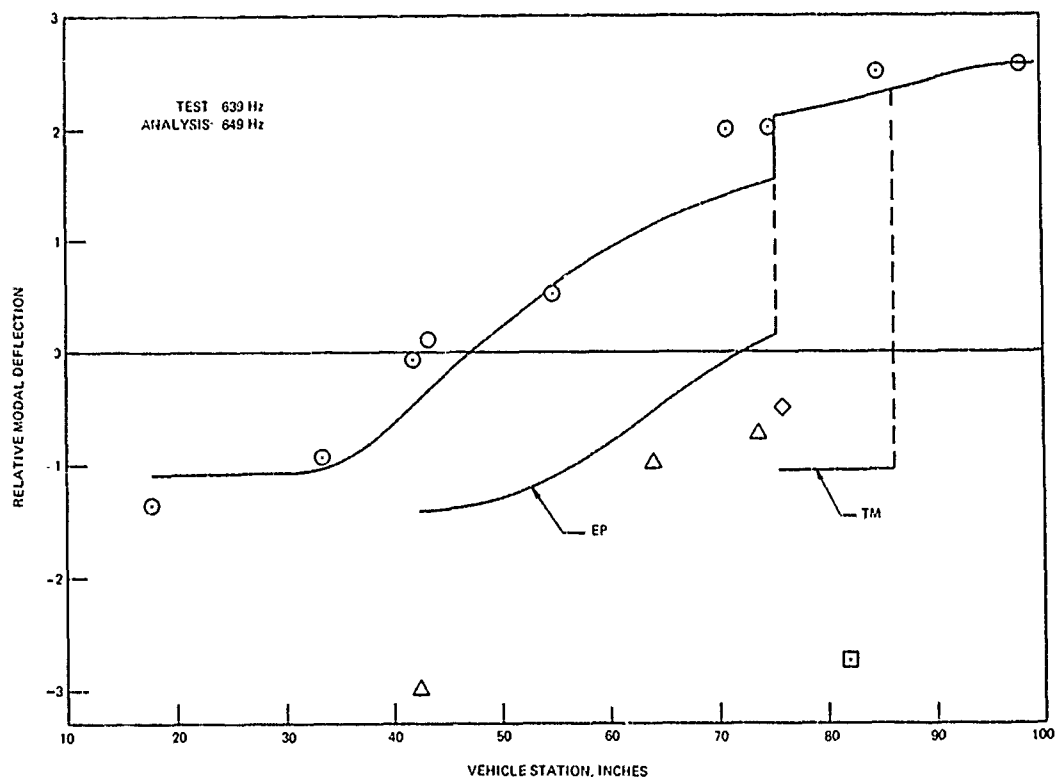


Figure 63. Axial Mode Shape, Test Vs. Analysis

and higher harmonics are two and above. This means that the circumferential shell displacement varies as $\cos n\theta$, where n is the harmonic number). In order to do this a one inch strip of the shell at 8AN was treated as a ring in lieu of using a higher harmonic SABOR model which would take more time. The frequency associated with the second harmonic, or ovaling mode, was computed at 520 Hz. The response was then determined and found to correspond to the point shown on Figure 60. It is then concluded that the significant response peaks on Figures 60 and 61 are associated with higher harmonic modes rather than the fundamental axial and lateral models. This indicates that for skin or shell mounted components higher harmonic models must be utilized in addition to the fundamental modes to get accurate response predictions and resulting skin-mounted component environments.

Figure 62 shows the predictions and test data for accelerometer 10AL. This figure shows that the response prediction technique is indeed accurate. The aft cover is a simple structure, with the 520 Hz mode being accurately described by the dynamic model. It is seen that the peak response exactly coincides with the test response at this frequency.

Based on Figures 50 through 62, it is concluded that the response prediction technique is accurate and verified. There are several suggestions which must be made to ensure the techniques accuracy. A modal survey (three axes) is a definite aid in establishing a representative dynamic model with requirements for recording all accelerometers in each axis of excitation. In fact, without the modal survey it is unlikely that the prediction technique could be verified because the initial dynamic models had to be significantly reworked to

obtain the accuracy required. The acoustic test pointed out the need for including higher harmonic shell responses for skin components. Dynamic models and subsequent response predictions are required for both lateral axes, not just one lateral axis.

4. DISCUSSION

There are several areas which should be elaborated upon as a result of the test-analysis correlations. As pointed out in the previous subsection, the developed prediction technique from Section IV is indeed an accurate and powerful tool. However, it is based on finite element dynamic models. The previous subsection clearly demonstrates that dynamic model accuracy is of prime consideration if accurate predictions are to be made. The correlation analysis showed several shortcomings of the modal survey in ensuring an accurate dynamic model. Perhaps the biggest deficiency was the failure to monitor the lateral accelerometers, whose sensitive axes were other than the test direction. The acoustic test clearly showed axial accelerometers responding at lateral frequencies, which was not unexpected. However, because of the failure to monitor the axial accelerometers during the lateral modal survey, there was no means to guarantee that the dynamic model accurately predicted this response.

Another problem, which was reflected by the poor correlation above 1000 Hz, is that the nose force input to excite the vehicle resonances did not excite the higher-order component modes. This is because the mode shapes associated with these modes have little nose motion, thereby resulting in insufficient modal force in the survey to excite them. A way around this would be to excite the vehicle at the locations where the component packages tie into the shell structure. A better solution would be to run detailed modal surveys of the component packages themselves. This would guarantee that the dynamic model is of sufficient detail in the component areas to describe their dynamic characteristics.

The correlation analysis of the previous subsection clearly demonstrated that if shell acceleration response predictions are desired, then the dynamic models must include higher harmonics. The inclusion of higher harmonic models is only required in the event that a small component is mounted to the vehicle shell and the component's vibration environment is desired. Both the acoustic test and the re-entry predictions demonstrated that the strains induced into the shell structure are of little consequence with respect to shell ultimate strength capability.

To summarize, the prediction technique does an excellent job of describing re-entry vehicle vibration response. However, care must be taken to insure the vehicle dynamic characteristics are accurately portrayed.

SECTION IX

VEHICLE RE-ENTRY SIMULATION TECHNIQUES

1. CURRENT AEROACOUSTIC ENVIRONMENT DESCRIPTION

The most current description of aeroacoustic environments during re-entry of high-beta vehicles is contained in Reference 23. This reference documents the results of a study contract conducted at GE-RESO concurrently with this study program, but which focused on improving the description of aeroacoustic loadings.

The acoustic description of Turbulent Boundary Layer (TBL) flow in terms of Overall Sound Pressure Level (OASPL), Power Spectral Density (PSD) and spatial correlation is essentially the same as that given in Section III. Significant asymmetric OASPL distributions about the vehicle roll axis do, however, occur for angles of attack in excess of the vehicle cone half angle because of separated flow.

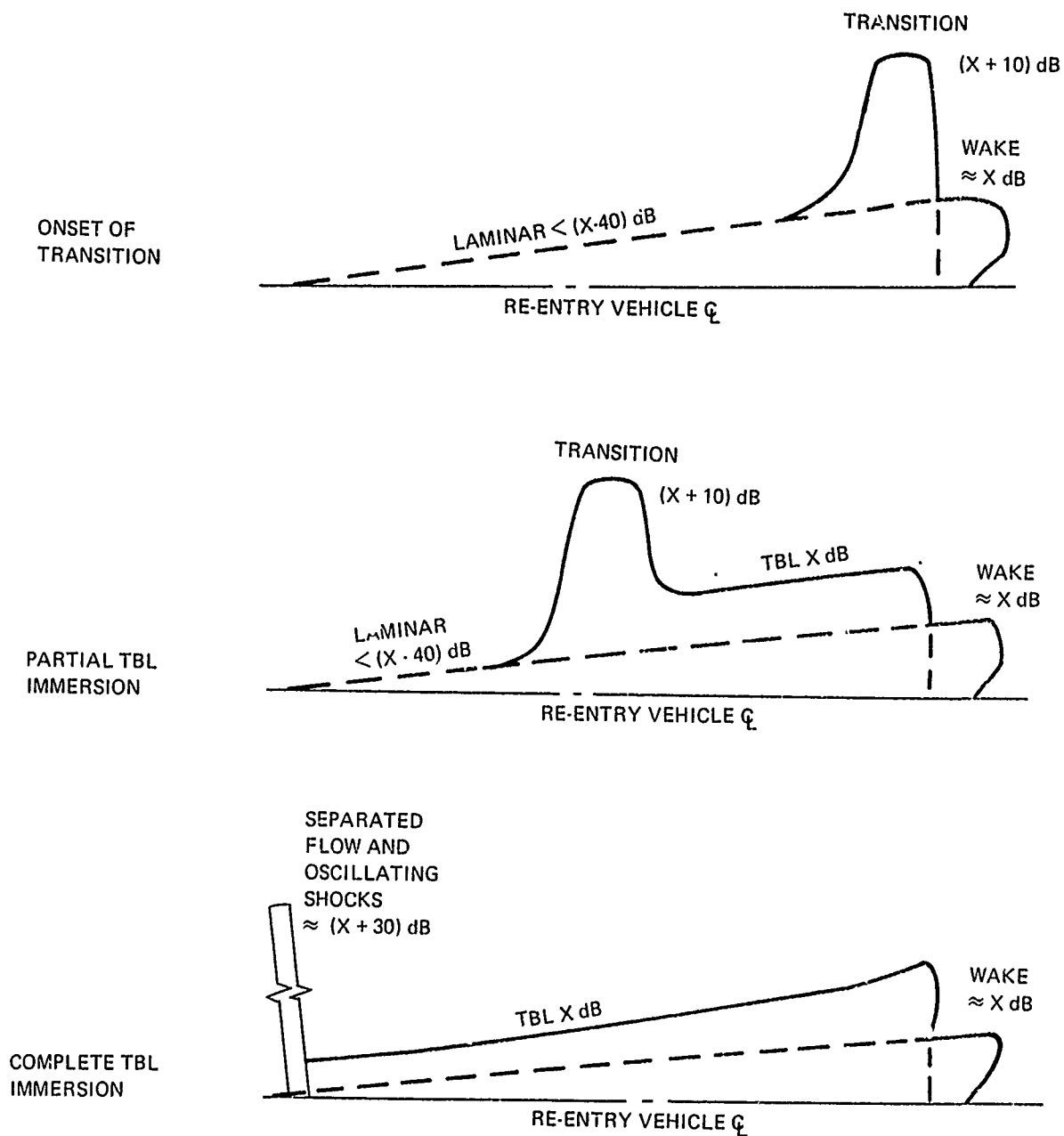
Transitional flow acoustic environment has an OASPL of approximately 10 dB greater than the TBL flow environment, but retains similar characteristics as TBL in PSD and spatial correlation. The length of vehicle affected by transitional flow is approximately equal to the local vehicle radius.

Wake flow OASPL is approximately equal to TBL flow, not 15 dB less than TFL as defined in Section III. Its PSD is higher than TBL in the frequency region less than 5000 Hz. Spatial correlation is assumed to behave as previously described.

Data obtained from recent flights with severe trajectories indicates that aerodynamic oscillating shocks can be set up on the vehicle nose if tip-ablated shapes create separated flow. Published data (24), (25) indicates that these oscillating shocks produce very severe OASPL, 30 dB higher than TBL, with very low frequency content, less than 100 Hz. The shock acoustic pressures are fully correlated along the flow direction (vehicle roll axis), but fully correlated over only one quadrant across the flow or around the vehicle circumference.

The combinations of the various aeroacoustic environments are depicted in the schematics of Figure 64 for three significant flow conditions that occur during re-entry. During early re-entry, the vehicle forebody is completely immersed in laminar flow. An altitude is soon reached where transitional flow occurs at the rear of the vehicle. As the vehicle further penetrates the atmosphere, the transitional flow zone moves forward on the vehicle, with turbulent flow occurring aft of the transitional flow zone. Finally, transition reaches the nosetip and the vehicle is completely immersed in turbulent flow. In addition, at this point in the trajectory, transition causes increased heating and subsequent ablation of the nosetip. Depending on the shape that the ablated nosetip assumes, separated flow and oscillating shocks can occur at the nose, both phenomena causing very high overall sound pressure levels.

OVERALL SOUND PRESSURE LEVEL DISTRIBUTIONS



NOTE: TBL - TURBULENT BOUNDARY LAYER
 X dB - OVERALL SOUND PRESSURE LEVEL FOR TBL

Figure 64. Current Aeroacoustic Environment Description

2. CURRENT RE-ENTRY VIBRATION ENVIRONMENT DESCRIPTION

Vibration environments at internal shelf-mounted components measured during nominal re-entry flights are mild. Figures 65 and 66 show these typically mild vibration environments measured during period of transitional flow and fully turbulent flow respectively. The high levels on these figures at very low frequencies are due to vehicle rigid-body aerodynamic pitching response.

No data from vehicle forebody shell and aft cover (base) are available for nominal flights. Data recently obtained, however, during very severe re-entry trajectories show extremely high (4000 g's) intermittent acceleration pulses of short duration (0.1 millisecond) occurring on the vehicle forebody shell structure. These levels were estimated by using triggering characteristics of high-g switches and saturation characteristics of vibration sensors. The cause of this phenomena is presently attributed, either directly (linear response) or indirectly (nonlinear response), to oscillating aerodynamic shocks on the vehicle ablated nosetip. The vibration environment occurring during transition on these severe trajectories and prior to nosetip ablation was mild, and that occurring in conjunction with the intermittent acceleration pulses could not be defined because of sensor saturation.

3. SIMULATION TECHNIQUES

The two areas which must be investigated in order to insure that a ground test of a vehicle will simulate the re-entry response are the vehicle dynamic characteristics and the

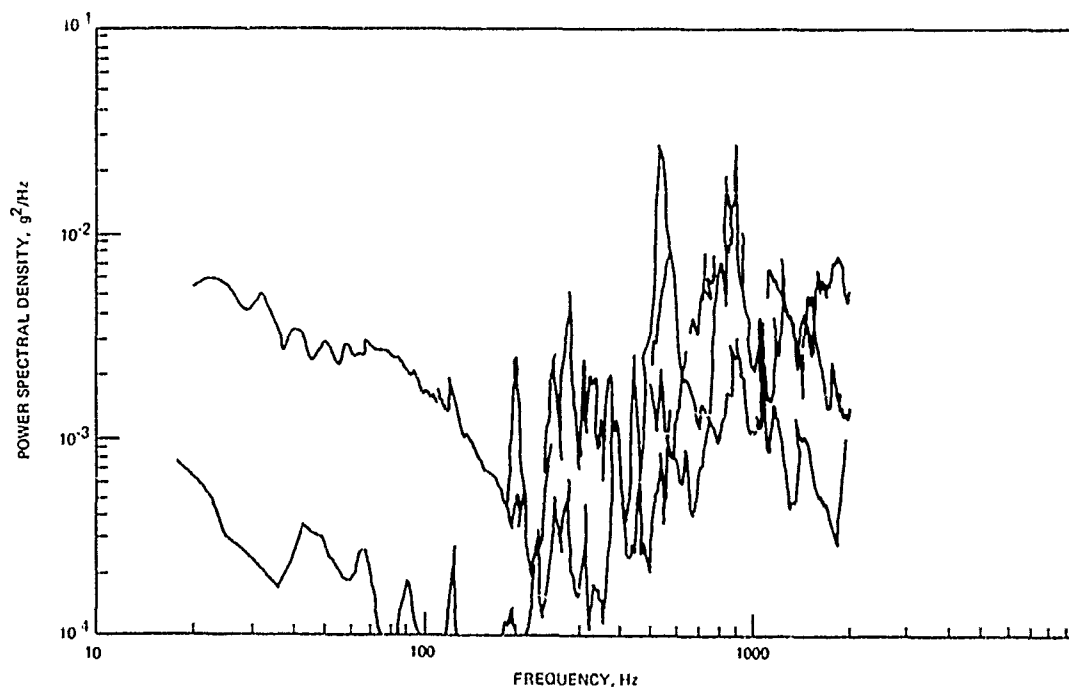


Figure 65. PSD Envelope For Internal Components-Transition

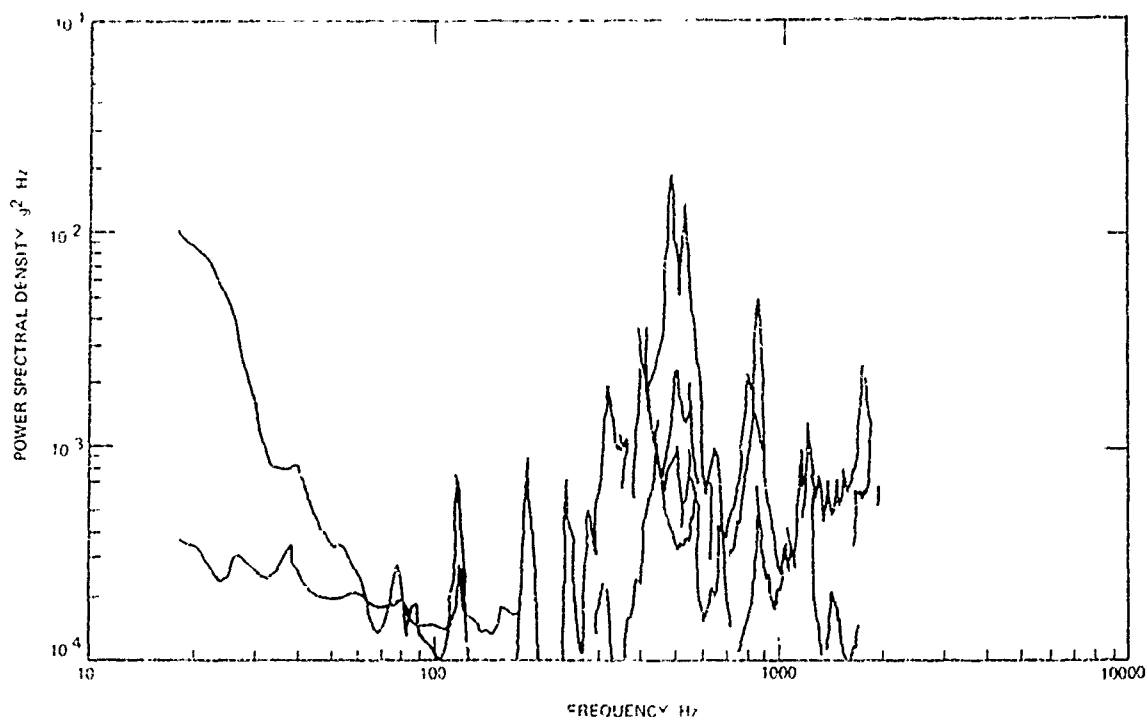


Figure 66. PSD Envelope For Internal Components - TBL

aeroacoustic loading. During re-entry, the heat shield will be ablating, the re-entry g loads will alter conditions of preload at the joint locations, and the increased temperature will reduce stiffness of the shell. These effects all combine to change the vehicle dynamic characteristics compared to those of a ground test vehicle. It is extremely difficult and costly to modify an unaltered prime vehicle to the point where it has the exact dynamic characteristics as a re-entry vehicle. Some things can be done, however, to approach the ideal condition. If the effect of the re-entry g loading is to loosen field joints through reducing the assembly preload, this could easily be represented by lower assembly preload. Although costly, it is possible to design and fabricate a heat shield which describes the predicted re-entry ablated condition of reduced thickness and modulus.

Techniques for simulating the aeroacoustic environments are shown schematically in Figure 67 for the three flow conditions previously described in Figure 64. It is seen that simulation of the movement of transition down the vehicle entails the use of baffles; this should present no problem, since it was done in the testing performed in the AFFDL Sonic Fatigue Facility. Simulation of the oscillating aerodynamic shocks and separated flow on the vehicle also requires local random force input utilizing a shaker. If the intermittent high acceleration pulses described previously are due to a nonlinear vehicle response such as field joint or equipment shelf impacting, then the shaker input through snug-fitting connectors should suffice. If, however, the intermittent acceleration pulses are due to a

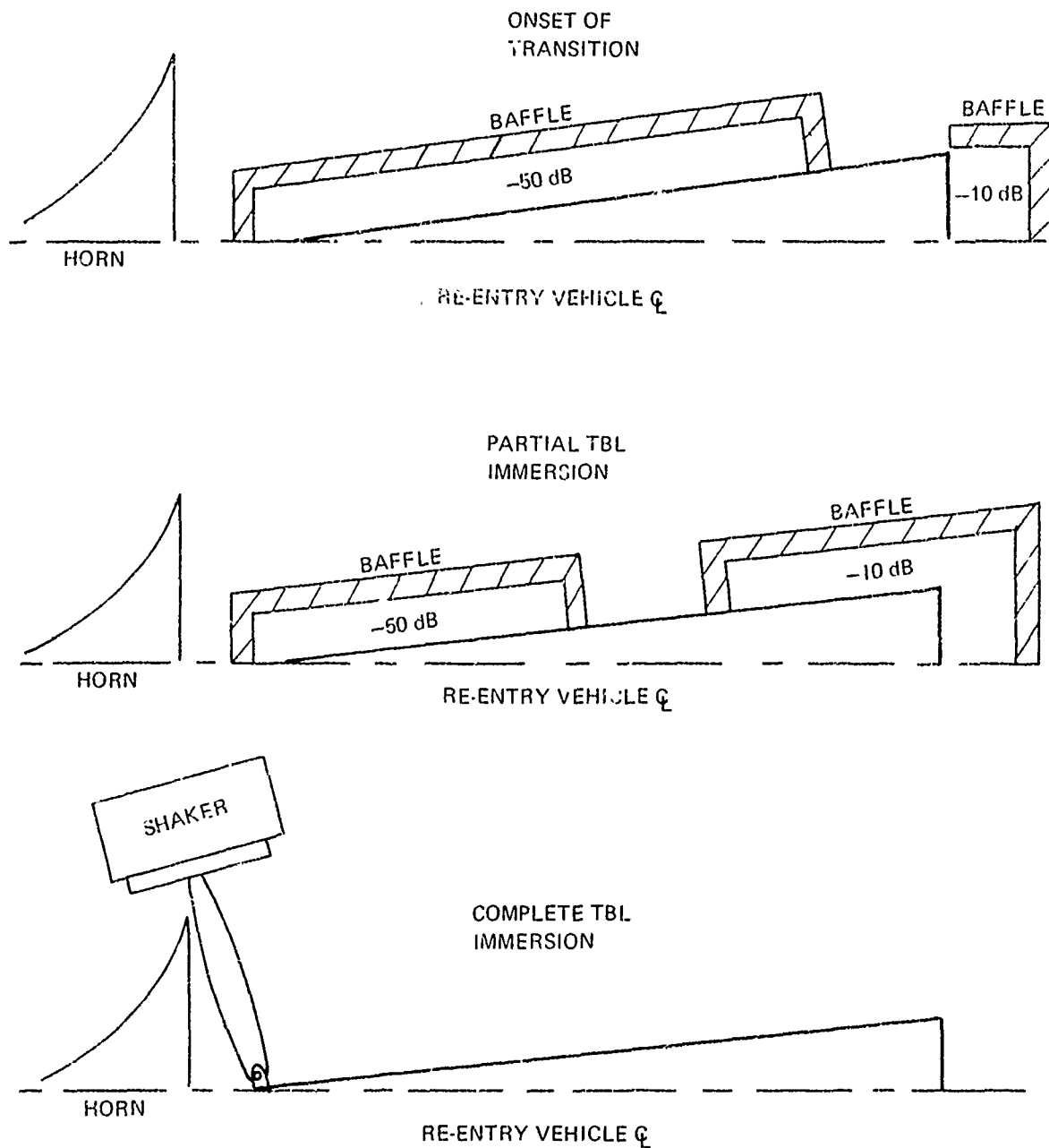


Figure 67. Re-entry Response Simulation Technique

similarly described aerodynamic shock loading on the vehicle nosetip, then an impacting device, such as loosely fitting connectors at the nose, must be used in conjunction with the shaker.

Finally, adequate simulation may demand that the test vehicle be mounted on springs such that a rigid body pitch and yaw frequency (≈ 20 to 40 Hz) similar to re-entry is realized, since some components may be susceptible to low-frequency environments.

4. AFFDL SONIC FATIGUE FACILITY CAPABILITIES

This facility has several test chambers. The large test chamber has the average physical dimensions of $42 \times 56 \times 70$ feet, and can be operated in either the reverberant mode or progressive wave mode. The high intensity sound in the test chamber is generated by 35 discrete frequency sirens with a range of 50 to 10,000 Hz. The sirens can be modulated to produce a narrow band random noise. A maximum acoustic power of one million watts can be radiated from the main bank within a limited frequency range. A maximum overall sound pressure level of 174 dB can be attained near the sirens. Full scale specimens can be tested in sound fields up to 162 dB (re 0.0002 dynes/cm²). Seventy-two channels of data can be recorded simultaneously by the facility instrumentation system, with the capability of recording 342 transducer outputs by commutating a number of data channels. There is also a smaller test chamber scaled to one-fourth the physical dimensions of the large chamber. This facility is powered by a 12 kilowatt wide-band siren capable of producing a continuous spectrum over a frequency range of 50 to 12,000 Hz. A maximum overall sound pressure level of 160 dB can be attained at the siren horn mouth.

As mentioned previously in various sections of this report, the acoustic test performed with the prototype vehicle in the AFFDL Sonic Fatigue Facility did an excellent job of simulating responses to the baseline re-entry environment, even though the overall sound pressure levels were lower than predicted for re-entry. This remark can be made since the component responses in the acoustic test, as measured by the accelerometers, exceeded the responses predicted for the baseline re-entry aeroacoustic environment. In summary, it can be stated that the AFFDL Sonic Fatigue Facility adequately simulates re-entry, since the correlation effects of the test chamber's semi-progressive environment yields vibration responses equivalent to re-entry, at overall sound pressure levels much lower than re-entry aeroacoustics.

SECTION X

DESIGN REQUIREMENTS, TEST SPECIFICATIONS

1. SPECIFICATION DERIVATION GUIDELINES

The basis for design requirements and test specifications are vibration predictions for all significant re-entry flow conditions at all component locations, utilizing the analysis and test procedures previously discussed. The initial task in specification derivation is to overlay the three axes of response for each component, as one specification for all axes of testing is desired. If a component is used at more than one location in the vehicle, then the responses at all locations and all axes must be overlaid. A test specification is then derived by enveloping the peaks of the response overlays. Notching of the specification is appropriate only if the response overlay peaks occur in groups at widely separated frequency bands as shown in Figure 68. However, notching is rarely possible in defining re-entry vibration specifications because of the wide band nature of the aeroacoustic environment. Rolloffs of the test specification about the response peaks should not exceed 12 dB/octave to be compatible with test machine control limitations.

Experience has shown that enveloping procedures just described, results in test overall levels that are approximately twice the response overall levels, thus providing sufficient conservatism. Additional safety margin is provided by the test duration, which should be approximately ten seconds per axis or thirty seconds total test time. Re-entry flight time from onset of transition to impact is on the order of ten seconds, with duration of highest level vibration even less than that. The short duration of test time will require the use of a near prime component simulator to be used in shaping the test specification during initial testing.

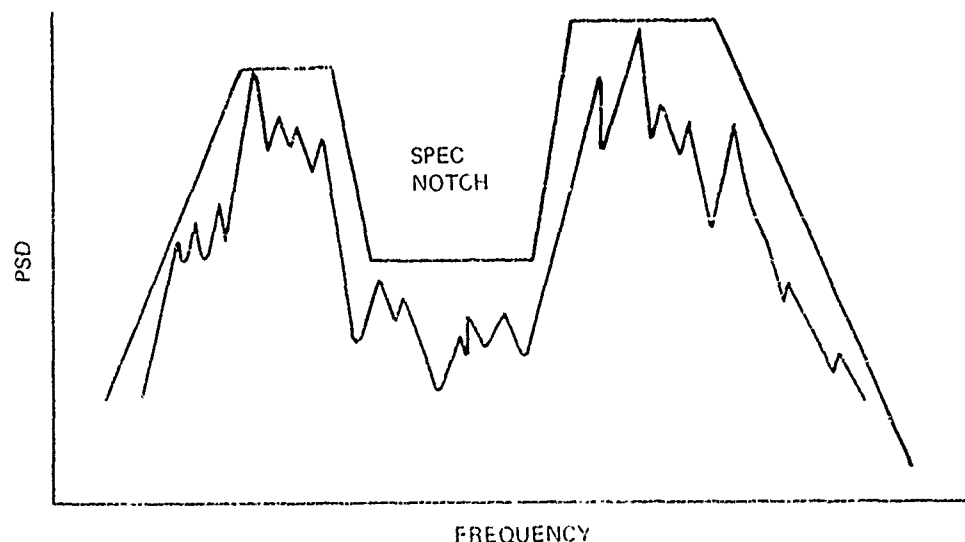


Figure 68. Test Specification Notching

2. TYPICAL COMPONENT TEST SPECIFICATIONS

Utilizing the numerous re-entry response analyses conducted on GE-RESO high-beta re-entry vehicle programs and available flight data, typical component test specifications were developed using procedures discussed above. Figures 69 and 70 display the results of this effort with test specification for internal shelf-mounted components and shell-mounted (forebody, aft cover) components respectively. The figures provide the ability to define realistic component re-entry vibration specifications for proposal or preliminary design purposes, but obviously more representative curves should be derived for a specific vehicle, utilizing the analysis and test procedures outlined in this report.

An attempt is made in Figure 71 to give a best estimate of acceleration shock pulse environments experienced in the vehicle shell structure if nose ablation causes nosetip separated flow and oscillating shock waves.

3. INTERNAL ACOUSTIC ENVIRONMENTS

Previously, in Section VII, it was noted that vehicle internal acoustic environments measured in the testing at AFFDL Sonic Fatigue Facility had overall levels 36 dB lower than the external acoustic environment. This means the external excitation is fifty times greater than the internal environment, and therefore acoustic excitation of components in conjunction with vibration testing is not necessary.

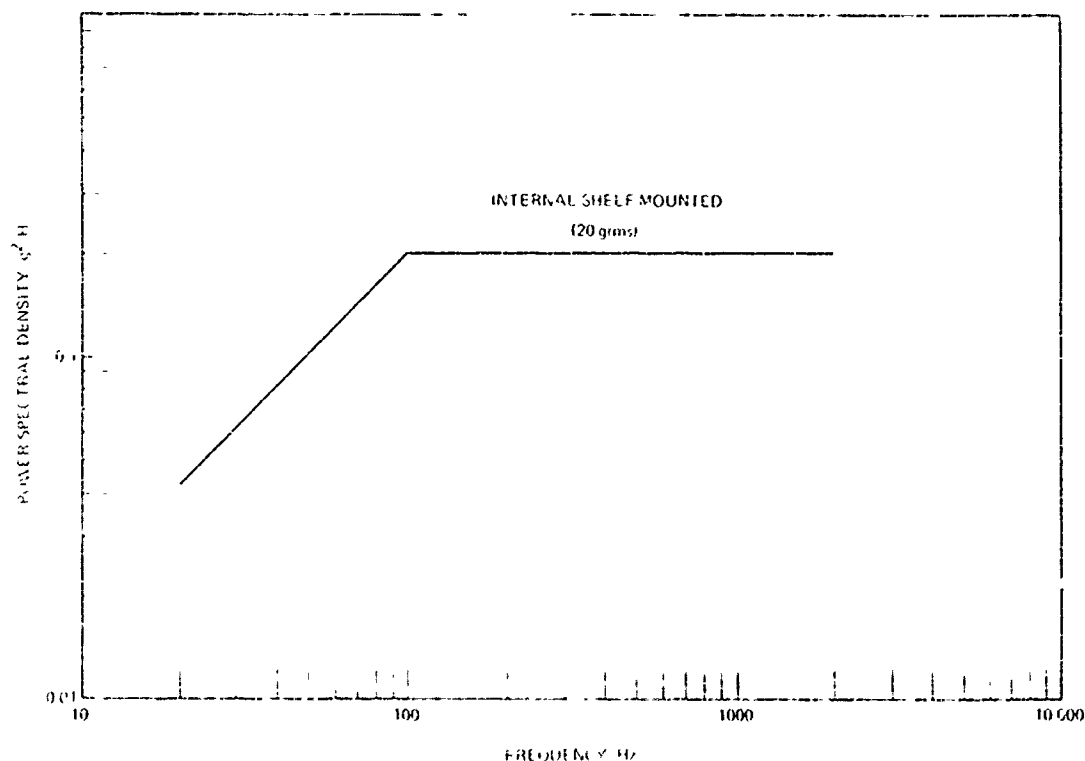


Figure 69. Component Re-entry Vibration Test Specification (Internal Self Mounted)

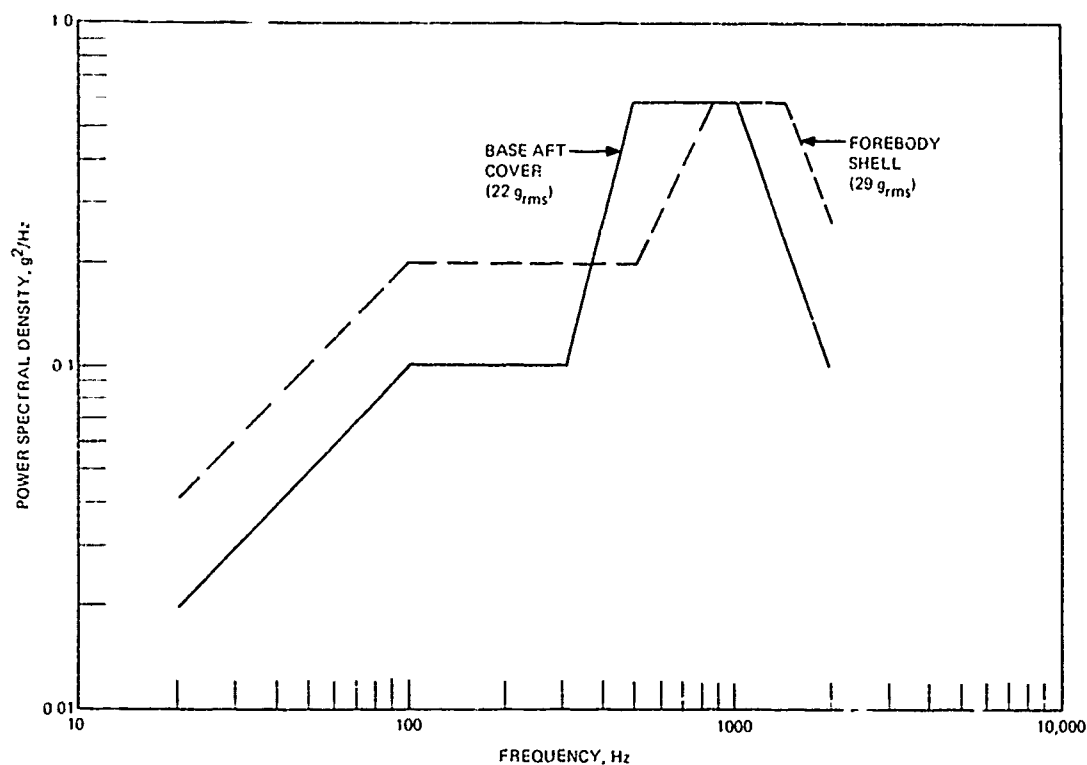


Figure 70. Component Re-entry Vibration Test Specification (Forebody Shell and Base)

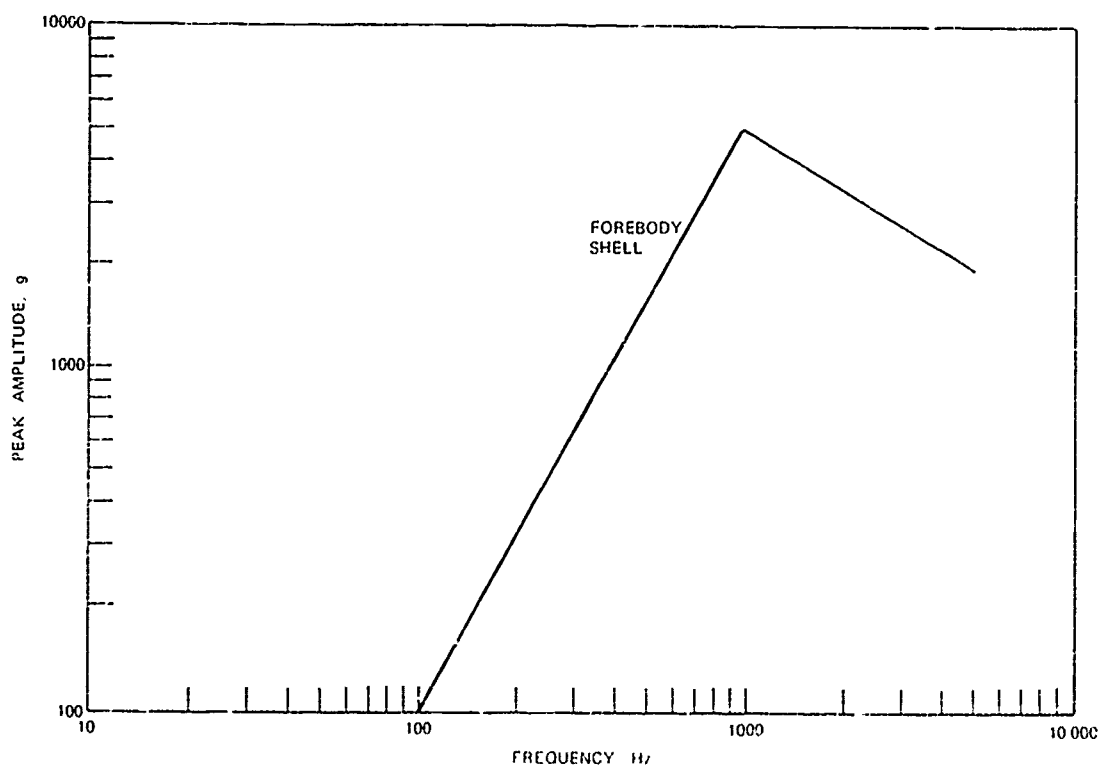


Figure 71. Component Re-entry Shock Test Specification

SECTION XI

CONCLUSIONS AND RECOMMENDATIONS

1. VIBRATION RESPONSE PREDICTIONS

The main objective of this study contract in developing a verified vibration response prediction technique has been achieved. However, the results of the test/analysis correlation have illuminated certain areas previously not addressed or little understood. Primarily, it is now evident that aeroacoustic environments cause significant responses in all three axes of the vehicle. Prior to this study, it was thought that axial response was dominant and the nodal survey and acoustic tests were planned accordingly.

A very significant item learned from the acoustic test is that the acoustic environment also excites vehicle shell modes, which become the largest contributor to shell response. Finally, test results reveal that internal component shelves are excited at their higher resonant frequencies as well as the expected lower modes.

Based on the results of this study, the following is recommended in predicting vibration response to acoustic environments:

- (1) All vehicle axes should be considered simultaneously in analytical predictions.
- (2) Shell response should be modeled.
- (3) Modal surveys for dynamic model verification should be conducted in each vehicle axis, monitoring all axes of internal responses.
- (4) High frequency modeling of internal equipment shelves must be included.
- (5) Modal surveys of internal equipment shelves alone should be done, or at least provision for excitation at shelf attachment structure during vehicle modal surveys should be made.

2. ACOUSTIC TESTING

The utilization of a nose/fixture combination was an excellent approach for providing nose excitation and vehicle suspension during acoustic tests.

It is certainly evident from the acoustic test results that either type of chamber configuration (reverberant, or progressive) is sufficient. This is because the proximity of the vehicle to the siren bank precludes good reverberation; hence the environment tended to be progressive. The acoustic environment provided enough spatial correlation decay around the vehicle circumference to cause sufficient lateral response. The use of baffles to alter acoustic environments has been proven to be an effective testing technique.

In future acoustic testing it is recommended that:

- (1) more microphones be placed to record circumferential variations in acoustic environment;
- (2) use of strain gage instrumentation be eliminated because of extremely low levels; and
- (3) high and low frequency portable sirens should be employed to raise sound pressure levels in those frequency bands.

3. SIMULATION TECHNIQUES

The fairly well-defined types of aeroacoustic environments (turbulent boundary layer, transition, wake) are at best difficult to simulate in ground tests. Simulation of oscillating shocks and separated flow will require a better definition of these environments. In summary, exact simulation of aeroacoustic environments in ground tests is virtually impossible, and therefore simulation of responses is most expedient.

The primary recommendation of this study program is that, now that feasibility has been demonstrated, further tests and analyses should be performed to thoroughly evaluate the response simulation techniques proposed in this report. This effort should also include tasks to determine if nonlinear responses in a vehicle structure could result in high intermittent acceleration pulses.

REFERENCES

1. Houbolt, J. C., "Structural Response of Re-Entry Vehicles to Boundary Layer Noise," GE-TIS 65SD223A, March 1965.
2. Houbolt, J. C., "On the Estimation of Pressure Fluctuations in Boundary Layer and Wakes," GE-TIS 66SD296, August 1966.
3. Bull, M. K., Wilby, J. F. and Blackman, D. R., "Wall Pressure Fluctuations in Boundary Layer Flow and Response of Simple Structures to Random Pressure Fields," AASV Report No. 243, July 1963.
4. "Equations, Tables and Charts for Compressible Flow," AMES Research Staff, N. A. C. A. Report No. 1135, 1953.
5. Cassanto, J. M., and Storer, E. M., "A Method of Predicting Base Pressure of Axisymmetric Ballistic Re-Entry Vehicles of Zero Angle of Attack in Turbulent Flow," Aerodynamics Technology Component Fundamentals Memo 64-6, December 1964, DIN ATFM 64-6, Classified Report.
6. Bozich, D. J., "Spatial Correlation in Acoustic Structural Coupling," Journal of Acoustical Society of America, Vol. 36, No. 1, January 1964.
7. Bozich, D. J. and White, R. W., "A Study of the Vibration Response of Plates and Shells in Fluctuating Pressure Environments," NASA CR 1515, March 1970.
8. Clarkson, B. L., "Stresses in Skin Panels Subjected to Random Acoustic Loading," Technical Report AFML-TR-67-199, June 1967.
9. Cockburn, J. A. and Jolly, A. C., "Structural Acoustic Response, Noise Transmission Losses and Interior Noise Levels of an Aircraft Fuselage Excited by Random Pressure Fields," AFDL-TR-68-2, August 1968.
10. Crocker, M. J., "The Response of Supersonic Transport Fuselage to Boundary Layer and to Reverberant Fields," J. Sound and Vibration, 9 (1) 6-20, 1969.
11. Maestrello, L. and Linden, T. L. J., "Response of an Acoustically Loaded Panel Excited by Supersonically Convected Turbulence," Boeing Scientific Research Lab Doc. D1-82-0971, May 1970.
12. Maestrello, L., "Radiation from and Panel Response to a Supersonic Turbulent Boundary Layer," Boeing Scientific Research Laboratory Document No. D1-82-0719, September 1968.
13. Strawderman, W. A. and Brand, R. S., "Turbulent Flow-Excited Vibration of a Simply Supported Rectangular Flat Plate," Journal of the Acoustical Society of America, Vol. 45, No. 1, January 1969.

14. Szechenyi, E., "The Response of and the Acoustic Radiation from Panels Excited by Turbulent Boundary Layers, " AFFDL-TR-70-94, June 1970.
15. Wilby, J. F., "The Response of Simple Panels to Turbulent Boundary Layer Excitation, " AFFDL-TR-67-70, October 1967.
16. Jacobs, L. D. and Lagerquist, D. R., "A Finite Element Analysis of Simple Panel Response to Turbulent Boundary Layers, " AFFDL-TR-67-81, December 1967.
17. Jacobs, L. D., Lagerquist, D. R. and Gloyna, F. L., "Response of Complex Structures to Turbulent Boundary Layer, " AIAA Paper No. 69-20, AIAA 7th Aerospace Sciences Meeting, 1969.
18. Maestrello, L., Gedge, M. R. and Reddaway, A. R. F., "Response of Structure to the Pseudo-Sound Field of a Jet (Using a Combined Continuous and Finite Element Method), " NASA AD-663662, September 1967.
19. Olson, M. D. and Lindberg, G. M., "Free Vibrations and Random Response of an Integrally Stiffened Panel, " Conf. on Current Developments in Sonic Fatigue, University of Southampton, July 6-9, 1970.
20. Schweiker, J. W. and Davis, R. E., "Response of Complex Shell Structures to Aerodynamic Noise, " NASA-CR-450, April 1966.
21. Percy, et. al., "SABOR III: A Fortran Program for the Linear Elastic Analysis of Thin Shells of Revolution Under Asymmetric or Axisymmetric Loading by Using the Matrix Displacement Method, " MIT ASRL TR 121-6, May 1965.
22. Moulton, P. B., "Consistently Derived Thermal and Mechanical Applied Forces for Sabor Shell Analysis, " General Electric-RESO, TM-SM-8156-215, Rev. A, August 1969.
23. Chaump, L. E., Monfort, A., "Aeroacoustic Loads Associated with High Beta Re-Entry Vehicles, " AFFDL-TR-72-138, September 1972.
24. Robertson, J. E., "Prediction of In-Flight Fluctuating Pressure Environments Including Protuberance Induced Flow, " Wyle Laboratories Research Report, WR 71-10, March 1971.
25. Coe, C. F., "Surface Pressure Fluctuations Associated with Aerodynamic Noise, " NASA SP-207, July 1969.

Unclassified

Security Classification

DOCUMENT CONTROL DATA - R & D		
(Security classification of title, body of abstract and indexing annotation must be entered when the overall report is classified)		
1. ORIGINATING ACTIVITY (Corporate author) General Electric - RESD 32nd and Chestnut Streets Philadelphia, Penna. 19101		2a. REPORT SECURITY CLASSIFICATION Unclassified
		2b. GROUP
3. REPORT TITLE VIBRATION RESPONSE OF BALLISTIC RE-ENTRY VEHICLES VOLUME I		
4. DESCRIPTIVE NOTES (Type of report and inclusive dates) Final - April 1971 to October 1972		
5. AUTHOR(S) (First name, middle initial, last name) Chaump, Louis, E., Lauzon, Joseph H., Minnich, Harry R.		
6. REPORT DATE April 1973	7a. TOTAL NO. OF PAGES 108	7b. NO. OF REFS 25
8a. CONTRACT OR GRANT NO. F33615-71-C-1562	9a. ORIGINATOR'S REPORT NUMBER(S)	
b. PROJECT NO. 1370		
d. Task No. 137005	9b. OTHER REPORT NO(S) (Any other numbers that may be assigned this report) AFEDL-TR-72-140, Vol I	
10. DISTRIBUTION STATEMENT Distribution limited to U.S. Government agencies only; test and evaluation statement applied 28 November 1972. Other requests for this document must be referred to AF Flight Dynamics Laboratory (FY), Wright-Patterson AFB, Ohio 45433.		
11. SUPPLEMENTARY NOTES		12. SPONSORING MILITARY ACTIVITY Air Force Flight Dynamics Laboratory Wright-Patterson AFB, Ohio 45433
13. ABSTRACT A technique is presented for predicting the vibration responses to re-entry aero-acoustic loading of high beta ballistic vehicles (those having a weight-to-drag ratio greater than 1500). Correlation of predicted responses due to ground acoustic loading and measured data is given and, based on these results, guidelines on the use of the prediction technique for acoustic and aero-acoustic loading are outlined. Computer programs for calculating vibration responses due to reverberant and progressive wave acoustic environments and to aero-acoustic excitations are documented and are available through the Air Force Flight Dynamics Laboratory (FY). Techniques for ground simulation of re-entry vibration response are discussed, and typical component design requirements and test specifications are delineated. The new feature of the technique is the use of finite element methods in deriving component test specifications. These more accurate test specifications will be essential in reducing the number of overdesigned components, thereby decreasing the cost of mission completion.		

DD FORM 1473
1 NOV 65

Unclassified

Security Classification

Unclassified

Security Classification

14. KEY WORDS	LINK A		LINK B		LINK C	
	ROLE	WT	ROLE	WT	ROLE	WT
Re-entry Vibration Aero-acoustic Environment Vibration Prediction Re-entry Simulation Re-entry Specifications						

Unclassified

Security Classification